Universidade de São Paulo
Instituto de Astronomia, Geofísica e Ciências Atmosféricas
Departamento de Astronomia

Lucas Augusto Leardini Siconato

The gamma-ray spectrum of Sagittarius A* with the *Fermi* Telescope

São Paulo
2023

Lucas Augusto Leardini Siconato

The gamma-ray spectrum of Sagittarius A* with the *Fermi* Telescope

Dissertation presented to the Astronomy Department of The Institute of Astronomy, Geophysics and Atmospheric Sciences at the University of São Paulo as partial requisite to obtain the MsC in Astronomy title.

Concentration Area: Astronomy
Advisor: Prof. Dr. Rodrigo Nemmen da Silva

São Paulo

2023

Para minha família, em especial: aos meus pais.

Agradecimentos

Em sua maioria, todas as tarefas que exigem muito de nós não podem ser completadas de maneira solitária. Por essa razão, agradeço inicialmente aos meus pais e a minha irmã, por terem me dado todo o suporte de que precisava.

À minha namorada, por ter me dado todo o seu apoio e por vezes ter me ajudado a seguir em frente nessa empreitada. Agradeço pelo seu amor, seu suporte e pela sua companhia.

Ao Dr. Rodrigo Nemmen, que no âmbito acadêmico foi meu orientador e mestre; me ensinando que sempre há algo interessante para ser estudado e compartilhando comigo todo o seu entusiasmo pela ciência.

Aos colegas do Black Hole Group do IAG/USP, pela amizade, pelas discussões e por todo o aprendizado que tive com cada um de vocês.

Ao Dr. Fábio Cafardo, por ter me ajudado com inúmeras discussões e apontamentos para o projeto.

À Pandora, minha gata, por ter sido durante todo o tempo do mestrado minha firme companheira de trabalho e descanso.

E a todos os demais, que por um motivo ou outro não foram nomidados, saibam que meu carinho e apreço por vocês é imenso.

Esta tese/dissertação foi escrita em LaTeX com a classe IAGTESE, para teses e dissertações do IAG.

"*Deus ao mar o perigo e o abismo deu*
Mas nele é que espelhou o céu"

Fernando Pessoa

"*O que é preciso é ser-se natural e calmo*
Na felicidade ou na infelicidade
Sentir como quem olha,
Pensar como quem anda,
E quando se vai morrer, lembrar-se de que o dia morre,
E que o poente é belo e é bela a noite que fica...
Assim é e assim seja"

Fernando Pessoa

"*Porque, onde estiver o vosso tesouro, ali estará também o vosso coração*"

Lucas 12, 34

Resumo

Estudamos Sagitário A* (Sgr A*) em altas energias usando observações do Large Area Telescope a bordo da espaçonave Fermi. Dividimos nosso projeto em duas etapas: construção da distribuição espectral de energia (SED) da fonte pontual de raios gama 4FGL J1745.6-2859 associada a Sgr A* entre 100 MeV e 500 GeV, e sua modelagem para entender a natureza da emissão. Nossa análise incluiu mais de trezentas fontes dentro de uma janela de 15 graus ao redor da fonte, bem como os componentes de emissão isotrópica difusa galáctica e extragaláctica usuais. Realizamos uma análise detalhada das incertezas sistemáticas para criar o SED final.

Para a segunda parte do trabalho, exploramos um modelo leptônico e descobrimos que as observações são consistentes como provenientes de elétrons relativísticos acelerados durante eventos de erupção perto de Sagitário A*, a uma distância de $\sim 10\mathrm{R_S}$, onde $\mathrm{R_S}$ representa o raio de Schwarzchild. Tais elétrons se afastam do local onde foram acelerados e então interagem com fótons-sementes, originando fótons com energias mais altas. A principal fonte desses fótons são as estrelas do Centro Galáctico. Em particular, assume-se que a taxa de injeção dos elétrons deve situar-se entre 3×10^{-12} cm^{-3} s^{-1} e $1,2 \times 10^{-11}$ cm^{-3} s^{-1}, sua temperatura entre 1 eV e 2 eV e sua densidade de energia entre 6×10^4 eV cm^{-3} e 10^5 eV cm^{-3}.

Abstract

We studied Sagittarius A* (Sgr A*) at high energies using observations from the Large Area Telescope aboard the Fermi spacecraft. We divided our project into two stages: constructing the spectral energy distribution (SED) of the gamma-ray point source 4FGL J1745.6-2859 associated with Sgr A* between 100 MeV and 500 GeV, and its modeling to understand the nature of the emission. Our analysis included over three hundred sources within a 15 degrees window around the source, as well as the usual diffuse galactic and extragalactic isotropic emission components. We performed a detailed analysis of the systematic uncertainties to create the final SED.

For the second part of the work, we explored a leptonic model and find that observations are consistent with coming from relativistic electrons accelerated during flare events close to Sagittarius A*, at a distance of $\sim 10\mathrm{R_S}$, where $\mathrm{R_S}$ represents the Schwarzchild radius. Such electrons move away from the place where they were accelerated and then interact with seed photons originating photons with higher energies. The main source of these photons are the stars in the Galactic Center. In particular, it is assumed that the injection rate of the electrons must lie between 3×10^{-12} cm^{-3} s^{-1} and 1.2×10^{-11} cm^{-3} s^{-1}, their temperature between 1 eV and 2 eV and their energy density between 6×10^4 eV cm^{-3} and 10^5 eV cm^{-3}.

List of Figures

List of Tables

Contents

Chapter 1

Introduction

When the sky is clear and we look up, there are many bright astronomical objects that we are able to see. The vast majority of these objects are galaxies and stars that are located an extremely long way from our own. Even though these astronomical objects are fascinating in and of themselves, when we observe them, we are somewhat constrained in what we can see of them due to the fact that we can only see the visible light that is emitted by them. The universe, which is already quite magnificent, becomes even more astounding when we consider the entire electromagnetic spectrum. This is because, in this scenario, new astronomical objects and even physical phenomena start to be seen.

A very significant part of this Universe is associated with astrophysical objects and phenomena that occur at high energies, particularly through the emission of photons with energies of 100 keV or more, whick are known as γ-rays. Here, region of intense star formation, supernovas, pulsars and BH come into play, showing the most violent set of effects that can be found in the Universe. Among the aforementioned objects, the goal of this dissertation is to investigate a BH, Sagittarius A* (SgrA*).

1.1 Black hole

Black holes (BH) are defined as regions of spacetime with gravitational fields that are so intense that neither massive particles nor light can escape. The publication of Albert Einstein's General Theory of Relativity in 1915 (Einstein (1915)) led to the prediction of a number of consequences, one of which is now known to be associated with the theoretical origin of the objects in question. However, in addition to knowing today that they are a real astrophysical object, we succeeded to research them well; or rather, we managed to study some types of them fairly well. Their studies can be rather difficult at times because by definition these are objects that cannot be seen.

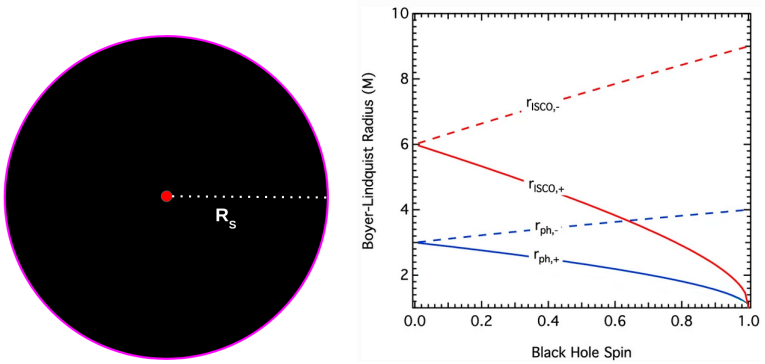

Figure 1.1: Left: Sketch of the structure of a BH. In red, in the center, we have the singularity. In purple, around the BH we have its event horizon. In the given situation, R_s represents the Schwarzschild radius. Both the singularity and the event horizon have been enlarged and highlighted for better visualization. Rigth: Here we have the characteristic radii in the spacetimes of Kerr BH, as a function of the black-hole spin. The plus sign present indicates the case of prograde orbits (those in which the material around the BH rotates in the same direction as its spin) and the minus sign indicates the case of retrograde orbits (those in which the material around the BH BH spins in the opposite direction of its spin). As can be seen, there is a clear dependence of the portrayed quantities on the BH spin. Adaptaded from Psaltis (2019)

The left plot of Figure 1.1 shows the structure of a BH. The singularity and event horizon compose it. The singularity, where spacetime curvature is infinite, is found in BH' centers. According to general relativity, this point in question is where all the mass absorbed by the BH is concentrated. The singularity has no volume, therefore its density must be infinite. In turn, the event horizon needs to be regarded as a membrane rather than a genuine surface. It only permits the movement of matter and light in a single, distinct direction: towards the BH. In this sense, this boundary can and must be seen as what defines the BH. In this particular instance, we are dealing with the fact that we have a BH-like object whenever we are capable of establishing the presence of an event horizon. An important quantity associated with the event horizon is the Schwarzschild radius, defined by the expression:

$$R = \frac{2GM}{c^2} \tag{1.1}$$

This quantity gives us the radius of the event horizon and allows us to calculate it. In addition, BH have other physical properties. The so-called BH photon spheres is another example of it. The photon sphere is a zero-width spherical shell that surrounds the BH, within this region the photons are imprisoned in unstable circular orbits. Since these orbits are unstable, small perturbations can send photons toward the event horizon or away from the BH. As a consequence of things already mentioned, the photon sphere is farther from

the singularity than the event horizon.

Another important property of BH is the innermost stable circular orbit (ISCO). In the same way that light has an orbit relative a BH in which photons circle it in a circular form, matter also do it. The ISCO value of each BH determines the minimum distance from the singularity at which a particle can maintain a stable circular orbit around it, meaning that no matter particle can maintain a stable circular orbit around a BH at a distance less than this limit.

In terms of their physical features BH that spin, have a zone of spacetime that revolves inexorably around them. This BH's frame-dragging effect creates the ergosphere (Thirring (1918, 1921); Lense and Thirring (1918)). In the ergosphere zone, as spacetime is moving, any object cannot stay still. The ergosphere's matter and light particles will not necessarily fall into the BH, depending on initial conditions, they may even travel away from the event horizon. This attribute is even more intriguing, since it is one of the mechanisms that may explain jets in some active galaxies.

An interesting fact is that many of the aforementioned properties, in addition to depending on the mass of BH, they depend on spin. The distance of the photon sphere, or the ISCO from the center of the BH is a function of its spin. This all is shown in the right plot of Figure 1.1.

In terms of classification, BH can be put inside several groups. Schwarzschild black hols have no charge or angular momentum. On the other hand Kerr BH have angular momentum but no charge. Astrophysics' most important BH are Kerr's. Reissner-Nordstrom BH have charge but have no angular momentum at all. Moreover, Kerr-Newman BH are the ones that have all three properties. Each of these BH classification is related to a different metric tensor, a tensor that is used to characterize its spacetime around it, making these distinctions very important. Regarding BH from a mainly practical perspective, they are are usually classified by their matter quantity. Stellar-mass BH are the smallest. They form when certain stars die and have masses of five to ten times the sun (Hughes (2005)). Intermediate-mass BH (IMBH) are the next classification. These BH have masses from 10 to 100 suns. Supermassive BH (SMBHs) with masses greater than 10^5 solar masses are the next categorie and will be discussed below. According to the existing research, a BH can be found at the center of virtually all galaxies (Netzer (2013, 2015)). These astronomical objects make up a highly different class, and because they often have masses that range

from $10^6 - 10^{10} M_\odot$, we refer to them as SMBH.

These objects stand out from the rest due to the fact that they have the potential to have an effect on the galaxies in which they reside. Such influences occur primarily when this type of BH is active through feedback mechanisms (Fabian (2012)), a subject that is beyond the foreseen scope of this work.

However, one of the important parameters to assess the influence of a BH on the surrounding environment is its gravitational sphere of influence. This sphere can be interpreted in a generic sense as a spherical zone surrounding a celestial body in which the major impact on any orbiting object is the gravity from the prominent celestial body in question. In a more personalized way to our case, this sphere of influence is a region in which the galactic gravitational potential is smaller than that generated by the BH, which in turn dominates the entire region. The formula that follows can be used to calculate the radius of such a sphere (Peebles (1972); Thorne et al. (2000)):

$$r_{sp} = \frac{GM_{BH}}{\sigma^2} \tag{1.2}$$

where G represents the gravitational constant, M represents the mass of the BH, and sigma represents the velocity dispersion of the stars in the bulge of the host galaxy. The preceding expression can be modified such that it looks as(Merritt (2004)):

$$r_{sp} \approx 10.8\text{pc} \left(\frac{M_\bullet}{10^8 M_\odot} \right) \left(\frac{\sigma}{200 \text{ km s}^{-1}} \right)^{-2} \tag{1.3}$$

1.2 The Galactic Center

As is widely known that the vast majority of galaxies, if not all, contain a supermassive BH at their galactic core (Lynden-Bell (1969); Kormendy and Ho (2013); Heckman and Best (2014)), the physical processes that take place in this region are typically controlled by objects of this type.

Along with everything else in the Solar System, the Earth is a part of a galaxy known as the Milky Way. Because of this we have a good access our galaxy nuclear region. Therefore, the galactic center (GC) of the Milky Way is, in fact, a true laboratory for the exploration of all of the physics that are associated with BH, as well as the investigation of all of the physics that is involved in the possible interactions of the SMBH with the environment around it.Furthermore, understanding the processes that take place in our galactic center

can shed light on similar processes that take place in other galaxies, which is an essential aspect of this discussion.

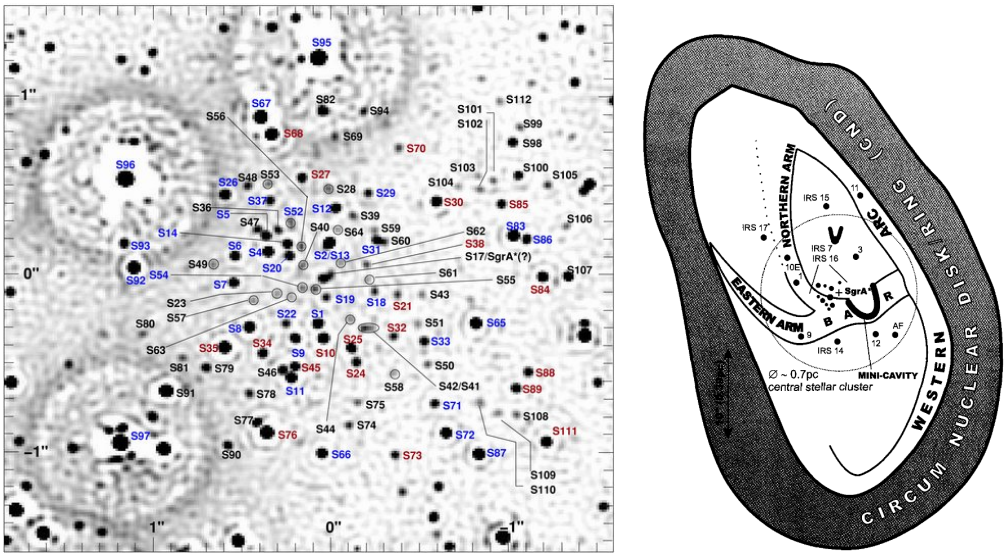

Figure 1.2: Left: This map shows the position of S-star cluster's stars. Stars that are clearly identifiable in numerous photos have designated names. Red markings denote late-type stars, whereas blue labels early-type stars. A black label denotes a star with unkown spectral type. Some light is visible in the location of Sgr A*, which may be caused by itself or by another weak, unidentified star that is mistaken for it. From Gillessen et al. (2009). Right: Schematic representation of the galactic center and its different structures. The position of Sgr A* is indicated by a cross. From Eckart et al. (2005)

Considering the fact that the predominant objective of this dissertation is to investigate gamma emission coming from Sagittarius A*, it is essential to have a knowledge of the GC. Given that this is a very intricate and involved topic, the reader is directed to the following works in the event that additional information is required: Brown and Liszt (1984) and Genzel et al. (2010). Below we will provide a general overview of this region of the galaxy.

If we proceed in the direction of the GC, we will discover something that is known as a circumnuclear disk (CND). The CND is a structure that is located at a distance of around 4 pc from the GC and can be seen inwards as far as 1.5 pc away from it. One can say that it is composed of three essential parts (Güsten et al. (1987); Jackson et al. (1993); Christopher et al. (2005); Montero-Castaño et al. (2009); Tsuboi et al. (2018); Armillotta et al. (2019)). The first of these is a collection of dense molecular clouds that revolves around the most central part of the GC. The second is fundamentally warm dust. The third, corresponds to a dense star cluster, which can then be found in the most central regions of our galaxy. According to the scientific literature, the CND must have a mass of the order of $10^4 M_\odot$ in terms of its gas and dust content (Eckart et al. (2005)). In addition,

it is fed probably by gases that originate from locations further away from the GC, with their origin being more than ten times further out from its inner boundary (Eckart et al. (2005); Hsieh et al. (2017)).

One of the most notable characteristics of the stellar cluster that resides in the GC is the fact that its density rises as we get closer to the central point (Genzel et al. (1994); Alexander (2005); Do et al. (2013); Calderón et al. (2019)). This cluster is also one of the locations in the galaxy that contains the highest concentration of newly formed stars that are extremely massive (Paumard et al. (2003); Alexander (2005); Paumard et al. (2006)). Because the presence of these young stars in such a harsh environment and at such close proximity to the SMBH is not something that is typically expected, this aspect of it is quite fascinating and gives rise to the so-called paradox of youth (Ghez et al. (2003)). This is a fact that throws a wrench into our existing knowledge of star formation and the processes that occur close to SMBH. Figure 1.2 left illustrate the scenario of the galactic center in terms of stellar objects.

Moving closer to the GC, we find that there is a sudden change between the CND and something that is known as the central cavity at the point where the distance is around 1.5 pc. This cavity is notable for both its low density and the strong ionization levels that it possesses (Zylka et al. (1994); Genzel et al. (2010)). Sagittarius A West, an area that gives the impression of a mini spiral with three arms as viewed from Earth, may be found inside of it (Vollmer and Duschl (2000); Christopher et al. (2005); Oka et al. (2011)). It is primarily made up of H II in its composition, but some highly hot gas is also seen in X-ray observations of this place. Sgr A$*$ is found within this cavity, in the central position of the GC Genzel et al. (2010); Akiyama et al. (2022). In Figure 1.2 right, we can see how the central portion of the galaxy is organized, as well as how the arrangement of the galaxy's core parts is laid out. Sagittarius A* can be seen as being housed in a complex, which is also formed by Sagittarius A West, the minispiral, and Sagittarius A East, which is (possibly) a supernova remnant.

The gravitational sphere of influence of Sagittarius A* (eq. 1.2) is delimited by a radius that is somewhere between $2 - 3$ pc (Genzel et al. (2010); Eckart et al. (2017)). It is important to keep in mind since its meaning is that the SMBH is the celestial body that predominates the cavity and a significant portion of the CND's gravity, both aforementioned structures. As might be expected, Sgr A$*$ dominates the mass distribution

of this region. Other contributions include, in order of relevance, those coming from the distribution of dark matter, gas, neutron stars, and stellar-mass BH (Freitag et al. (2006); Ghez et al. (2008); Vasiliev and Zelnikov (2008); Gillessen et al. (2009,?); Murchikova et al. (2019)). Furthermore, in this region there remain certain gaseous masses and stars that are themselves relevant, given that from the orbits of some stars we can, for example, determine the value of the mass of the BH (Ghez et al. (2008); Genzel et al. (2010)).

1.2.1 The Galactic Center in Gamma-rays

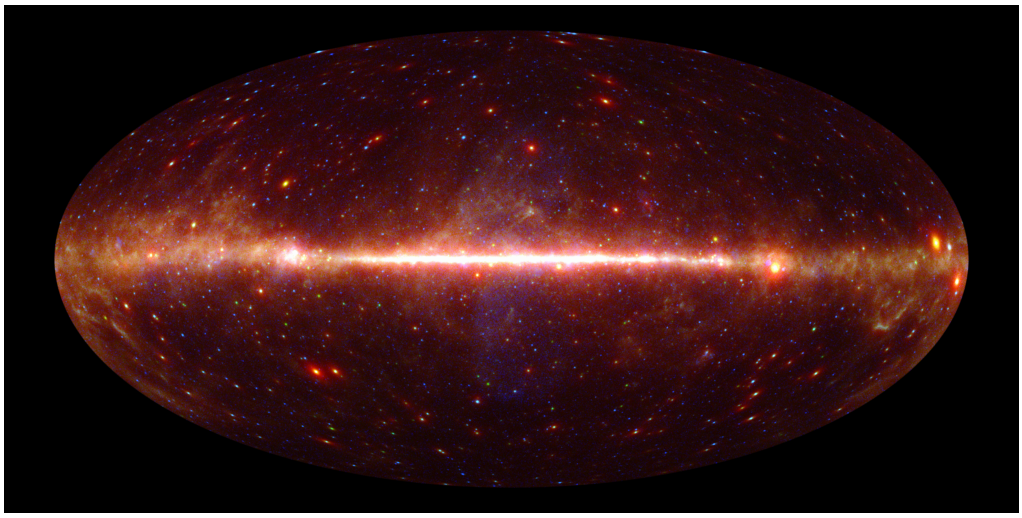

Figure 1.3: A gamma-ray sky map produced using *Fermi* Space telescope observations from August 2008 to May 2021. The energy is split using the photon energy as a criterion. The first energy range is 100MeV to 1GeV and is represented as red. The second one is 1GeV to 10GeV and is represented as green. The last one is 10GeV to 1TeV and is represented as blue. *Carlos, D.; Siconato, L; de Menezes, R.;Nemmen, R.*

When we take a look at the gamma ray sky, it is not difficult to see that the galactic center is the brightest location. Taking a look at Figure 1.3 will prove this point beyond a reasonable doubt in this matter. This figure shows a whole sky map in gamma rays produced with observations from the *Fermi*-LAT Space Telescope between August 2008 and May 2021 using photons with an energy band that ranges from 100MeV to 1TeV.

This image has several interesting features. The first of them is represented in the situation where different colors indicate emissions in different energy bands. The picture displays a red color for emissions with energies between 100 MeV and 1 GeV. If the emissions have a total energy between 1 GeV and 10 GeV, we see the color green and on the other hand, if the emissions have a total energy of between 10 GeV and 1 TeV, we see the

color blue. The second component that is important to emphasize pertains to the most noticeable aspect of the entire map, which is the band of diffuse glow that divides the map in half horizontally. Given that the information shown in this figure is presented in galactic coordinates, this band of diffuse glow represents the plane of our Galaxy. It can be traced back to the interaction of cosmic rays (CR) with the interstellar gas in this region. It is essential to realize that the GC is located at the center of this region characterized by significant gamma emissions. The presence of two structures in the shape of bubbles with strong energy emissions, leaving vertically from the center point of the image, is the third and last aspect brought to your attention here. These structures are known as *Fermi* bubbles and their origin is not fully comprehended at this time (Su et al. (2010); Cheng et al. (2011); Ackermann et al. (2014); Yang et al. (2018)).

The number of sources recognized by the most recent source catalog of *Fermi*-LAT (Abdollahi et al. (2020, 2022)) if we consider a circle of 1 degree around the GC is 6 sources, but, if we take a similar circle, this time one that has 3 degrees around the GC, the number of sources that is accounted for rises up to 50. This location is the most densely populated in all of the sky in terms of the presence of gamma rays. In addition, even when we take into account the emissions from the point sources mentioned earlier as well as those from other locations around the GC, and also if we go further and take into consideration the contribution of gamma emissions that arise from the interaction of the CR with the interstellar medium, there is still an excess of gamma emission in the GC that is not explained by any of the existing models (Goodenough and Hooper (2009); Hooper and Goodenough (2011); Hooper and Linden (2011); Ajello et al. (2016); Ackermann et al. (2017)). There have been many different hypotheses put up in the research community in an attempt to explain this phenomena; however, none of these explanations have been able to adequately provide an explanation yet.

The observation of the GC in gamma rays at energy greater than those captured by *Fermi*-LAT rises yet some others significant characteristic of this place. When observations have an energy greater than 1 TeV, we are able to see in the GC an extended emission zone that is centered on the location of Sgr A* (hes (2016)). This extended region was explained as the result of the interaction between protons with energy on the order of PeV and the gaseous material that made up the first 10 parsecs of the galaxy (Guo et al. (2017); Hooper et al. (2018); Abdalla et al. (2018)).

1.3 Sagittarius A*

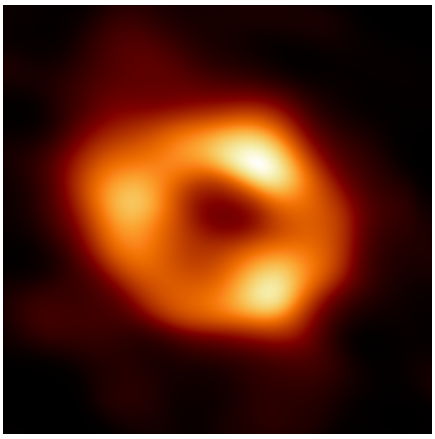

Figure 1.4: The first image by the EHT Collaboration of the shadow of Sgr A*, the Milky Way's SMBH (Akiyama et al. (2022)).

There are a variety of ways in which central SMBH in galaxies might make their presence known to observers. This makes them interesting for us since it allows us to employ a diversity of methodologies and instruments in our investigation of them. Sgr A*, the SMBH of Milk Way galaxy, is in a context of astronomical distances, practically in our garden. It is the second BH whose existence has been established through an image, as shown in Figure 1.4 (Akiyama et al. (2022)). Because of its proximity to Earth, not only can it be used to research the physics of BH, but also to gain a better understanding of how a BH interacts with the stars and the environment that surrounds it.

1.3.1 Sgr A∗ and its historical context

In 1933, Karl Jansky was the first person to detect signals in the radio band that could be attributed to what is now known as Sagittarius A∗ (Jansky (1933)). However, the first direct observations of the source that was later associated with Sgr A* were made in 1974 through the use of radio astronomy (Brown (1973)). Nonetheless, 1974 is the year that is considered the one in which the SMBH from the center of the Milky Way galaxy was discovered. Its name is primarily derived from historical facts and is connected to its location in the sky, as it lies on the boundary between the constellations of Sagittarius and Scorpio. Additionally, due to the fact that it was an exciting discovery, a parallel was made to the nomenclature used in excited atoms, which resulted in it receiving an asterisk

in its name. The letter A, in turn, was used to denote the brightest radio source within the constellation (Goss et al. (2003)).

The idea that there was a mass concentration at the GC first emerged from measurements of the velocity of ionized gas in the line of sight taken at the end of 1970 showing values of a few hundred km/s (Wollman et al. (1977); Lacy et al. (1980)). Virial analysis was used to confirm and support that this mass concentration was a BH with a mass of $2-4\times10^{6}\mathrm{M}_{\odot}$, what caused it to be connected to the compact radio emission source found earlier (Lacy et al. (1982)). Since gas in these kind of regions have a volatile behavior as it is not only subjected to the force of gravity, measurements from stellar dynamics had to be made to further investigate the claims.

1.3.2 Sgr A at the GC: a certainty*

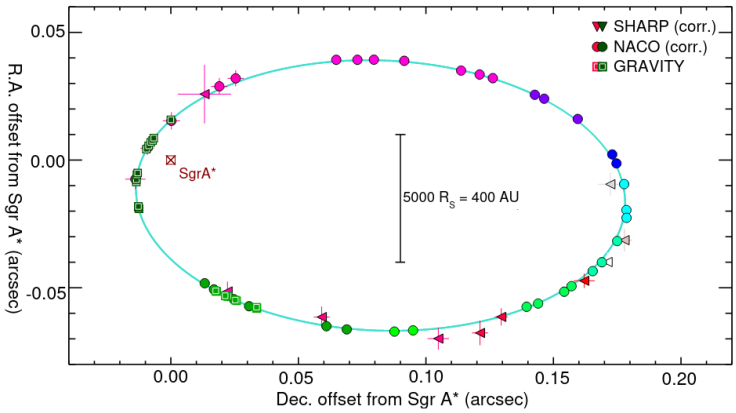

Figure 1.5: S2 star projected orbit, with relation to the location of Sgr A∗ in the sky. (J2000). Adapted from Abuter et al. (2018)

In order to comprehend the behavior of this region and its physical composition, we must analyze the star orbits in the GC. They can be used to test the effects of general relativity around a SMBH (Abuter et al. (2018, 2020)), provide information about the mass distribution in the GC (Rubilar and Eckart (2001); Mouawad et al. (2005)), and provide pertinent data about Sgr A∗ itselft, such as its mass and distance (Eisenhauer et al. (2005); Genzel and Karas (2006); Boehle et al. (2016); Abuter et al. (2019)). Near-infrared (NIR) observations and adaptive optics were both used for this kind of studies. Several stars in the so-called S-star cluster have already had their entire orbits observed as of today (Gillessen et al. (2009)), primarily due to the work of the Gravity collaboration (Abuter

et al. (2019)). This particular stellar cluster is shown in Figure 1.2 left, along with the names of several of its members.

The so-called S2 star stands out in this group of stars because it is one of the brightest and because its orbit around Sgr A* only lasts about 16 years, which is much shorter than most (Abuter et al. (2018)). Its orbit, in addition to the last said propertie, must be explainet by general relativity. At its pericenter, this star is moving at a speed of about 7650 km/s (Gillessen et al. (2009); Abuter et al. (2018)). Figure 1.5, presents the orbit of this star from data collected over 26 years. Like S2, the star S4714 is very close to Sgr A*. It has even a shorter orbital period, with a duration of only 12 years and an orbital speed that can reach 8% the speed of light (Peißker et al. (2020)). From these observation is possible to make inferences about Sgr A* see that this compact region of high mass is indeed an SMBH.

Other observations, in turn, showed that dense gas clouds with masses on the order of 18×10^{24} kg are moving toward the area where the mass of Sgr A* dominates the gravitational potential. G2 is the name of this gaseous mass. There was, within the scientific community, great hope that between the end of 2013 and the beginning of 2014 (Gillessen et al. (2013)) this mass would suffer a tidal disruption event in the GC, culminating in burst events, outflows and increasing the rate of accretion of Sgr A* (Saitoh et al. (2014); Schartmann et al. (2012)). Several observational campaigns were set up, but despite the fact that it is known that the G2 object left Sgr A*'s sphere of gravitational influence more elongated than it entered, the predictions did not come true (Plewa et al. (2017)).

The detection of orbital movements of hot pots is another evidence of how the GC works. In them, located in a region very close to the ISCO of the SMBH, very high velocities are found, reaching values of the order of 30% of the speed of light (Abuter et al. (2018)). That, in turn, is more evidence as to what it is that we find at the GC, a SMBH.

Realize, however, that the above things are all indirect evidence of the existence of an SMBH in the GC. This is because they are the result of what its presence can do there. For a long time, these were the facts that enabled us to say that Sgr A* was real. Today, however, we have direct evidence of its existence, the result of the work of the EHT Collaboration which, using Very Long Baseline Interferometry (VLBI) techniques, was able to generate an image of the shadow of Sagittarius A* (Akiyama et al. (2022)). This image has already been shown in Figure 1.4, above.

Sagittarius A* basic facts

	Fact	Value	Source
1	Mass	$(4.02 \pm 0.20) \times 10^6 M_\odot$	Boehle et al. (2016)
2	Distance	8.2kpc	Abuter et al. (2019)
3	Schwarzschild radius	$R_S \approx 1.2 \times 10^7$ km	From 1, above
4	ISCO (non-rotating BH)	$3R_S \approx 3.6 \times 10^7$km	From 3, above
5	Bondi radius	$R_B \approx 10^5 R_S$	From 3 and Genzel et al. (2010)
6	Sphere of influence	$R_{sh} \approx 2 - 3$ pc	Genzel et al. (2010)
7	Luminosity (radio to X-ray)	$L_{bol} \approx 10^{36}$ erg s^{-1}	Genzel et al. (2010)
8	Eddington luminosity	$L_{Edd} \approx 5 \times 10^{44}$erg s^{-1}	Genzel et al. (2010)
9	Accretion rate	$10^{-9} \leq \dot{M} \leq 10^{-7}$ $M_\odot$/yr	Genzel et al. (2010)
10	Eddington mass accretion rate	$\dot{M}_{Edd} \approx 9 \times 10^{-2} M_\odot$	From 8, above

Table 1.1 - Set of basic and relevant facts about Sgr A*, the black hole at the center of the Milky Way

Starting from the fact of the reality of the existence of Sgr A*, table 1.1 lists ten fundamental and pertinent facts of this SMBH. Five of them are either already covered in the text above or have widely accepted definitions. Below is a brief discussion of the new five. In a spherical accretion environment, the bondi radius is defined from the point that we set the escape velocity of the environment equal to the sound speed. From this we can get a radius that is the bondi radius. It represents the boundary between subsonic and supersonic infall in this environment (Edgar (2004)). In turn, the luminosity shown in the table, assumes an isotropic emission mechanism and represents the total luminosity , from the radio to the X-ray emissions of the SMBH of interest. Differently, the luminosity that an object has when the force produced by the radiation pressure equals the gravitational force is known as Eddington's luminosity. As in other situations, it considers the accretion to be spherical. The accretion rate, in turn, represents the amount of matter per unit of time that is falling in the SMBH. The Eddington accretion rate, in turn, derives from the Eddington luminosity, since $\dot{M}_{Edd} = L_{Edd}/c\eta$, where η represents the accretion efficiency and is usually taken as a value of $\eta = 0.1$.

1.3.3 Sgr A* and its two states

In-depth analysis reveals that this SMBH typically exists in a steady state with $L \sim 10^{36}$ erg/s falling between radio and X-ray frequencies (Genzel et al. (2010)). The lowest energy part of the electromagnetic spectrum, between radio and submm, dominates the majority of it. However, Sgr A* can be seen as an underluminous BH, which is surprising because there enough gas in the GC region that would enable it to be much brighter than it is right now (Genzel et al. (2010)). Its luminosity is roughly 8 times lower than its Eddington

luminosity in comparison, as shown by the data in table 1.1.

In terms of physical origins, the luminosity of Sgr A* is mainly due to accretion from stellar winds that occur in its vicinity (Eckart et al. (2005); Genzel et al. (2010)). Furthermore, because this process is not time-independent, it is possible to occasionally observe higher accretion rates than usual as a result of stochastic fluctuations in the accretion disk or as a result of gas clouds with low angular momentum that end up falling to the galaxy's center.

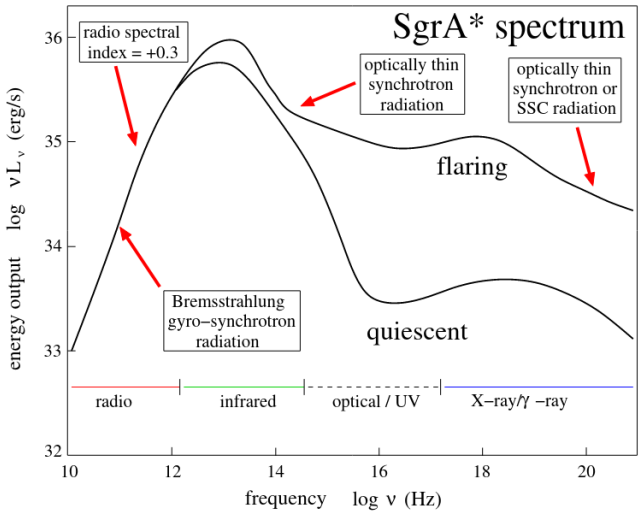

Figure 1.6: Sagittarius A* spectrum showing differences between quiescent and flaring states. From Eckart et al. (2018)

Sgr A* has essentially two different emission states: a quiescent state and a flaring state. An illustration of their behavior can be seen in Figure 1.6. Its emissions in the NIR and X-ray regions stand out for their variability. An analysis of nearly two decades' worth of NIR data reveals that it exhibit consistent variability over the entire time period (Chen et al. (2019)), possibly related to synchrotron emissions from a population of non-thermal electrons (Witzel et al. (2018)). In turn, the X-ray emissions must come shocks, thermalization, and bremsstrahlung processes (Baganoff et al. (2003); Xu et al. (2006)).

1.3.3.1 Its variability

Physically speaking, Sgr A*'s extremely high variability in the infrared and X-ray band region is very significant because it supports the idea that the source is indeed compact by imposing an upper size limit that can be determined by calculating the light crossing time (Baganoff et al. (2001); Genzel et al. (2003); Ghez et al. (2004); Dodds-Eden et al.

(2009); Neilsen et al. (2013); Fazio et al. (2018); Boyce et al. (2019); Murchikova and Witzel (2021); Witzel et al. (2021); Boyce et al. (2022)). Flares in the NIR and X-ray range happen frequently. The latter, for example, happen almost daily and last from a few to tens of minutes (Neilsen et al. (2013)). NIRs flares, in turn, can occur at an even higher frequency than daily. While not all NIR flares are followed by an X-ray flare (Yusef-Zadeh et al. (2012); Ponti et al. (2017)), it is important to note that this is not unusual because after several of them, it was already observed the emission in this other band as well (Fazio et al. (2018)).

Now, the occurrence of flares is a definite sign that a distinctive event occurred in the galaxy's central environment. For instance, it might be a magnetic reconnection mechanism, heating, or some accretion (Netzer (2013); Ball et al. (2016)). This kind of behavior even helps to provide us with hints about what is going on there. Furthermore, in areas near Sgr A*, relativistic effects like gravitational redshift and doppler boosting may be present (Eckart et al. (2006); von Fellenberg et al. (2023)), which are evident in some X-ray flares, since it affect how the flare overall shape appears (Nowak et al. (2012); Ponti et al. (2017)).

It is important to realize that, while gamma emissions appear to be non-variable (Chernyakova et al. (2010); Malyshev et al. (2015)), emissions at wavelengths longer than NIR have been observed (Zhao et al. (2003); Miyazaki et al. (2004); Marrone et al. (2008); Yusef-Zadeh et al. (2009); Brinkerink et al. (2015); Stone et al. (2016); Boyce et al. (2019)). Particularly, we know that this type of variable radio band emission has typical durations ranging from a few hours to days (Zhao et al. (2003); Herrnstein et al. (2004); Mauerhan et al. (2005); Marrone et al. (2006) and are quite important for understanding the galaxy's core environment.

Note, therefore, that although Sgr A* is an SMBH that is currently not in an active state, these types of events are valid to provide us with information about its functioning. Although it is not the scope of this work, any of the above topics could certainly be explored in a particular way to get insights about this particular source.

1.3.3.2 Sgr A* from the gamma ray perspective

Numerous telescopes and high-energy observation campaigns have already picked up and reported gamma ray emissions from a position consistent with Sgr A*. However, it

is not simple to say with certainty that these emissions originate from Sgr A*. Cafardo et al. (2021) explores this in his work and studies different possibilities of origin for the emissions detected by *Fermi*-LAT energy range, reaching the conclusion that, in the band detected by *Fermi*, the highest probability is that these detected emissions are associated to a gamma ray counterpart of Sagittarius A* since the other possibilities explored cannot satisfactorily explain the observations.

From the historical perspective, the GC source 3EG J1746-2851 was identified with 95% confidence by EGRET, another gamma-ray space telescope (Hartman et al. (1999)). It was initially thought to be incongruous with Sgr A*'s position, but up until that point, it was the source connected to the GC (Mayer-Hasselwander et al. (1998)). With time and advancements in observing techniques made with this telescope, the aforementioned source was actually connected to Sgr A East, and its gamma emissions were thought to be the result of pion decay (Hooper and Dingus (2005); Fatuzzo and Melia (2003)). VERITAS, H.E.S.S., and MAGIC, three terrestrial gamma-ray observatories, made detections of gamma emission from the GC. In relation to the first one, this detection occurred in the TeV band and achieved 95% confidence level about the emission region, which measured about 0°15, included the position of Sgr A*, and was consistent with a point source (Kosack et al. (2004)). When we looked at a region of 1' in the second case, there was also the detection of photons with extremely high energies that coincided with Sgr A*, made by the H.E.S.S. (Aharonian et al. (2004)). More contemporary evidence points to the existence of a petravon in the central region of the galaxy, and it is possible that a period of greater Sgr A* activity is responsible for it (Abdalla et al. (2018)). In the case of MAGIC, GC's observations also identified a point source emitting gamma rays there (Albert et al. (2006)), whose location is coincident with both Sgr A* and Sgr A East (Ahnen et al. (2017)). Moreover, their results are compatible with those found by H.E.S.S. (Acciari et al. (2020)).

From the point of view of *Fermi*-LAT, a point source coincident with the position of Sgr A* is detected when considering emissions from MeV to TeV. This is not a modern peculiarity, as since the beginning of the telescope's operations, this source has already been detected. This source has been extensively studied in the literature by different authors, two of the main works being those by Chernyakova et al. (2010) and Malyshev et al. (2015). The first analyzed this source when only 25 months of data were available,

while the other analyzed it when 74 months of data were available.

The detection of two massive bubbles, which have a width of roughly 40° in longitudinal distance and extend for about 50° above and below the galactic plane, was a very important point and a consequence of the observations made with the *Fermi*-LAT (Su et al. (2010)). These bubbles are known today as the Fermi bubbles, and can be recognized in Figure 1.3 as the blue structures that come out of the central region of the galaxy. Currently, efforts are being made to identify and fully comprehend these structures' origin. Some scenarios suggest that it may be due to a starburst episode that happened in the galactic core region, while others relate it to past SMBH accretions (Yang et al. (2018); Mertsch and Petrosian (2019); Negro et al. (2022)). In a sentence: this structure could therefore be a hint of past Sgr A* activity, which make it of great interest.

1.3.4 Emissions from Sgr A: modeling*

In the context of emission models, Sgr A* has been explained a lot better through the use of RIAF models (Narayan et al. (1995); Yuan et al. (2003)) than with any other. According to this scenario, the main emissions of the spectrum, those that take place between radio and submm, are caused by a population of thermal electrons and a much smaller population of non-thermal electrons, through the synchrotron mechanism (Yuan et al. (2003)). NIR emissions, in turn, are directly associated with the SMBH accretion flow and changes that may occur in it (Ghez et al. (2004); Dodds-Eden et al. (2009)).

The emissions from this SMBH are split into two parts at higher energies, specifically at the X-rays band: one part is in charge of producing the flares that we see, and the other is in charge of creating the quiescent spectrum. In terms of the first, the models are consistent with the idea that they are created very close to Sgr A*, possibly as a result of inverse Compton scattering caused by the non-thermal electrons that are present there (Ball et al. (2016)). Others contend that these events can be produced by synchrotron emissions themselves (Dodds-Eden et al. (2009)), so there is not a conclusive model regarding it yet. It is thought that the component that produces the quiescent emissions is the result of an extended region with a size similar to the Bondi radius, and that the emissions happen via the bremsstrahlung process, originated due to shocks that occur in the region as a result of the region's transition between the accretion flow and its general environment (Quataert et al. (2002)).

1.4 High-energy astrophysics

Gamma rays, which are abundant in our universe and shine brilliantly, offer us fascinating opportunities to study them. We can therefore look into issues like their emergence environment and the kinds of particles that gave rise to them. As we are unable to directly observe high-energy radiation, telescopes act as a substitute for our eyes. Despite the fact that there are numerous gamma telescopes, we will only use the data from the *Fermi* space telescope for this investigation.

The definition of a gamma ray is any photon with energy equal to or greater than 100 keV and they are excellent probes for high-energy events in the universe that originate from non-thermal processes. Gamma rays are also intriguing because they are related to other cosmic messengers being studied by modern astronomy. Moreover, gamma rays can indirectly study dark matter and fundamental physics. It is important to note that our atmosphere absorbs the majority of the gamma rays that make it to our planet and launching telescopes into space may be necessary to observe them.

Gamma rays can be seen coming from a number of different places when viewed from an extragalactic perspective. Among these, we have blazars, gamma-ray bursts, (GRBs) and emissions by galaxies that are undergoing a so-called starburst - a rapid rate of star formation. In the galactic context, pulsars, supernova remnants, and microquasars are examples of sources that are capable of emitting this type of radiation. There is also a diffuse and galactic contribution which will be covered in greater detail later on.

Gamma rays and CR have a very close connection with one another. This occurs as a result of the fact that CR, which are charged and accelerated particles, might sometimes result in the emission of gamma rays because of its interaction with the environment. Therefore, having some additional knowledge about one implies having some further knowledge, about the other. The gamma emissions created by leptonic particles and the emissions generated by hadronic particles are the two primary scenarios that are typically investigated when looking into circumstances such as these. They will be explored as necessary below.

1.5 The *Fermi* Space Telescope

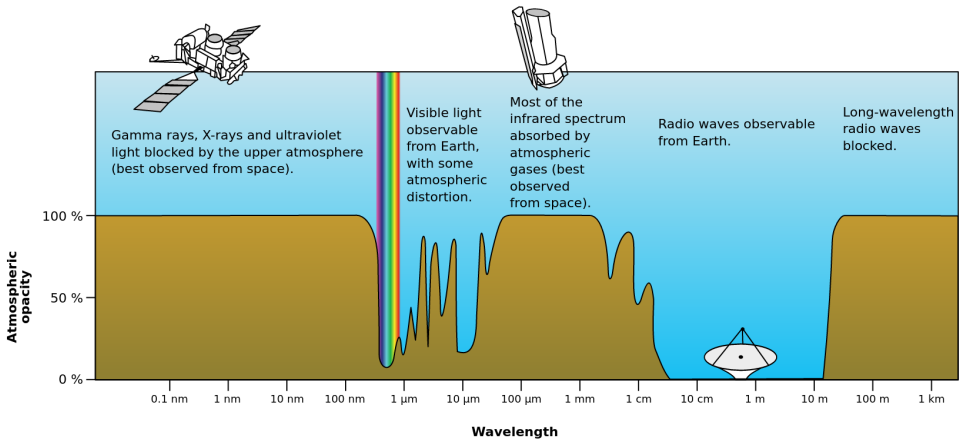

Figure 1.7: Atmospheric opacity as a function of different wavelengths. From: NASA (original); vectorized by Mysid / Public domain

Several gamma ray telescopes exist, some of which are space-based and some are terrestrial. As the interaction properties of these kind of photons with matter are more unusual than those of with lower energies we cannot use lenses to focus these photons in telescopes. Therefore, we are led to use telescopes that use particle accelerator technologies, or else, telescopes that are sensitive to Cherenkov radiation.

The fact that the atmosphere of the Earth is opaque to various wavelengths of light, including gamma light, as demonstrated in Figure 1.7, is another significant aspect of this topic. In this scenario, even if we consider the cost, the limit on its size and consequently on its effective area, one of the most interesting alternatives is to carry out the observation utilizing telescopes that are in space, in orbits around the planet.

1.5.1 A general overview of the *Fermi* Space Telescope

On June 11, 2008, NASA successfully launched the *Fermi* Space Telescope into space (Atwood et al. (2009)). It is a gamma-ray observatory that orbits our globe in an orbit of $\approx$ 535 km above sea level.

Because there are basically three types of interactions that high-energy photons can have with matter: i) Compton scattering; ii) formation of electron-positron pairs (e^- e^+) and iv) the photoelectric effect, gamma telescopes are not traditional since they cannot employ reflection and refraction to focus that light. These telescopes make use of the

principles and procedures of particle accelerators, detecting the light in an indirect manner, through the detection of the products that result from one of the interactions indicated above.

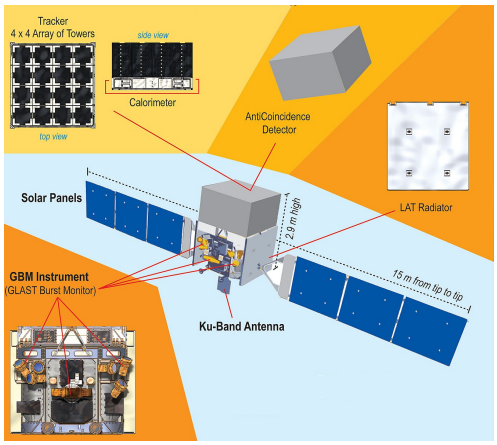

Figure 1.8: An overview of the *Fermi* Space Telescope and its main components. Adapted from NASA (GLAST)

As for the telescope's observation modes, although they may be requested by members of the collaboration, usually *Fermi* operates looking at the whole sky and not at a particular source. It maintains its orientation toward the northern celestial hemisphere during some of its orbits and maintains its orientation toward the southern celestial hemisphere during other orbits. This causes the observation hemisphere to oscillate throughout each of its orbits. The entire sky is surveyed approximately once every three hours, which corresponds to the amount of time it takes for two of its orbits to be completed. Because of this, it is possible to conduct time domain gamma ray astronomy studies using it. On the other hand, this continual exposure to the sky at high energies results in the obtaining of deeper and more focused images, which means that the limit in this case happens only because of how faint a given source is, or else the resolution of the instrument.

Fermi's expected lifespan was originally estimated to be between 5 and 10 years, but is now extended, making the total amount of time it has been operational slightly over 14 years, with no clear indication of when it will stop working. There are two instruments dedicated to different purposes in it: The Large Area Telescope (LAT) and the Gamma-ray Burst Monitor (GBM). Both can be seen in Figure 1.8 along with details of the telescope's other apparatus and devices.

Particularly, the purpose of the GBM is to investigate gamma ray flares that occur all

of a suddenIt is able to detect photons whose initial energy is 10 keV, which are actually X-ray photons, and it can capture photons whose maximal energy is larger than 25 MeV. This energy range is the result of the decision to have the instrument capture photons with energies that are both lower than the limit associated with GRB and simultaneously with energies that are higher than the minimum seen by the LAT. The sensitivity of measurements of the sky in gamma rays carried out by the *Fermi* mission is approximately thirty times higher than the results acquired by earlier missions (Kanbach et al. (1989); Atwood et al. (2009)). This is due, in part, to the the field of view (FOV) of both of the *Fermi* instruments. It is important to point out that *Fermi* continuously operates in a configuration that prevents it from detecting gamma rays emanating from the silhouette of the planet. Instead, it is only instructed to collect these photons at specific times that may be helpful for the calibration of the instruments.

1.5.2 The LAT instrument

The main instrument of the *Fermi* space telescope is the Large Area Telescope (LAT), which was designed to observe high energy photons - gamma rays, coming from the universe. In terms of energy, the LAT operates in the range given by 20MeV- $>$ 300GeV. Another important characteristic of this instrument is its wide FoV, of approximately 2.4sr.

In account of the properties of gamma rays and the ways in which they interact with matter, the LAT functions on the basis of the occurrence of the following reaction:

$$\gamma \rightarrow e^{+} + e^{-} \tag{1.4}$$

Thus, the LAT is a pair conversion telescope. This is a very significant feature because, in addition to allowing for the detection of these photons, this process also possesses particular properties that enable us to differentiate gamma ray events from CR ones. This is relevant given that the flux of CR is about one hundred thousand times greater than that of gamma rays, implying that for the proper functioning of this instrument, a good knowledge of the background emissions that it can detect is necessary (De Angelis and Mallamaci (2018)).

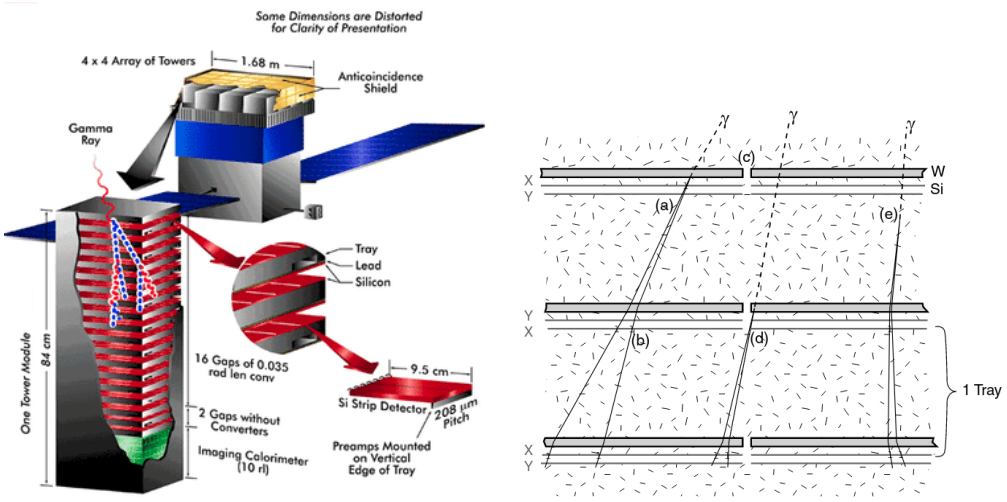

Figure 1.9: Left: Adapted from: Schematic view of the *Fermi* Large Area Telescope and its components. From: Sundbäck (2018). Right: Illustration about the tracker working principle. From: Atwood et al. (2009).

The LAT is composed of three primary components. The first one is a 4x4 array of identical towers, which is where the trackers are located. They are the portion of the telescope in which the gamma rays interact with the material through the pair production process, and the product particles are followed in their path in order to recover the photon information. It can be seen in on both panels of Figure 1.9. The second is a calorimeter made of cesium iodide. It is used to measure the amount of energy possessed by the particles that are produced as a direct result of the reaction that takes place between the photons and the tracker. The Anticoincidence Detector (ACD), which is essentially a scintillator with the goal of rejecting the huge number of CRs that reach the telescope, is the third part of the LAT.

1.5.3 LAT products

Every astrophysical photon that is collected by the telescope has its own unique set of physical characteristics, which are duly recorded. The reconstructed energy and direction of the event, the moment of conversion of these photons into pairs as well as the quality of each of these parameters are included in this set of information. The quality of each of these parameters can vary from event to event depending on how well the LAT is performing. The total number of events that have been recorded by *Fermi*-LAT between the beginning of telescope operation on August 4, 2008 and today, October 3, 2022, is $\sim 4.1 \times 10^9$. Roughly

40% of these events have been categorized as having a high probability that they were caused by photons. This disparity occurs due to the fact that the *Fermi* collaboration's reconstruction of the events is influenced by a variety of parameters. It is important to note that as time passes, more information is gained about the LAT itself, leading to a better understanding of how the telescope operates as well as the environment in which it is located when it is in orbit. This leads to an improvement in the categorization process as a whole. You may locate a comprehensive and extensive explanation of this on-line[1].

Nonetheless, *Fermi* does not collect data continuously, and this is another piece of information that needs to be taken into consideration for the analyses.

In practical terms, other informations are needed to make an analysis, such as a catalog for the identification of gamma ray sources that we have in the sky, a model of diffuse emission from our galaxy and from background extragalactic emission, as well as the Instrument Response Functions, (IRF), a set of functions that is essential for us to bring meaning to the collected data.

Fermi data is divided into event classes. The degree to which the *Fermi*-LAT algorithms are able to accurately reconstruct a particular event is the criterion that determines whether or not that event belongs to a particular class. That is to say: the more likely it is that a particular event was caused by an astrophysical photon, the more constrained the level at which it is, since these categories are organized in a hierarchical fashion: events with lower probabilities than another category are less restricted than the latter category. The class of photons that are of a higher quality has events that have a lower background (BG) contamination and a narrower point spread function (PSF), but these benefits come at the expense of a smaller total number of events. In the others, the chance that photons were responsible for the occurrence of the event diminishes, but the number of events increases.

In addition to the classification of events into classes, which was just covered, the data obtained from *Fermi* are also split up into a variety of additional groups. For instance, events that belong to the same class can be further separated into event types, which make use of selections based on the particular event topology, such as whether or not an event converted in the FRONT or BACK area of the Tracker. Likewise, events can be divided in categories that are an indicator of the quality of the energy reconstruction of the photon that was collected by the detector or in accordance with the quality of the reconstructed

[1] https://fermi.gsfc.nasa.gov/ssc/data/analysis/documentation/Cicerone/

direction. In this work, all available photons were used.

1.6 LAT Sources Catalogs

In order to carry out an investigation of a gamma source, one of the fundamental necessities that must first be satisfied is the creation of a model that explains the gamma ray emissions in the area of the sky that is being investigated. Because of this, it is necessary for us to be aware with the most, if not all, of the gamma ray sources located in the area that we are investigating. As a consequence of this, the *Fermi* Collaboration has, throughout the course of time, able to publish official source catalogs that these can be used to assist in the creation of models that are required for the analyses. Historically, different catalogues were released by the LAT Collaboration.

Here, use the 4FGL-DR3 catalog, which now contain information regarding 12 years of observations of the gamma-ray sky (Abdollahi et al. (2022)) and is the most up to date one.

1.6.1 4FGL-DR3 Catalog

The 4FGL-DR3 catalog has a total of 6658 sources incorporated into it, and the energy range that their emissions cover is between 50 MeV and 1 TeV. For comparison purposes, 4FGL-DR2 recognized the existence of 5787 sources. This new catalog, along with the two that came before it, makes use of various spectral shapes for its modeling. These spectral shapes are determined by the observed properties of the source, with pulsars typically being modeled with a Power Law cutoff and other sources being modeled with a model of the LogParabola in the event that a statistically significant curvature in their emissions is detected, or else by a simple and direct PowerLaw. A source's significance must be more than 4σ in order for it to be considered for inclusion in this catalog. The catalog also has information about the location of these sources in the sky.

The so-called log-parabola or the log-normal representation is one of the spectral models that are utilized in the catalog. Particularly helpful in sources with a curved spectrum, its expression is given by:

$$\frac{dN}{dE} = N_0 \left(\frac{E}{E_0}\right)^{-\alpha-\beta\log(E/E_0)} \tag{1.5}$$

The variables N_0 stands for the normalization that has been defined at a reference energy

E_0, chosen such that the error on the normalization was minimal, α determines the slope of the spectrum at the energy E_0, whereas β identifies the spectrum's curvature. In the case of point sources the above expressions have the units $cm^{-2}\ s^{-1}\ MeV^{-1}$. Our interest in it is associated with the fact that the spectrum of source 4FGL J1745.6-2859 is described by a law of this form.

1.6.2 The 4FGL J1745.6-2859 source

4FGL J1745.6-2859 is, one of the most interesting sources of the galactic center, which includes some of the most diverse sources. Besides, this source is not only the brightest we have in the area, but it is also the source that is located closest to Sagittarius A* position, according to the data that is part of the catalog 4FGL-DR3. We now understand that this source is in fact the gamma-ray counterpart of Sgr A*, which indeed enables us to acquire a high-energy view of this SMBH (Cafardo et al. (2021)).

1.6.3 The diffuse models

In addition to point and extended sources, the 4FGL-DR3 catalog (Abdollahi et al. (2022)) also contains information about two diffuse emission components that need to be considered when working with the gamma ray sky in the *Fermi* energy band. These two models are referred to as the galactic diffuse emission model (galdiff) and as the extragalactic isotropic diffuse emission model (isodiff). The most important aspects of each of them is summarized below. A more comprehensive collection of information may be obtained in the relevant literature (Abdollahi et al. (2020)).

1.6.3.1 The galactic diffuse emission model

Emissions from activities occurring between the stars predominate the gamma ray sky at energies greater than 50 MeV. The presence of CR in the interstellar medium is largely responsible for this phenomenon. The decay of pions into gamma rays, for example, is caused by the interaction of CR protons with other nuclei in the galactic environment. CR electrons, in turn, can also produce gamma rays through the Bremsstrahlung process. The Inverse Compton (IC) scattering of these CR electrons with lower energy photons, such as infrared or ultraviolet photons from the interstellar radiation field (ISRF) can also generate this kind of light.

Of all the photons generated by this process, those of lower energies, particularly the ones with less than a few hundred GeV, do not participate in any further interactions. Because of this, the galaxy's diffuse emission is seen to have a higher brightness at lower gamma energies. This effect is due to a combination of interstellar gas column density and ISRF intensity. Moreover, because of the way interstellar gas is distributed throughout the galaxy, gamma ray emission in this energy band and others gamma rays bands is significantly higher at lower galactic latitudes than it is at higher latitudes.

The model that makes an attempt to explain the radiative transfer of gamma rays that takes place in the Milky Way try to provide an explanation for all the gamma emission that is present in it. This is accomplished by linearly combining a number of distinct templates, each of which represents a different element of the emission being studied. These elements are i) the gas within the galaxy; ii) dark and cold gas iii) IC scattering and ISRF models; iv) the large-scale structures; v) information about already cataloged galactic high energy sources; vi) information on unresolved galactic sources and vii) lunar and solar emissions.

In reference to the first element mentioned earlier, the information required to determine the distribution of the gas that is found in the Milky Way is obtained from the surveys of spectral lines of HI and CO, with the latter serving as an H_2 tracer. In addition, information about tracers that emit in the infrared was used in order to correct any possible overestimates or underestimates that were made regarding the HI column densities. With all that, a model of gamma ray emissions was constructed for the central region of the galaxy.

Dark and cold gas forms the second element used in the construction of templates. This is the component of the interstellar medium that is gaseous but cannot be traced via HI or CO emissions. The existence of this component was demonstrated by analyzing the thermal emission data of HI, CO, and gamma rays (Grenier et al. (2005)). Its analysis is carried out in great depth for the same region of the gases that was covered in the earlier point.

When it came to the IC scattering and the ISRF models, the analysis was carried out once again for the same region as before. In particular, the *Fermi*-LAT collaboration utilized the Porter et al. (2017) and Ackermann et al. (2012) works in order to model the IC emissions. Going further, another component that was taken into consideration was the large-scale structures. In particular, they make reference to other structures in the

interstellar medium that do not have clear counterparts in other wavelengths to be used for template construction. The most important examples of it are the *Fermi* bubbles.

In the process of developing the overall framework for the template, it was necessary to make use of information pertaining to known and existing sources. This is to be expected, since this kind of information is especially helpful because it makes it possible for the emissions from these sources to not be incorrectly attributed to the diffuse emissions model. Preliminary versions of the 4FGL catalog were utilized to provide sources information. Finally, the Sun and the Moon must be taken into account because they act as effective diffuse sources of gamma rays. So a template that could be used for each of them individually was created.

As a result, the galactic diffuse emission model emerges from the linear combination of templates derived from each of the elements covered earlier. This gamma ray component, which has a very large spatial extent, is the brightest one that has ever been found. It is important to point out that models of this kind are modified over the course of time and that, despite being built in this manner, the model still contains a number of uncertainties by its very nature.

1.6.3.2 The isotropic diffuse model

An isotropic background that is quite significant can be seen in the *Fermi*-LAT data. This background is caused, for example, by unresolved extragalactic sources as well as residual cosmic ray emissions. In this context, the extragalactic diffuse emission model was developed in order to provide an explanation for occurrences such as these. This model was developed in the energy band that is bounded by 30 Mev and 1 TeV. In addition, in order to prevent contamination brought on by diffuse emissions from the galaxy as a whole, it do not take into account any emissions that originate from the galactic plane region.

This model is obtained in a practical sense through the residual emission that is found between the data and the sum of galactic diffuse emissions with information on emissions from sources that are listed in the 4FGL catalog as well as contributions related to solar and lunar templates. There are multiple variants of this model that can be obtained from various combinations of the data sets that were used in the process.

1.7 Motivation and goals of this dissertation

This dissertation has the goal to understand the nature of the gamma-ray emission of Sagittarius A*, for this, we studied the emissions from the 4FGL J1745.62859, which is the source observed by *Fermi*-LAT that corresponds to Sagittarius A* (Cafardo et al. (2021)).

We are in an extraordinarily privileged location in relation to Sgr A*, which makes it a one-of-a-kind laboratory to investigate both the behavior of SMBH in the center of galaxies as well as the many influences that they can have on the environment around them.

Concretely, we build the Sgr A* SED using photons with energies ranging from 100 MeV to 500 GeV that were collected between August 2008 and June 2022. In addition to this, a detailed analysis of the systematic uncertainties connected with the creation of this SED are included. Further, we conduct an in-depth analysis of the data obtained from this SED and model them using a minimum of two different gamma-ray emission models. The model explored here is associated with leptonic particles.

By doing so, we will be able, for example, to identify the kind of particles that are responsible for the emission that we are witnessing, and how they interact with the environment that they resides in.

Chapter 2

Methodology and observations

2.1 The Fermi's maximum likelihood modeling

The method of maximum likelihood is at the heart of the *Fermi* analyses. By definition, the likelihood is the probability of obtaining the data given an input model. In the context of this specific research study, the model can best be conceptualized as the gamma-ray sky, complete with all of the sources that it contains, as well as their respective distributions and spectral characteristics.Therefore, in order to get the maximum likelihood, what we need to do is vary these various values, until we find it. As a result, we anticipate that the likelihood of obtaining the data from a model that provides a more accurate description of the underlying reality will be higher than the probability of obtaining the data from a model that provides an inadequate description.

In most cases, it is required to adhere to a procedure that is broken down into four distinct parts when conducting investigations of this kind. The first one is the appropriate selection of data to be used. In this situation, the most important thing for us to do is to collect data from a particular spacial region that is centered on the source of interest that we have. As a consequence of the huge PSF that *Fermi*-LAT possesses, this enables us to gather information regarding the SOI and about adjacent sources, a detail that is crucial for the development of a good model.

The second part is concerned with the selection of models. This includes complete information about the gamma-ray sky of the ROI used, and also the models for the diffuse gamma emissions. The *Fermi* collaboration is responsible for providing items such as these models of diffuse emission as well as a catalog of gamma-ray sky sources, as previously noted.

The precomputing of quantities that are required for the calculation of maximum likelihood is the third step in this procedure. Calculating certain quantities that can be done before beginning the analysis is extremely recommended because doing so prevents those quantities from having to be recalculated each time the parameters of a model are changed to be fitted. This is because the parameters of a model are indeed changed multiple times in order to maximize the likelihood and this will result in a reduction in the amount of time and resources spent computing.

Finally, the last part is where the fit is actually done. During this part of the procedure, a search is conducted to identify the combination of parameters that both maximize the likelihood and explain the data. Even in situations with a large parameter space, it is necessary for all of these parameters to be fitted.

Once the steps involved in this analysis are generally known, it will be required to learn and comprehend about the likelihood function, which is essentially what we're going to accomplish in the next section.

2.1.1 The likelihood functional form

A *Fermi*-LAT count - a valid event - is characterized by a sizable number of distinguishing characteristics. Among these, some of the most important include the time of detection, the energy and the direction of the detection. Because of this, the amount of time required to calculate the likelihood becomes prohibitive when we consider an analysis that covers a long period of time or a source that is not too faint. This is because that, in these instances, there is an extremely high number of counts that need to be considered.

Data binning is the approach that was taken to solve this issue. Particularly in this case, prior to carrying out the fit, the data are categorized into bins based on the count characteristics. Therefore, even if initially we have a large number of them, each bin will have a smaller number. The Poisson distribution is used to describe the distribution of the observed number of counts within each bin.

In light of this, the Poisson distribution can be expressed using the following format when applied to the scenario under consideration:

$$p_i = \frac{m_i^{n_i}\, e^{-m_i}}{n_i!} \tag{2.1}$$

Here m_i is the predicted number of counts of the i-th bin. This quantity is a function of the

model, and since, it follows that many models of a given source will each imply a different value for it. The n_i quantity, in its turn, provides us with the number of counts that were observed in each bin.

In this context as a whole, the likelihood L is given by the product of the probabilities of each bin, it follows logically from the previous equation that the likelihood can be calculated using the following formula:

$$L = \prod_i p_i = \prod_i \frac{m_i^{n_i}\, e^{-m_i}}{n_i!} = \prod_i \frac{m_i^{n_i}}{n_i!} \prod_i e^{-m_i} \tag{2.2}$$

The expression that we currently have can, however, be improved if we pay attention on the rightmost side of it. In light of this, the final term of this equation can be calculated as follows:

$$\prod_i e^{-m_i} = e^{-m_1} \times e^{-m_2} \times \ldots \times e^{-m_i} = e^{\sum_i -m_i} = e^{-N_{\text{pred}}} \tag{2.3}$$

This is a consequence of the fact that the total number of counts that the model predicts ought to have been detected is provided to us by the sum of the m_i. With this, we can then determine the best form of likelihood function for a binned analysis, given by:

$$L = e^{-N_{pred}} \prod_i \frac{m_i^{n_i}}{n_i!} \tag{2.4}$$

Based on the most recent representation of this equation, we can conclude that the likelihood can be expressed as the product of two terms: the first that is purely a function of the model used and the second that is a function of both: the model and the data. In a practical sense, our goal is to locate the combination of parameters that yields the highest likelihood, indicated by the equation 2.4.

Last equation can be rewritten in a different and potentially more friendly way, since maximizing the above equation is identical to maximizing the log version of it. From this, we have that:

$$\begin{aligned} \log L = l &= \log e^{-N_{\text{pred}}} + \log \prod_i m_i^{n_i} + \log \prod_i \frac{1}{n_i!} \\ &= -N_{pred} + \sum_i n_i \log m_i - \sum_i \log n_i! \end{aligned} \tag{2.5}$$

Because it is not related to the model in any way, the final term of the expression that was found above can be disregarded, simplifying all to:

$$l = \sum_i n_i \log m_i - N_{pred} \tag{2.6}$$

which is the final version of the equation with which the analyzes of this work were made.

In the case that the bins in question were infinitesimally small, we would deal with an unbinned analysis. If we were not constrained by computational resources, we could conduct this kind of investigation as thoroughly as possible. This argument can even be enhanced by considering the fact that, in this case, we would not lose any type of information, which is something that does eventually happen throughout the binning process due to the fact that there is data grouping. In the case of the likelihood, this would led to the simplified equation:

$$L = e^{-N_{pred}} \prod_i m_i \tag{2.7}$$

The main difference here is that m_i would be determined by making use of the exact value of each count rather than an average value, which is what occurs when we have binning in place. In a similar manner, the log-likelihood equation for the unbinned analysis would look like this:

$$l = \log m_i - N_{pred} \tag{2.8}$$

2.1.2 The likelihood approach and the model selection

One could say that the method that accounts for the maximum likelihood is efficacious. In essence, it not only offers the set of parameters that maximize likelihood, but it also provides errors associated with each of the computed values. In contrast, it does not offer a measure of fit quality, and the way we proceed with the analysis in this case is to compare one model to another and select the one that fits the data that we have available in the best way.

The hypothesis that permeates this argument is that, if we have a certain model with a higher likelihood, L, it represents a better option in describing reality than another model with a lower likelihood. The TS is the quantity used to do this. Its definition is:

$$TS = -2 \log \frac{L_{max,0}}{L_{max,1}} \tag{2.9}$$

here, $L_{max,0}$ represents the value of maximum likelihood for a model that does not include an additional source, known as the "null hypothesis", and $L_{max,1}$ represents the value of maximum likelihood for a model that does include an additional source and places it in a specified location.

To get a better grasp on how it operates, let's consider an example scenario in which we want to analyze and compare a certain model that does not have a source at a given position to a model that does have this source. What we need to do then is maximize the likelihood A for the model that does not have the extra source, and we also need to maximize the likelihood B from the model that does have the additional source. When that is finished, we will be able to compute the TS by using the equation from above. Therefore, as a result of the definition of likelihood itself, it follows that a larger TS will indicate that the null hypothesis is incorrect, which means that the model in which the source exists is a better explanation of the data that we have, and therefore, of reality.

A very practical result that indicates a meaning to the TS says, in fact, that (Mattox et al. (1996)):

$$\sqrt{TS} \approx \sigma \tag{2.10}$$

where σ represents the significance that the favored model has in comparison to the alternative. The conclusion that can be drawn from this is that the TS would be approximately the square of the significance of the source detection expressed in terms of standard deviations in the scenario that was used as an example earlier. This is even the meaning of TS that is most commonly employed.

2.2 Fermitools and Fermipy

The *Fermi*-LAT Collaboration provides two sets of tools that are of critical value for the work that is being done here. The *Fermi* ScienceTools, also known simply as the Fermitools, are the first grouping of this collection of tools. They are part of a larger collection of resources that were developed to facilitate working with data from *Fermi*. It is possible to find commands within it that allow for the temporal and spatial selection of data, the creation of counts maps, as well as the analysis of the data and the creation of models for further investigation. The user is able to carry out any form of study of *Fermi* data while using them, which implies that within a single suite, blazars and pulsars as well as any other source of gamma rays can be investigated. Within the context of this project, the version of Fermitools labeled as 2.2.0 was utilized.

The Fermipy package is the second group of these essential tools (Wood et al. (2017). It is essentially a Python package that wraps the Fermitools and brings them into Python

enabling the user to also have all the Python resources and packages at hand. With Fermipy in particular, analyses performed with Fermitools become simpler to carry out and more straightforward to reproduce. The Python version 3.10 and the Fermipy package version 1.1.6 were utilized in this project.

2.2.1 The likelihood and the Fermitools fitting process

As described earlier, to maximize likelihood we need to find a set of parameters that does it. Typically, a task like this takes place during the process of fitting. Fermitools, and by extension, Fermipy, contains algorithms that help in this duty. These algorithms are referred to as optimizers.There are five of them available to be used, and their differences can be summarized as follows: how quickly they converge to the function's maximum; the amount of computer power that is required; and how accurately they map the function's dependency near the maximum. In the specific scenario of Fermipy, only two of these five are accessible for user input and manipulation. The MINUIT and an updated version of it named NEWMINUIT. Following is a description of the primary concept behind how each of them operates.

An iterative approach is used to determine the answer that has the maximum likelihood. For each unique set of parameters, the log-likelihood value, l, is computed. Then, its derivative with respect to the parameters is computed in order to guide the algorithm's next choice of parameters, so that this causes the set as a whole to move closer and closer to the values that maximize l. This process is repeated until either an upper limit has been reached for the number of times it can be repeated or the difference in log-likelihood values between iterations is small enough to be considered acceptable. When it comes to sets of parameters that are deemed by the algorithm to be relatively close to the maximum region that is being searched, the algorithm carries out a special mapping of the function and its dependencies in order to provide the uncertainties that are associated with the parameters that make the best fit.

2.3 Data

According to the distribution policy of the *Fermi*-Lat Collaboration, the data that were utilized in this study are openly available to the general public. This data is obtained

from two separate files, namely the events file and the spacecraft file. Both of these files are required for any kind of analysis because they contain distinct but complementary kinds of information. From the first one, we are able to obtain fundamental parameters regarding the event that was detected by *Fermi*-LAT. Some of these parameters include the reconstructed direction, the angle of incidence, the energy of the incident photon, and the parameters that measure the quality of each of these indicators individually. We receive measurements of the telescope's position and orientation once every thirty seconds from the second, which provides us with information relating to the physical position and direction of observation of the telescope in space.

In order to carry out the analysis, the information included in the two separate files needs to be combined and synchronized. This is accomplished by making use of the tools that are found in Fermitools or directly using Fermipy. In the context of Fermipy, data selection information is transmitted to it via a configuration file that is written in the YAML language. With the raw data in our possession, the first thing we need to do is to make some selections within the data. Among them, the choices that stand out the most are the ones related to the range of energies with we will work, the intervals of time, the location of our source of interest (SOI), and the characteristics of our region of interest (ROI) with its size being our primary worry. The maximum zenith angle, as well as the event class and type that we will employ, are both also selected at this time.

In terms of energy limits, the selected values were, for the lower limit 100 MeV, and for the upper limit 500 GeV. In point of fact, our selection was made in such a way that it enables us to test for the presence of gamma emissions of hadronic or leptonic origin from our SOI, which is 4FGL J1745.62859, the gamma-ray counterpart of Sgr A* (Cafardo et al. (2021)).

Therefore, a lower bound that is less than 1GeV ought to be chosen, as it would allow us to observe in the event that it were there, the bump that was caused by pion decay. However, because *Fermi*'s angular resolution values and its effective area are both dependent on the energy of the incident photon, we were aware that if we chose photons with energy values that were lower than the aforementioned thresholds, the spatial quality of the analysis would deteriorate. Therefore, a value of 100 MeV, was chosen because it would allow us to see the presence, if any, of hadronic emissions from this source while also serving as a threshold for the spatial quality of the analysis. To a large extent, we

still relied on the expertise gained from the analyses performed in Cafardo et al. (2021) when making this choice. The criterion of greatest influence for the upper energy limit is connected with the number of photons that would need to be available in each band for it to be statistically significant. We are aware that the quantity of photons produced by our source, as well to those produced by any other gamma rays source, reduces as their energies increase (Longair (2010)). Therefore, despite the fact that *Fermi* can capture gamma photons with energies even greater than 500 GeV, was decided, pragmatically, to be used as the cutoff value for our work.

In terms of time intervals, the data that was used in this research begin with the first moment when data was collected by the *Fermi*-LAT instrument: August 4, 2008 at 15:43:36 UTC. The time range that was selected continue until 2022-07-15 00:00:00 UTC. As a result, the analyses cover about 14 years worth of data.

The ROI that was utilized is analogous to a square within the heavenly sphere, and each of its edges measures 15 degrees. The center of it is, by choice, the location of our SOI. Furthermore, the ROI is shifted Eastward by approximately 58.6 degrees in Galactic coordinates. The area of the ROI helps us to have a large number of captured photons, which is essential for our analysis, given that our interest is in the central region of the galaxy and many gamma sources exist there.

The determination of the maximum zenith angle is an another significant issue to think regarding the data selection. From the point of view of the data, this angle serves the purpose of excluding time intervals of collected data in which the Earth limb is very close to the ROI. Following the recommendation of the *Fermi* collaboration, the maximum value of the zenith angle used here is in this context is 90.

Regarding the photons event class, the one called P8R3_SOURCE is utilized for the analyses that were performed here. The reconstruction quality of a *Fermi*-LAT event and the probability that the event was in fact generated by an astrophysical photon are both taken into consideration when evaluating it. Therefore, the selection of this event class takes place as a result of the fact that it is able to provide good sensitivity for the majority of analyses involving point sources and is also beneficial for the analysis of sources that are moderately extensive. In the same way, the photons that are gathered by *Fermi*-LAT are separated into a variety of event types. Here we decided to use all of the available photons for our analysis, choosing them based on the four different PSF classifications: photons

from PSF0, PS1, PSF2, and PSF3. This decision was made in light of the fact that we needed to achieve a good statistical reliability and also as a result of internal discussions that took place during the course of the project with the *Fermi* Collaboration.

One further element to consider in relation to the selection of data is the IRF that was used. It is safe to say that each of the existing event classes has its own IRF; hence, the IRF that was applied in this investigation was the one that was linked to the event class that was selected. It is referred to by the name of P8R3_SOURCE_V3. This parameter, as was the case for the other elements, is communicated to Fermipy by way of the YAML configuration file.

Some other items of information about the data selection are also received. These includes the directory in which the spacecraft file and the event files that will be used in the analysis can be found and similarly, it is in it that the model of diffuse galactic emission and isotropic extragalactic emission are pointed, together, with the source catalog it should employ.

Frmo this point, Fermipy is prepared to begin. However, before the creation of the model itself, there are certain additional procedures that occur. The first one is the creation of what are known as Good Time Intervals (GTI) by Fermipy. A GTI is a time period within which the data gathered by *Fermi* is considered to be valid. This classification is done analysing the spacecraft file and is determined by two primary factors: the parameters we utilized in the data selection process, and the times when the telescope was operating normally and collecting data. From this final point, it follows that any and all time periods during which the telescope was undergoing maintenance or calibration are disregarded. The first point, on the other hand, is connected to matters of a more nuanced kind. In particular, we are aware that the telescope will aim in different directions across the sky as it travels its orbit. Parts of the observation intervals will not be regarded as a GTI because of its position, its orientation, and the seen sky region, since some kind of contamination may be present.

The orbit of the satellite around the Earth, as well as the orientation of the satellite at each time, might have an impact in the total quantity of photons that are delivered to us from the many sources that are being observed. That is to say, the number of events that are detected for a source of a particular intensity depends on the amount of time that source spends at each of a number of inclination angles throughout the course of an

observation. The amount of livetime, or the total amount of time that the LAT has been actively collecting event data, is another factor that will influence the number of events seem by *Fermi*. All of this information will be taken into consideration and computed during the construction of the so-called livetime cube, which, at its core, is a function of the position of the telescope in he sky and its inclination angle. This, to be crated, makes use of the spacecraft pointing history file in conjunction with the time range and GTI selections in the event file.

Even after that, it is still a standard step in this kind of analysis to produce an exposure map. They are essential for computing the projected amount of photons that are produced by diffuse components in your source model within a ROI. This specifically refers to diffuse galactic emission as well as isotropic emission from extragalactic sources. Conventional exposure maps, which are the integrals of effective area over time, are different from these maps in a number of fundamental ways. In this case, the calculation for exposure that is employed in the study is an integral of the whole response. This involves multiplying the effective area by the energy dispersion times the point spread function throughout the whole ROI.

2.4 About the modeling of the Region of Interest

Any modeling and analysis that is going to be carried out with *Fermi*-LAT data must first begin with the selection of data and the preparation that it requires. Because of this, the procedure in question was discussed in great detail in the section that preceded this one.As soon as the initial procedures have been finished, we may go on to begin the process of fitting the models to the data. This is something that needs to be done because, if we examine the data in their current state, all that we are going to find is a set of cluster of photons that points to the existence of sources. Here, the claims that we shall be able to make will be limited to the aforementioned point. As a result, the purpose of our modeling will be to correctly assign the photons that we have to each of the sources that originated them and are present in our ROI and to make the parameters that define each of these sources as close to reality as is possible.

2.4.1 About the ROI itself

The first thing we need to worry about with the model is our overall ROI. After the processes that were described in the previous part have been completed, we find in it photons that are mostly related with the following three things: i) the gamma ray sources that are recognized and identified by a LAT catalog that are in use and are contained within it, ii) photons from extragalactic diffuse isotropic emission, and iii) photons from the galactic diffuse emission. This suggests that at this point, we require knowledge regarding these three different components. Generally speaking, this set of information is supplied by the LAT collaboration.

The most recent and up-to-date version of the *Fermi* source catalog which was accessible was the one that was utilized for this project, this catalog was the one called 4FGL-DR3 (Abdollahi et al. (2020, 2022)). The information that is found in the catalog relates to the positions of the sources as well as the spectral models of those sources. It is important to point out that the spectral parameters of the sources contained in the catalog can be updated while modeling. The quality of the model that is built from the data can be then increased and improved as a result of this.

For the case of diffuse isotropic emissions and those of extra-galactic origin we used the model recommended by the LAT Collaboration for our data selection. For the case of diffuse galactic emission, we also used, initially at least, the model indicated by the collaboration.

Finally, in relation to ROI, it is essential to discuss its dimensions. The size of the sides of this region were determined so that we would not experience any difficulties as a result of the large PSF of *Fermi*-LAT, particularly at low energy levels. Nonetheless, it is valid to note that the more away we are from the SOI, the less influence the sources from there will have; hence, this is a physical argument in support of limiting the size of the ROI itself.

When carrying out an analysis such as ours, it is imperative that we find a suitable equilibrium between the size of the ROI and the number of sources and data that it contains. This is due to the fact that the analysis requires a greater amount of computational resources in proportion to the size of these last two factors. However, there is no one and only one way to specify the size of the ROI to be employed, so this cannot be done unequi-

vocally. In point of fact, this is something that is done on the basis of empirical evidence, taking into account the factors that were just made and discussed in addition to testing and experience. In the process of creating the model, data from sources located in a region that was significantly larger than the ROI was included. In this approach, we take into account all of the sources within a region that is otherwise identical to ROI, except that the side is set to 20 degrees. This is because we can view external sources as generators of some of the photons that are in the ROI, which is indeed the situation in reality.

2.4.2 About the model creation

In the course of our project, we utilized Fermipy to carry out a binned likelihood analysis. A binned likelihood analysis is the approach of choice for the vast majority of different LAT analysis types. The data was divided into bins with a pixel size of 0.1 and into 8 logarithmically spaced bins per decade in energy. During this procedure, we carried out a joint likelihood analysis taking into consideration the various types of events PSF0, PSF1, PSF2, and PSF3 that were selected before.

The execution of a Fermipy method known as *optimize()* is the initial step in this process of generating the model. This method will automatically optimize the ROI by ensuring that all the sources that are present in itw will have a fit. This is done using an iterative methodology. During the course of its execution, the optimize method is responsible for carrying out three distinct operations. The first one is to carry out, simultaneously, the normalization fit of the N brightest sources of the model. These sources are selected in such a way that, when their individual counts are added together, the overall value of these sources is equivalent to a percentage, here 95% of the total number of counts that the model has predicted. The second operation consists of fitting the normalization of any and all sources that were left out of the first step of the process. Finally, the final step of the procedure that is being explained is to carry out an individual fit of the normalization and the index (or shape) of each source of a particular set. This set will be defined by containing all of the sources that have a Test Statistics (TS) value that is higher than a threshold value indicated by TS $>$ shape ts threshold $= 25.0$.

The next step in enhancing the model is applying Fermipy's *fit()* method to specific sources in order to get a better fitting of them. This method will do a fit in likelihood optimization mode on all of the model's free parameters. In addition to this, it performs

updates on the characteristics of parameters that correspond to the model. This means that it updates, among a lot of others, the spectral parameters, the TS of a source and its N_{pred}. On the other hand and in contrast to what takes place during the optimization approach described above, here we liberate, in accordance with our criteria, the source parameters that will be go in the fitting process. Because of the large number of sources that are present in our ROI, it is imperative that such processes be carried out with caution in order to prevent the fit from failing to converge and the loss of exhaustive and laborious computational work.

2.4.2.1 The construction of our best model

For the construction of our best model, experience led us to make the various sources go through 20 different rounds of what was called analysis-fitting groups (AFGs). These analyses and fittings can be seen as groups that bring together a certain number of fits, with each of these fits being carried out according to certain free parameters, and with the majority of them having some particularities in relation to the others. In the next paragraphs there is a general description of each one of of these AFGs.

A predetermined number of sources is chosen for examination for each of the AFGs. This initial group of sources is subdivided in a way that avoids computational and convergence problems. If we have many free parameters (for example, more than 15-20 in some cases), we will not achieve a good convergence, and the process as a whole will need to be redone. Once the subdivision of sources is done, the parameters that must pass through the fitting are freed. Then, these sources will be fit by the MINUIT optimizer if the fit, within the current AFGs matches an even number, and by NEWMINUIT if it matches an odd number. This strategy was adopted with an intention of maximizing the use of available optimizers, so that we could take advantage of both.

From the group of sources undergoing a fitting, one of these sources is removed from that group, indicating that it obtained a good fitting using two different criteria: How much the value of its TS and N_{pred} varied in each fitting. If a source's values for these parameters change by less than the limit that has been imposed, then the source is eliminated from the subgroup, and the fitting procedure continues.This will repeat until the subgroup equals the empty set. After that step is completed, the fitting process continues on to the subsequent subgroup of sources, which will experience the identical processes as before. This process

will continue until all of the subgroups of sources have been fitted. As soon as that is accomplished, the current cycle of AFG is ended.However, the procedure that was just detailed has the potential to result in an endless loop if there is no restriction placed on the maximum number of possible fittings in the event that a particular source does not remain within the restrictions that have been established after a number of consecutive fit. Therefore, it is required here that, if after 15 valid fittings a source does not fall within one of the imposed limits, then it is removed from the subgroup to which it belongs, and it is left to be analyzed, if necessary, in an individual manner at a later time. Moreover, as is naturally to be expected, indeed sometimes several iterations were made on the sources that were being fitted. This was the scenario mainly in the case of the brightest and closest sources to the SOI.

In order to better take advantage of this whole process we took into consideration just the most promising possible fits, and not all of them are considered valid. In practical terms, only those that Fermipy categorized as having Status: 0, indicating that the process of fitting converged, and Quality: 3, indicating that the optimizer generated a completely accurate covariance matrix were taken into consideration. This was a check that had to be performed at every occasion to assure we would have a valid fit.

In the first AFG, a fit was performed on all of the pre-existing sources in the ROI. Their respective distances from the SOI served as the basis for the sequence in which they were organized. 13 distinct sources each had their normalizations fitted in each analysis. Three of these sources formed the main triad (MT), which was composed of the SOI, the diffuse component of the galaxy, and the isotropic extragalactic component of gamma ray emissions. The remaining 10 sources were grouped in accordance with the algorithm that was described earlier. The MT was always kept present to be re-fitted in every time, implying that, from each group, 10 sources were exchanged each time.

In the second, all sources were fitted again. However, they were now arranged in a new manner, based on the value of the TS parameter that was assigned to each one of them during their last fit. As was the case previously, every group that was going to have its normalization fitted was made up of 13 sources, the MT and 10 other. In turn, the third and fourth AFGs were replicas of the first and second groups, respectively. This step is taken at this juncture to make certain that, before moving further with the process, we will have a good overall fit for the ROI as a whole.

In the case of the fifth AFGs there is a particularity. Before the fitting process, a search for sources that may not be recognized in the catalog we are using was done. The strategy is to take advantage of the *find_ sources()* method that Fermipy provides. This approach operates, in general, by including a putative source in each of the several possible spots that are available within the ROI. Therefore, the TS of the model is computed wherever the putative source is present in a new site. Because optimizing the TS is the same as optimizing the likelihood in the region where we are working, as follows from its definition, that states that it is a monotonically increasing function of the likelihood $L_{max,1}$, whenever the TS value rises above a predetermined threshold, this indicates that there, in that position, additional sources may need to be included. To continue, at this point in the process, a fresh analysis of all of the sources that were present in the ROI was carried out. During this, they were arranged once more into groups according to the distance from the SOI, and as is customary, each group contained 13 different sources: MT's 3 and ten others. At this stage, only the normalization of each one of them was freed to be fitted.

Now, between the sixth and tenth AFGs not all sources were fitted. In each of them, the sources were arranged in descending order of their distance from the SOI, and the typical groups of 13 sources were utilized. The only parameter of these sources that was fitted was the normalization. Well, instead of having all of the sources to be fitted, we created circles centered on the SOI with radii of different sizes so that we could guarantee that the sources closest to the SOI were as well fitted as possible. In the sixth case of the AFGs, the sources fitted were located within a circle with a radius of nine degrees from the SOI. This circle's radius was 8 degrees when it was the seventh case. In the eighth case, the value of this radius was reduced to 6 degrees, and in the ninth case, the value was reduced to 4 degrees. The tenth case, in turn, reached the value of the radius equivalent to 2 degrees.

In order to continue, it is important to point out that in every one of the scenarios described above, a specific source was removed from the group that was being fitted whenever the difference between its new TS value and its previous one was less than 15 or the difference between its new N_{pred} and the older one was less than 3%. Between AFGs eleven and fourteen, the parameters that removed a source from the group that was being fitted became tighter so that the process as a whole had better outcomes. This was done to obtain a higher quality of fittings as well as a more resilient model. Specifically, in instance

eleven, the maximum variation limit of TS was reduced to 10%, while that of N_{pred} was reduced to 2%. In case 12, these values were brought down to 7% in the TS case and to 1.8% in the N_{pred} case. AFGs 13 and 14 both had a maximum acceptable variation value of 1.5% for N_{pred}, and kept the value of 7% for the TS case. These last values were the ones used in all other AFGs from here on.

It is convenient to point out that not all ROI sources were accounted for in the cases of any of the AFG 11-14. As was the circumstance with the cases that were detailed above, here a portion of these sources was chosen by defining a circle whose center coincided with that of the SOI. This circle had a radius of six degrees between the eleventh and thirteenth AFGs while the fourteenth saw a reduction in this radius to 4 degrees. Furthermore, the normalization was fitted once more for a set of 13 sources. Ten sources each time in addition to the MT. Finally, it should be noted that in this case, the sources were organized according to the TS value associated with them, so that those with higher TS were looked at before those with smaller TS.

In the fifteenth AFG, the analyses started to take into consideration also the indices connected with the spectral laws that described them, implying that at least two parameters per source would be looked at. Because of this, the number of sources that went to the group that would go through the fitting together decreased; there were now the three from MT and 8 more. These eight sources came from a big group of sources that were found inside of a circle with SOI serving as its center and having an 8-degree radius. However, there was an additional distinction that was present in this selection process. The photon number that was associated with the sources being selected had to be equal to at least 3 percent of the photon number that was associated with the SOI. As in previous cases, they too were organized through the TS value.

In cases 16 and 17, we have a choice of parameters analysis that are essentially the same as the ones from the prior case; the only differences are the size of the radius of the circle that was used to pick sources and the percentage of photons from a certain source in comparison with the SOI that were necessary to be selected. For case 16, the radius was 6 degrees, and to be selected a source needed to have at least 3.5% as much photons as the SOI. Regarding scenario 17, these values come in at 4 degrees and 1 percent, respectively.

In the second-to-last case, once again, we have a copy of the previous case selection and fitting parameters, with the difference, in relation to case 17 only in the radius used in the

source selection circle: here 2 degrees was adopted. In the penultimate one, a one-degree radius was employed around the SOI for source selection, but the additional criterion that compared the quantity of photons from sources within it to that of the SOI was left out of the computation. The rest of the parameters for the selection and the fitting were once more exactly the same. In AFGs group number 20, the last one, significant changes occurred in relation to the selection criteria used in the others above. Here sources with $TS > 200$ were taken to be fitted and the others weren't. Also, instead of a group of 11 sources to be fitted at a time, here the set of sources that would pass together in a fit has been decreased. There were three MT sources and only 4 others.

It is also important to point out that this method as a whole was established and refined via the accumulation of experience, and this ensured that the total ROI sources, 316, were properly accounted for. Anyway, in the case of a ROI as the one investigated in this work, there is no such thing as an optimal type of recipe that can be used to construct the model. However, the algorithm that was described above helped us create a good model for our problem and served as parameters for all of the analyses that we did. It is possible that there are other ways to analyze this ROI and arrive at similar results, but this was the one that we found out.

2.4.3 Evaluating the quality of the model

The process of evaluating each fit that was performed while the model was being created involves a variety of different indicators. The likelihood value that has been assigned to the model that is being considered is one of these indicators. An increase in likelihood in comparison to a previous model is a condition that is required for us to have a better model; however, it is not sufficient.Additional pertinent indicators include the diagnostic plots that are generated after each fit round. These plots include the residual maps, the TS maps, and the residual histogram.

Starting from a gamma ray model, one of the diagnostic plots that we can generate is the residual map. In a straightforward manner, we can define it as the operation of subtracting modeled counts from real data. Figure 3.3 displays one of them, which is going to serve as an example moving forward in the discussion. Maps of this type serve the more pragmatic purpose of assisting us in determining how good a certain fit is. In it, the colors indicate the significance of the residue in each pixel, calculated according to

the definition given above. Therefore, regions in the ROI sky that have positive residuals represent locations in which the model made an under-prediction, whereas regions with negative residual values suggest locations in which the model made an over-prediction. In this way, we discover with them regions that need to be treated with greater care.

The TS Map is another diagnostic map that can be created and utilized in diagnostic work regarding the fit quality. Its primary purpose is to help us evaluate the level of quality of the fittings we have. The TS Map that is displayed in Figure 3.4 is a illustration of this tool. In a nutshell, this map is constructed by placing a putative source in the most varied positions across the ROI. Every time anything like this is carried out, a maximum likelihood fit is calculated and to construct the map as a whole, we make use of the TS value that was estimated in this point, based on the existence of the putative source in each pixel. In these maps, the colors indicates the TS value at a given position. If we use such a map and, for instance, remove the central source from the ROI because it is our SOI and it is fully incorporated into the models, then we will have possible indications of particular locations or regions where the presence of a new source may be seen. Therefore, if we combine this kind of information with that of the previous map, we will have powerful instrument to direct us to locations that need to be properly analyzed and modeled.

One final diagnostic map that we are able to use is essentially a histogram that provides us with the residual distribution of the ROI. One example can be seen at Figure 3.1. In the ideal scenario, the distribution of this kind of residual should resemble that of a normal distribution, which has a mean $\mu = 0$ a standard deviation $\sigma = 1$. Each of the histogram bars in this map shows the probability, expressed as a percentage, of finding a particular pixel in the residual map that has a significance equal to that which is displayed along the horizontal axis. In particular, the significance of a pixel is determined by calculating its standard deviation relative to the average value of all other pixels in the image. There, the black curve represents the ideal Gaussian distribution that was described previously, and the red curve represents the Gaussian distribution that provides the best fit to the data that we have. When we consider our ROI, this plot basically tells us how near we are to a perfect environment or how far away we are from that ideal situation. Therefore, for our model to be improving, we should see an approximation of the distribution that describes our data to a normal distribution in each step.

2.5 Building a Spectral Energy Density

The creation of the Spectral Energy Density (SED) for our SOI, is an important element of the work that was carried out here. Because of this, below there is an explanation of how the SED is constructed by Fermipy making use of the data that we have and the model that we generated.

Although there are some parallels to the procedure that we followed in order to generate the model, the data in this case are partitioned in a different way. Specifically, we now have the data organized into energy bins. At the end of the SED evaluation, we will have a single point for each of these energy bins. Then, for example, a SED with 10 points corresponds to a SED created with a bin count of 10.

In order to produce the SED, we make advantage of Fermipy's *sed()* method. The SED is computed by carrying out independent fits for the flux normalization of the source in each of the energy bins. Since the spectrum of the source whose SED is being built and which was achieved through the numerous fittings made before during the model creation is used here as prior, the model created is a fundamental key that is also needed at this point.

In the investigation that we carried out, the SED was divided into 30 bins, which is the same as dividing it into 8 bins for each decade of the energy band that we are examining (100MeV-500GeV). This choice of parameters is associated with the operation of the *Fermi*-LAT: because the resolution of the telescope varies with energy, we had to choose a number of bins that at the same time was large enough to contain a number of counts that would be able to provide statistically significant results and that adequately captured energy dependence.

Regarding the procedure for developing the SED, there are two more aspects that should be brought to your attention. The first one is that it is possible to release parameters from other sources during the process of generating the SED. Due to the fact that the fitting of these released sources throughout this process of the SED creation can have an effect on the outcome of the SED itself. The second is that in order to lessen the overall level of systematic uncertainty, each and every one of the analyses here needs to be carried out utilizing the energy dispersion correction that is offered by Fermipy.

Chapter 3

The Spectral Energy Density of Sagittarius A*

The major goal of the entire process of selecting and defining the ROI and carrying out numerous fits to acquire the best model of gamma emissions from the galactic center was to have a reliable model that could be used to construct the SED of Sgr A*. This is due to the fact that SED gives us crucial information regarding the emission of a certain source. As a result, every step we took to create the most stable and reliable Sgr A* SED to date is described in detail in this chapter. In all scenarios explored, the *Fermi* space telescope observed gamma radiation from this source between August 2008 and July 2022 and the data has an energy ranging from 100 MeV to 500 GeV.

3.1 About the fiducial SED

In the previous chapter, the entire model and SED construction process was described. However, this description, although providing all the necessary steps to replicate the results we obtained, is somewhat general. Therefore, here we will provide the details inherent to this analysis.

To create the fiducial version of the SED the most recent tools and resources offered by the *Fermi*-LAT collaboration were used. This set of information is presented in Table 3.1 for convenient reference. It was decided to use all of the photons included in the LAT

Model parameters	
Energy range:	100MeV-500GeV
Date interval:	Aug/2008 - July/2022
Catalog:	4FGL-DR3
Photons PSF:	0+1+2+3
Galdiff:	gll_iem_v07
Isodiff:	iso_P8R3_SOURCE_V3_v1

Table 3.1 - Set of model configuration and selection parameters used in the creation of the fiducial SED

database given the energy range we fixed. This is attested by our choice to use photons with PSF0, PSF1, PSF2 and PSF3 in our analysis. Also, we decided to employ the most recent version of the galactic diffuse emission model, or galdiff, known within the collaboration as gll_iem_v07. The most recent version of the extragalactic diffuse isotropic emission model, or isodiff, that is suitable for our data is the one called iso_P8R3_SOURCE_V3_v1, and for that reason it was used here.

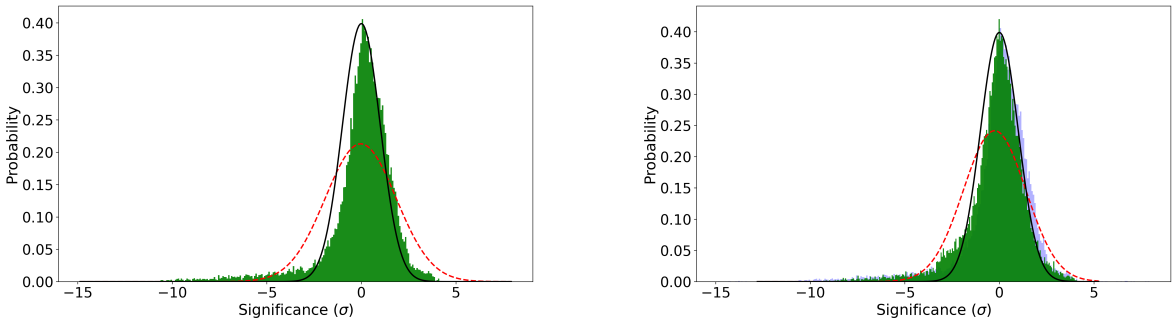

Figure 3.1: Residue histograms used as fit quality assessment tool, for the whole ROI. On the left, we have the histogram corresponding to the first fit executed in the construction of the model for the fiducial SED. The red curve is characterized by having a mean $\mu = -0.03$ and standard deviation $\sigma = 1.9$. On the right, we have the histogram corresponding to the last fit executed in the construction of the model. Here the red curve has a mean $\mu = -0.2$ and standard deviation $\sigma = 1.7$. The data set in blue in this histogram is the same as the one on the left plot, placed there to facilitate comparisons. In both cases the black curve is the ideal normal distribution, with mean $\mu = 0$ a standard deviation $\sigma = 1$.

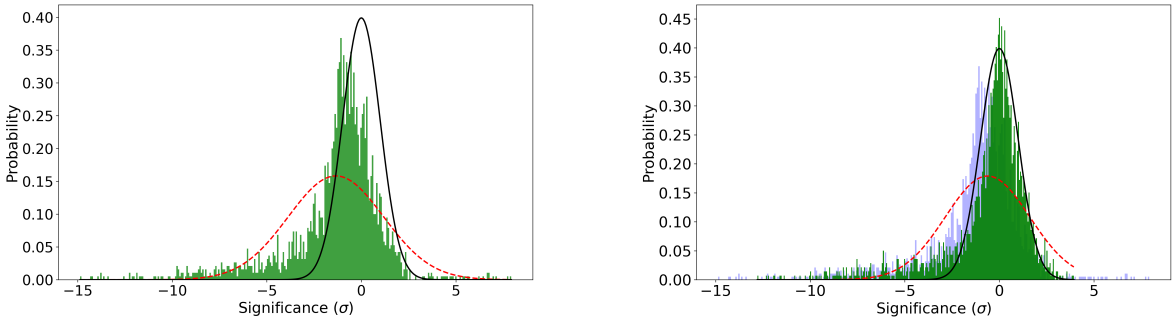

Figure 3.2: Residue histograms used as fit quality assessment tool, for a square region of the ROI, centered on the SOI and with sides measuring 5 degrees, everything else the same. On the left, we have the histogram corresponding to the first fit executed in the construction of the model for the fiducial SED. The red curve is characterized by having a mean $\mu = -1.3$ and standard deviation $\sigma = 2.5$. On the right, we have the histogram corresponding to the last fit executed in the construction of the model for the same region. Here the red curve has a mean $\mu = -0.6$ and a standard deviation $\sigma = 2.2$. The data set in blue in this histogram is the same as the one on the left plot, placed there to facilitate comparisons. In both cases the black curve is the ideal normal distribution, with mean $\mu = 0$ a standard deviation $\sigma = 1$.

With this selection made, the model for the galactic center region was created as the initial step for the construction of this SED. We completed this process once 405 valid fits of the relevant region had been performed using the algorithm outlined in the preceding chapter.

3.1.1 Model fit quality discussion

A model analysis should be performed using the available tools to ensure that the model being utilized is of high quality before building the SED itself. This is important since it is the model that provides the initial value of the parameters that are necessary and analyzed in the construction of the SED.

The histograms present at Figure 3.1, which informs us about the residue existing in our ROI as specified in the preceding chapter, will be examined as the initial step in this analysis. In the plot on the left, we can see the residuals' distribution in the ROI immediately following the initial fit round. The black curve denotes a normal distribution - the ideal case for our data, while its red curve represents the distribution which best describes the data. When compared to the ideal condition, it is seen that the distribution is somewhat displaced to the right. From this we know that at this time, the created model was unable to properly distribute the measured photons across the ROI sources since positive residuals signify a model under-prediction. Practically speaking, we should interpret this information as indicating that our model needs to be improved because it is currently unable to predict all of the photons that were detected, in a general way. Here, the red curve has a mean $\mu = -0.03$ and standard deviation $\sigma = 1.9$.

The histogram of the distribution of residuals following the most recent set of fits is shown on the right plot of the Figure mentioned above. From a broad perspective, it shows that the distribution was shifted to the left, bringing us closer to the ideal scenario. This implies that our model's predictions improved and that, in fact, it was enhanced after all the rounds of fits done. Yet, the residual data present in this plot show that there are some places in which the model makes an over-prediction, meaning that it assigns more photons to some parts of the ROI than were actually detected there. Despite the fact that this suggests that the model may be improved, there were primarily three factors that led us to choose to end the fitting process at this point: i) A considerable improvement in the model, when looked at globally. ii) Using the algorithm outlined previously, we had

already completed a thorough fitting of the ROI before we got to this point. This indicates that the sources, particularly the ones closest to SOI, the most important and relevant ones, were fitted multiple times. It was then apparent that additional fittings were not significantly improving the model. iii) The majority of the places in which we have the lowest residual values are scattered along the galactic plane, as shown when we combine the information supplied here with the residual map that will be covered later. This means that the inferior fitting suggested by these residuals is not solely a reflection of the model, but rather a result of the galdiff, which, while good, does not perfectly capture reality of the Galactic Center. Here, the red curve has a mean $\mu = -0.2$ and standard deviation $\sigma = 1.7$.

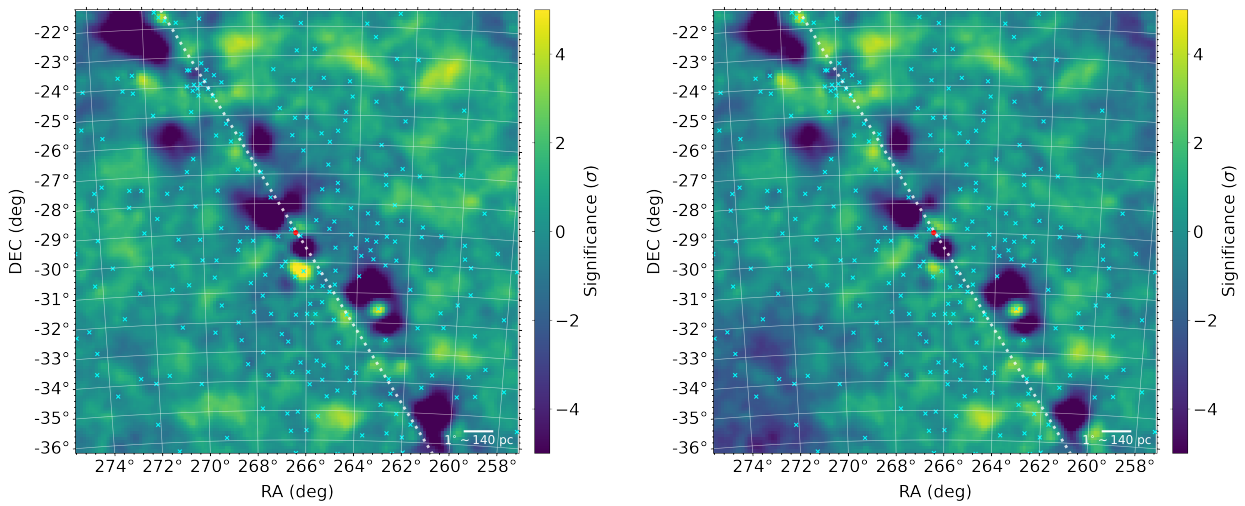

Figure 3.3: Map of residuals, used as fit quality assessment tools, corresponding to the first and last fit of the model used to build the fiducial SED. On the left, there is a greater concentration of areas that need improvement in the model, indicating regions of under- and over-prediction. On the right, there is a smaller concentration of them, with the exception of the galactic plane region, whose problems are related to the nature of the region and the galdiff model we have.

Within the ROI, the brightest and nearest sources to the SOI are those that are most crucial and relevant for the model. For this reason it is also worthwhile to perform a quick study of the residual distribution using only the ROI's central region rather than the ROI as a whole. To achieve this, we clipped the original ROI to create a new analyzed region that is equally square and centered on the SOI, but now has sides that are 5 degrees wide.The two histograms in Figure 3.2 display the residuals of this area, again for the first

and last fit performed.

The plot on the left makes it clear that the situation in this area was far from optimal. What is even noticeable is that there is a large concentration of over-prediction by the model in this region. The data here as described by the the red curve has a mean $\mu = -1.3$ and standard deviation $\sigma = 2.5$. The plot on the right, differently, shows that a process of building and improving the model took place, since it is now closer to the ideal situation. In contrast, even despite being downsized, it can be observed that there is still a left tail in the histogram that displays the final panorama of the analysed region, causing it to be extended to negative significance levels. The reasons for the existence of this tail are the same as those discussed for the previous case, and once again, we think that the outcome is more tied to the galdiff and our ability to adequately model the galactic plane region more than anything else. In this case, the normal curve describing the data has a mean $\mu = -0.6$ and a standard deviation $\sigma = 2.2$

Two residue maps are shown in Figure 3.3. The one on the left represents the residual map just after the first round of fitting, while the one on the right is the same map just after the last round of fitting. In both cases, the scales were normalized so that the maximum and minimum significance values became, respectively, 5 and -5. As was already said, these diagnostic plots are crucial tools for evaluating the model's quality. It is particularly important to note that the region associated to the galactic plane, which is clearly outlined in the plots, is the most intricate region in both cases. Again, this is a reflection of our limited comprehension and difficulty in fully understanding the center region of our own galaxy as well its galactic plane. Nevertheless, we need to explore into this a bit further. The first thing to note is that the majority of the issues in this region are caused by locations where the model predicts a gamma ray flux that is higher than what was actually observed by the telescope, although regions with flux smaller than those detected by the telescope also exist. Furthermore, if a gamma source was present in these places, the situation could be handled more efficiently from the standpoint of forecasting and detecting flux other than observed flux, since it would probably be enough to try to make particular fits for the sources in question. Since this is not the case, these regions are much more difficult to treat. Additionally, the location of these regions in space and the absence of sources in them clearly suggest that these are regions that are associated with galdiff emissions.

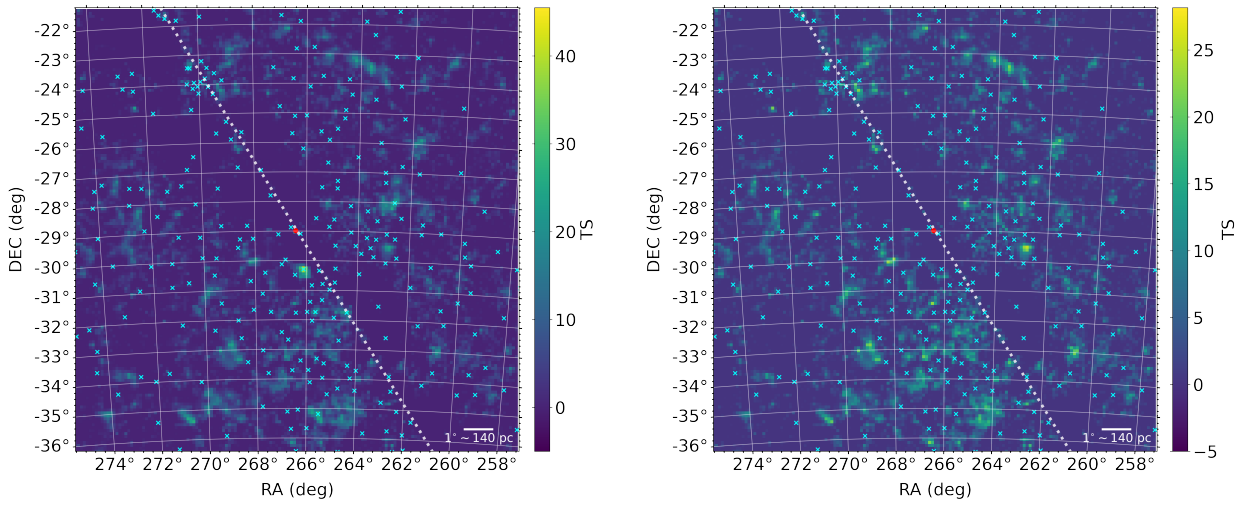

Figure 3.4: TS maps, used as fit quality assessment tools, corresponding to the first and last fit of the model used to build the fiducial SED. On the left, you can see regions with TS $\sim$ 40 indicating places where the model needs improvement. On the right, a more homogeneous distribution of regions with detected TS is seen, with lower absolute values, indicating a general improvement in the model used.

Pragmatically speaking, it is feasible to observe that the regions in the left plot that have residuals close to the limit values are greater than those in the right plot. This shows that the model genuinely benefited from the changes we made in it during the fittings. Also, regions with significant values towards the extremes of the plot on the left are a clue that the fit in those regions needs to be improved. For instance, the extremely under-predicted region immediately to the south of the SOI fades in the plot on the right compared to the one on the left for this reason, demonstrating the effectiveness of the applied fits algorithm. We can see that when compared, the results shown in these residual plots with the ones presented in the histograms shown in Figure 3.1 are consistent.

The TS map is the final diagnostic plot that needs to be examined in order to assess a goodness-of-fit. Figure 3.4 displays the TS Map for the first and final fits made during this analysis. The plots in this image were created by placing a putative source at various ROI locations and calculating out the maximum likelihood, with the particularity of having SOI included in the model, indicating a scenario in which its existence would be guaranteed. Similar to earlier situations, the information offered by this kind of plot assists to highlight ROI spots that require more care. If one of them has a region that sticks out because of the TS values allocated to it, a fresh fit should probably be performed on that area.

However, this should not be considered individually, and a comparison between TS maps from different fittings also needs to be done. The existence of a few highlighted spots and an overall decline in the map's TS values in this case are definite signs that the model building process is progressing.

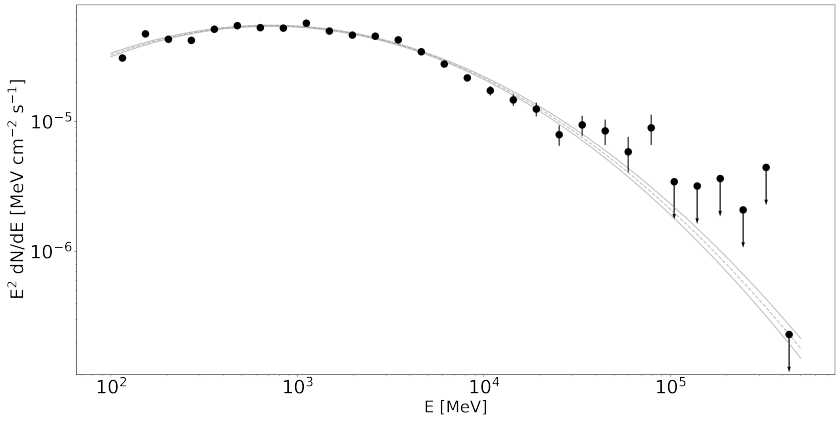

Figure 3.5: The fiducial SED. Built with photons of energy between 100MeV and 500GeV, and from observations between August 2008 and July 2022 and with the selection of parameters described in table 3.1. The curve is described by a log-parabola with parameters $\alpha = 2.57 \pm 0.02$, $\beta = 0.133 \pm 0.005$, $N_0 = (8.0 \pm 0.1) \times 10^{-13}$ cm^{-2} s^{-1} MeV^{-1} and $E_0 = 6113$ MeV. In grey, there is the best fitting curve from the model data accompanied by 1σ errors.

Comparing the TS maps of the two different fits in this instance, we can observe that the TS values have actually dropped overall. This is evident when observing that, despite sharing the same colors, each scale's maximum value varies, with the scale of the first fit reaching a maximum value of $\sigma \approx 45$ and that of the second at $\sigma = 25$. Despite this, there are a few locations on the TS map of the plot shown to the right that could be interpreted as areas that eventually would be benefited from improved fittings but The result observed in this TS was something that was essentially not changing as the procedure went on. In this sense, when we consider the information together with the other diagnostic plots, they are actually the best results we were able to obtain.

3.1.2 The fiducial SED

Using the information that was previously covered, we constructed the SED by adhering to the last chapter's description. The SED is displayed in Figure 3.5. The gray line in this graphic represents the log-parabola equation for the source's spectral model provided

Model parameters	
Energy range:	100MeV-500GeV
Date interval:	Aug/2008 - July/2022
Catalog:	4FGL-DR3
Photons PSF:	0+1+2+3
Galdiff:	gll_iem_v05_rev1
Isodiff:	iso_P8R3_SOURCE_V3_v1

Table 3.2 - Set of model configuration and selection parameters used in the creation of the SED using an old galdiff model

by the model that we made for the ROI and it is constrained by the 1σ uncertainty. The errors represented in the flux also correspond to the uncertainty of 1σ but they come from the likelihood maximization operation of the SED generation process itself. In descriptive terms, a log parabola with parameters $\alpha = 2.57 \pm 0.02$, $\beta = 0.133 \pm 0.005$, $N_0 = (8.0 \pm 0.1) \times 10^{-13}$ cm^{-2} s^{-1} MeV^{-1} and $E_0 = 6113$ MeV provides the best fit for the dataset acquired. The E_0 parameter has no error because it was kept fixed throughout the process.

In the setting just given, this SED could potentially be interpreted as the finest SED for Sagittarius A* in the band thought to have been constructed thus far. But, as was already indicated, the ROI model that was employed in its design is strongly related to galdiff. In order to further explore this result and strengthen it, we will discuss the construction of other SEDs that are derived from ROI models other than the one employed here.

3.2 Exploring some others SEDs

The idea here is to present two others SEDs, built from models that use previous versions of galdiff, in order to verify their influence on our result. Like it was before, the text that follows will include a succinct description of the model developed along with pertinent remarks about the model's fit quality before the SED is shown.

3.2.1 SED built from an old galdiff model

As was the case in the previous section, we construct a model for our ROI by making use of virtually all of the most recent resources and tools that have been made accessible by the *Fermi*-LAT collaboration. The only exception to this is the galdiff, whose version that was utilized was the penultimate one that was available: gll_iem_v05_rev1. In table 3.2, information on the resources used and the selection of photons used is available for

consultation. From this perspective, the model for the central portion of the galaxy that was generated was obtained by applying the procedure that was discussed in the prior chapter and a total of 455 valid fits were made to arrive at the best possible scenario for this model.

It is essential to note out that the galdiff that was used in this instance, despite being an older model, was constructed in almost the exact same way as the most recent one.The quality of the templates that are available is what differentiates the two, as our knowledge of the area is intimately connected to this aspect of the process. When more time passes, we gain a better understanding and recognition of it, allowing us to obtain more precise information.

3.2.1.1 Model fit quality discussion

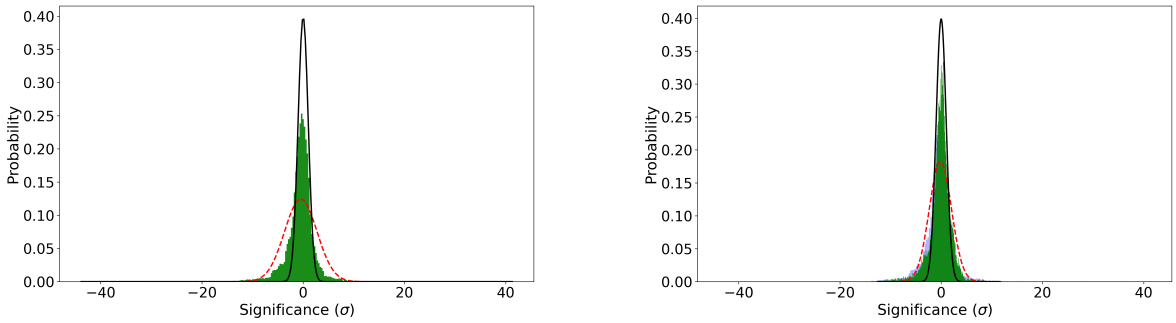

Figure 3.6: Residue histograms used as fit quality assessment tool, for the whole ROI of the model used to build the SED with and old galdiff. On the left, we have the histogram corresponding to the first fit executed in the construction of the model for the fiducial SED. The red curve is characterized by having a mean $\mu = -0.5$ and a standard deviation $\sigma = 3.2$. On the right, we have the histogram corresponding to the last fit executed in the construction of the model. Here the red curve has a mean $\mu - 0.2$ and a standard deviation $\sigma = 2.2$. The data set in blue in this histogram is the same as the one on the left plot, placed there to facilitate comparisons. In both cases the black curve is the ideal normal distribution, with mean $\mu = 0$ a standard deviation $\sigma = 1$.

In terms of the fitting quality analysis, we have three indicators that may be accessed through diagnostic plots. In the case of the first one, in order to see evidence that the fitting is progressing towards better outcomes, the given histograms need to move in the direction of approaching the ideal normal distribution. When we compare the histograms of the first fitting with those of fit 455, as shown in Figure 3.6 left and right, we find that this is the case here. In the left plot, the red curve that best describes the data has a mean

$\mu = -0.5$ and a standard deviation $\sigma = 3.2$, whereas on the right plot, the red curve has a mean $\mu - 0.2$ and a standard deviation $\sigma = 2.2$ suggesting that the process of constructing and enhancing the model progressed.

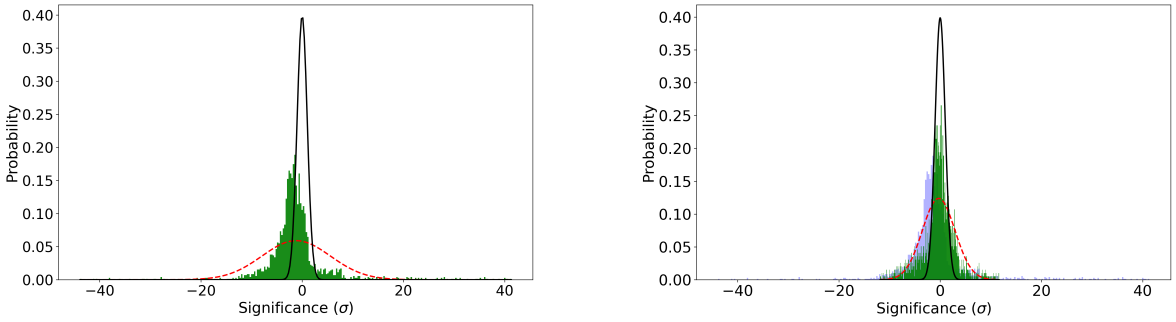

Figure 3.7: Residue histograms used as fit quality assessment tool of the model used to build the SED with and old galdiff, for a square region of the ROI, centered on the SOI and with sides measuring 5 degrees, everything else the same. On the left, we have the histogram corresponding to the first fit executed in the construction of the model for the fiducial SED. The red curve is characterized by having a mean $\mu = -1.2$ and a standard deviation $\sigma = 6.8$. On the right, we have the histogram corresponding to the last fit executed in the construction of the model for the same region. Here the red curve has a mean $\mu = -0.3$ and a standard deviation $\sigma = 3.2$. The data set in blue in this histogram is the same as the one on the left plot, placed there to facilitate comparisons. In both cases the black curve is the ideal normal distribution, with mean $\mu = 0$ a standard deviation $\sigma = 1$.

In a similar fashion, the information that can be gleaned from the histogram data that can be seen in Figure 3.7 and leads us to the same conclusions. In this instance, the smaller region that is being addressed is the same as the ROI subregion that we had above. In this situation, the normal curve that most accurately reflects the data in the left histogram is characterized by an mean $\mu = -1.2$ and a standard deviation $\sigma = 6.8$, whereas the normal curve that most accurately describes the data in the right histogram is defined by a mean $\mu = -0.3$ and a standard deviation $\sigma = 3.2$.

This diagnostic plot shows that the final model we have was indeed able to correct various over- and under-prediction regions that were originally present in the ROI, mainly in the central region. In addition, it is important to point out that when compared to the prior scenario of the last section, these disparities in the observations and in the values predicted by the models are significantly larger, probably because of the galdiff used.

In the instance of the residual maps that are presented in Figure 3.8, we are once again able to validate the progress that has been made in the quality of the model that has been developed. When we analyze places further away from the galactic plane and the center of

the galaxy, we notice that the residue map does not display extremely emphasized regions. This is especially true in the case of the plot on the right. However, in both situations, and similarly to the scenario that was covered in the section before this one, the galactic plane is the location that presents the greatest challenges in terms of adequate fitting. Combining this information with the higher significance values that were observed in the previous histogram reveals that, it is now much more challenging than before to look at the galactic plane region in the correct manner. This is yet another indication that the galdiff played a role in the development of the model.

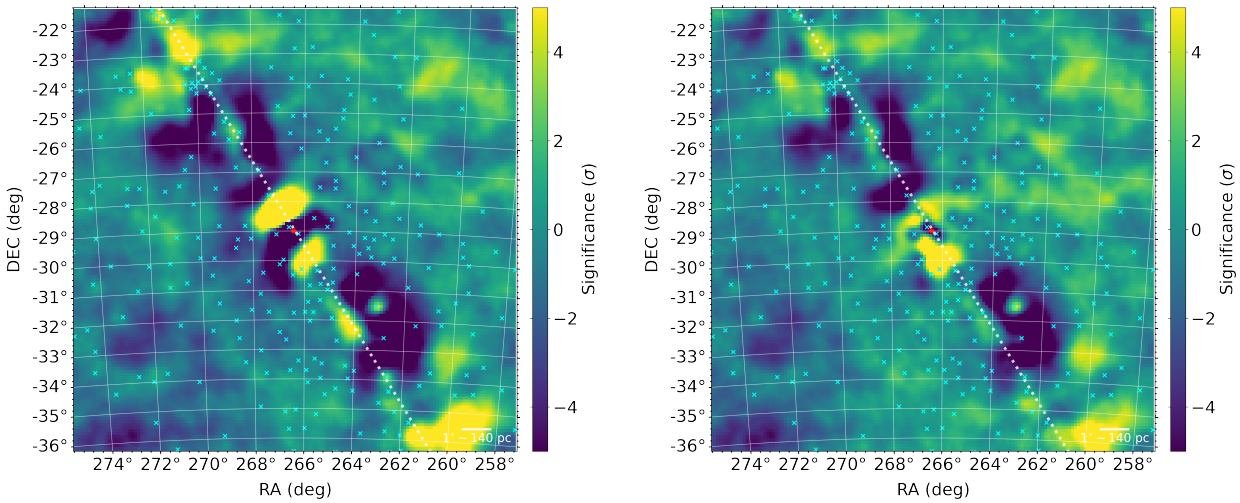

Figure 3.8: Map of residuals, corresponding to the first and the fit number 455 of the model used to build the SED using an old galdiff model. On the left, there is a greater concentration of areas that need improvement in the model, indicating regions of under- and over-prediction, mainly in the central region. On the right, there is a smaller concentration of them, with the exception of the galactic plane region, whose problems are related to the nature of the region and the use of the old galdiff model.

The comparison between the residual map of the initial fit and the one of the latest fit reveals that there has been a reduction in the number of significant excesses found in the galactic plane. This finding is significant from a practical standpoint. In essence, they have not been completely resolved, but the performed fittings were able to address all of their issues in a complete way, meaning that none of these regions were not adequately treated. Therefore, when we combine the information that is present in the fit 455 residual map with the changes that were observed in the histograms that were discussed earlier and in the TS map that will be seen below, the decision to cease creating the model at this

point becomes understandable.

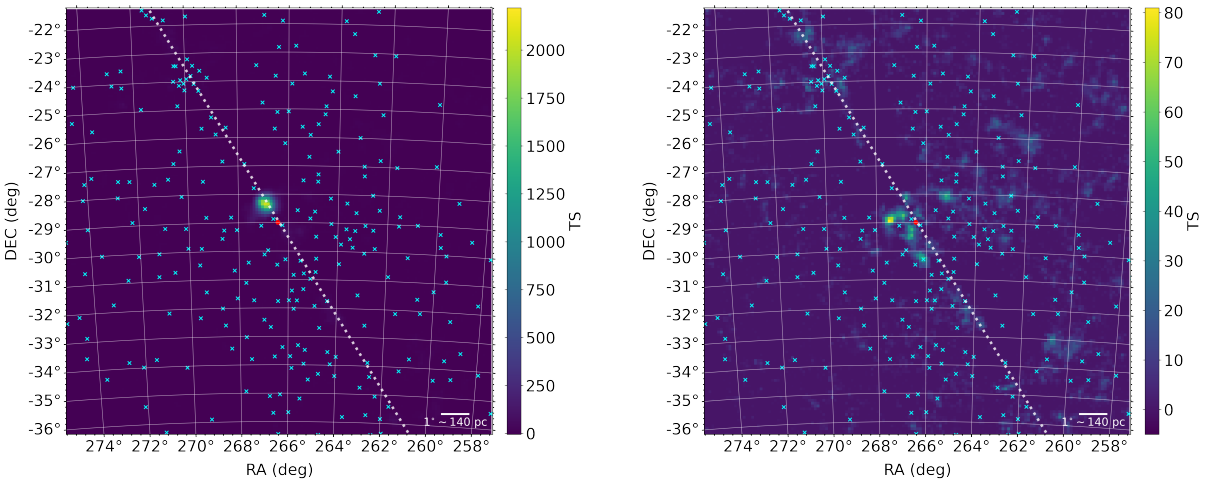

Figure 3.9: TS maps, used as fit quality assessment tools, corresponding to the first and last fit of model used to build the SED using the old model of the galdiff. On the left, it is possible to see a region highlighted from the others due to a high TS value. On the right, in turn, it is possible to see a differentiated panorama, showing that the fits carried out treated the ROI properly. This indicates a good improvement in the model used.

Two observations on the TS maps present at Figure 3.9 may be made. Following the initial fitting, the model displayed a value for this indication, as shown on the left plot, that was outside its the typical range when we compare it with the ones from the previous case. This as a result, showed that there was a place in the region adjacent to SOI in which the chance of the presence of a source at that moment was extremely high. As the SOI itself was already incorporated into the model, it was not possible for such a point to ever refer to it. This, together with the TS values that were on the map, suggested that there was a need for improvements to be made to the fitting of the central region and the area near to the SOI. In an essence, this is a TS map that unequivocally demonstrates that the model that was established at that point in time was inadequate.

However, with the use of the algorithm discussed in the previous chapter, it was rectified, perfected, and improved, which in the end led to us having the TS map that was shown by the right plot. This plot illustrates a scenario in which the difference between the various TS values in the ROI is smaller, with fewer foci of places where the TS is large.These foci, however, continued to exist even after the full model creation algorithm had been applied, as well as after attempts had been made to individually treat and fit

each of these locations. Therefore, when viewed in a broader context and when the information presented here is combined with that presented by the other diagnostic plots, it is clear that the model has, in fact, been improved. Furthermore, considering that significant improvements were no longer observed in valid fits, the decision to stop developing the model at this point was an appropriate one. In such manner, we were ready to build the SED.

3.2.1.2 *The SED built*

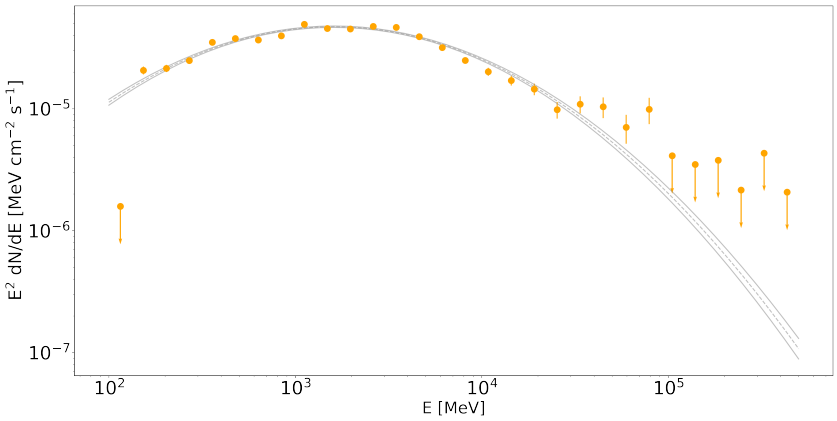

Figure 3.10: The SED build with an older version of the galdiff. Built with photons of energy between 100MeV and 500GeV, and from observations between August 2008 and July 2022 and with the selection of parameters described in table 3.2. The data is described by a log-parabola with parameters $\alpha = 2.49 \pm 0.02$, $\beta = 0.185 \pm 0.006$, $N_0 = (9.0 \pm 0.2) \times 10^{-13}$ cm^{-2} s^{-1} MeV^{-1}, and $E_0 = 6113$ MeV. In grey, there is the best fitting curve from the model data accompanied by 1σ errors.

Figure 3.10, contains the SED constructed with the use of this model. Figure 3.11 contains a plot that compares the SED constructed with the model described above, which is shown in orange, to the fiducial SED, which is shown in red. The gray line depicts the log-parabola spectral model that is provided by the model that was explained in this subsection and is constrained by the associated 1σ uncertainty.

The parameters that best describe the log-parabola data set seen in the Figure 3.10, from the construction of the SED are $\alpha = 2.49 \pm 0.02$, $\beta = 0.185 \pm 0.006$, $N_0 = (9.0 \pm 0.2) \times 10^{-13}$ cm^{-2} s^{-1} MeV^{-1}, and $E_0 = 6113$ MeV. The E_0 parameter has no error because it was kept fixed throughout the process.

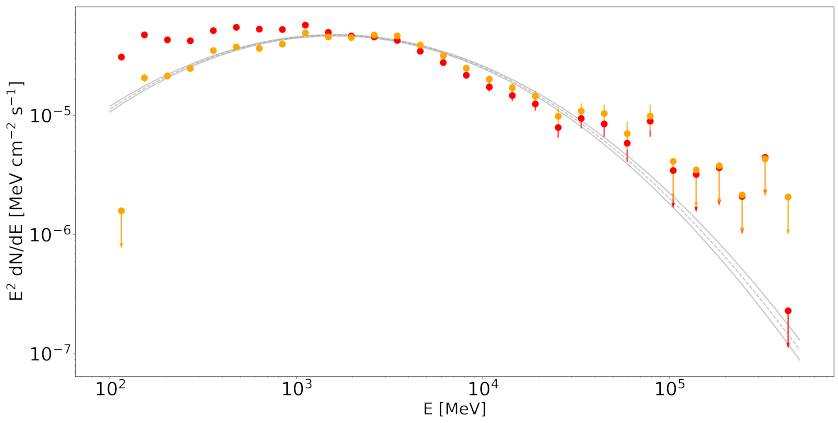

Figure 3.11: The SED build with an older version of the galdiff in orange and the fiducial SED, in red. Comparing them, it is possible to see that there is a difference between them. In grey, there is the best fitting curve from using parameters from model that used the old version of galdiff accompanied by 1σ errors

It is particularly interesting to note here that, as Figure 3.11 demonstrate, the selection of a different model for galdiff does, in fact, alter the SED that is obtained. Although this influence is present throughout the entire energy band that was investigated, it is far more significant in the region of lower energies. This is a reflection of the fact that, as was aptly explained previously, the majority of the galdiff's emissions are also in this energy range. As a result, these alterations are connected to the decreased quality of the galdiff that was utilized. In turn, this also has an affect in the scenario of greater energies since, as we have shown, the ROI fitting in here was more arduous to do than it was in the scenario where the fiducial SED was involved.

Considering that the format of this SED conveys very distinctive information about the SOI as well as the physical processes that are taking place nearby, because hadronic emissions are characterized by the presence of a bump in the region of lower energies, for example, we need to carefully understand the changes that have been found so we can latter interpret it correctly.

Below, we will continue with the description of the construction, evaluation of the quality of the fitting, and building of a new SED utilizing an even older version of galdiff than the one that was utilized here.

Model parameters	
Energy range:	100MeV-500GeV
Date interval:	Aug/2008 - July/2022
Catalog:	4FGL-DR3
Photons PSF:	0+1+2+3
Galdiff:	gll_iem_v05
Isodiff:	iso_P8R3_SOURCE_V3_v1

Table 3.3 - Set of model configuration and selection parameters used in the creation of the SED using the older galdiff model

3.2.2 SED using an even older galdiff model

The first step of this procedure is to construct a model for the ROI. The decisions regarding the choices of things to be used, are the same as the ones that were made in the preceding scenario, with the exception of the version of galdiff that was utilized. In this particular instance, we made use of the gll_iem_v05, which is the oldest version of the galdiff that is still compatible with our analysis.An overview of the parameters that were used throughout the building of this model may be found in table 3.3. From a practical point of view, the best model we were able to obtain for the central region of the galaxy within our ROI, using the configurations described above was obtained after running a total of 446 valid fits.

It is noteworthy that the version of galdiff that was used here is, in essence, a slightly different version than the one that was discussed in the previous subsection. Their similarity is due to the fact that the version from the subsection above is actually a slightly revised version of the templates that are utilized in the version that is being employed here. Nevertheless we will conduct just as thorough an investigation of them. It is also important to point out that other versions of galdiff do exist, some of which are rather old; unfortunately, these other versions of galdiff are not fully compatible with the photons that we selected, notably the catalog that we employed. Because of this, no attempt was made to explore them.

3.2.2.1 About the fit quality

The histograms depicting the significance values for the ROI in its entirety may be found in Figure 3.12. On the left is the histogram that we acquired after the very first fit, and on the right is the histogram that we obtained after the final fit.

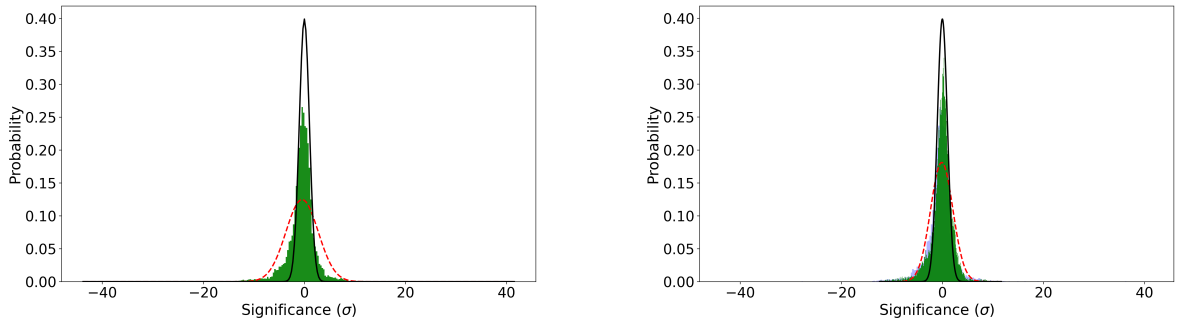

Figure 3.12: Residue histograms used as fit quality assessment tool, for the whole ROI. On the left, we have the histogram corresponding to the first fit executed in the construction of the model for the SED that uses the oldest galdiff. The red curve is characterized by having a mean $\mu = -0.4$ and standard deviation $\nu = 3.2$. On the right, we have the histogram corresponding to the last fit executed in the construction of the model. Here the red curve has a mean $\mu = -0.1$ and a standard deviation $\sigma = 2.2$. The data set in blue in this histogram is the same as the one on the left plot, placed there to facilitate comparisons. In both cases the black curve is the ideal normal distribution, with mean $\mu = 0$ a standard deviation $\sigma = 1$.

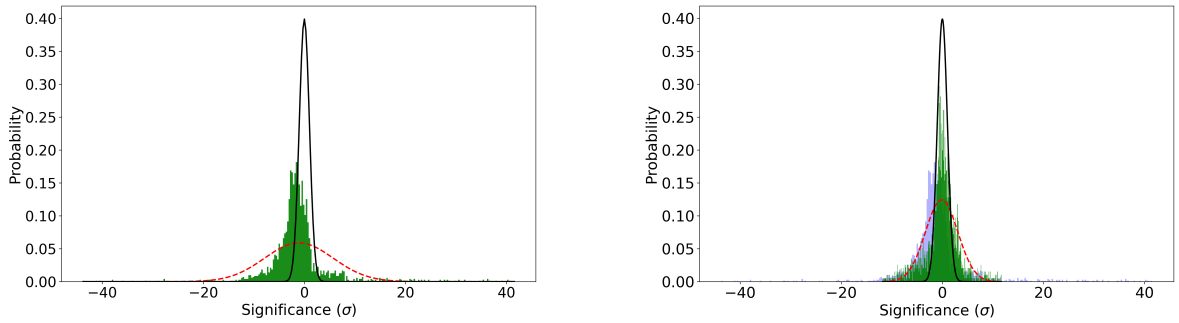

Figure 3.13: Residue histograms used as fit quality assessment tool, for a square region of the ROI . On the left, we have the histogram corresponding to the first fit executed in the construction of the model for the SED that uses the oldest galdiff. The red curve is characterized by having a mean $\mu = -1.1$ and a standard deviation $\sigma = 6.8$. On the right, we have the histogram corresponding to the last fit executed in the construction of the model for the same region. Here the red curve has a mean $\mu = -0.1$ and a standard deviation $\sigma = 3.2$. The data set in blue in this histogram is the same as the one on the left plot, placed there to facilitate comparisons. In both cases the black curve is the ideal normal distribution, with mean $\mu = 0$ a standard deviation $\sigma = 1$.

In terms of the normal curve that most accurately describes the data, the information on the left side leads us to a curve with mean $\mu = -0.4$ and standard deviation $\nu = 3.2$, while the information on the plot at right side leads us to a normal curve that has a mean of $\mu = -0.1$ and a standard deviation $\sigma = 2.2$. When seen from a more broad perspective, it is feasible to observe that the model building method that was applied to ROI was successful

in bringing it closer to the ideal scenario.This becomes even more apparent when we look at the data from the most central region of the ROI, which comes from a square region centered on the SOI and with sides measuring 5 degrees, as shown in Figure 3.13. In this case, the change in model quality in the region is even more noticeable because, initially, there was a large concentration of negative significance there, not to mention also a large variation in the significance values, as indicated by the plot on the left. On the other hand, as can be seen in the plot on the right, after the fitting and modeling procedure was completed, the region became closer to what would actually be expected from a good model. In mathematical parlance, the normal curve on the left plot that best describes the data has a mean $\mu = -1.1$ and a standard deviation $\sigma = 6.8$, whereas the one on the right plot has a mean $\mu = -0.1$ and a standard deviation $\sigma = 3.2$.

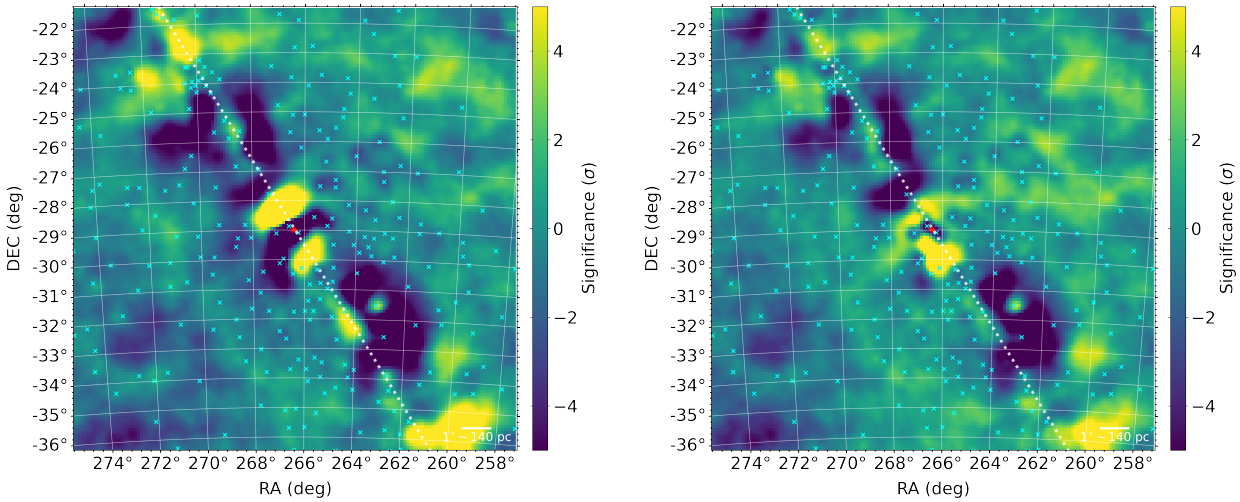

Figure 3.14: Map of residuals, used as fit quality assessment tools, corresponding to the first and last fit of the model that uses the oldest galdiff avalable. On the left, there is a greater concentration of areas that need improvement in the model, indicating regions of under- and over-prediction. This can be seen all along the galactic plane. On the right, there is a smaller concentration of them, with the exception of the galactic plane region, whose problems are related to the nature of the region and the galdiff model we have.

The residual map that we had for the ROI after the initial fit is shown on the left side of Figure 3.14, and the final residue map is shown on the right side of the same Figure. In the same way as in the preceding case, the region of the galactic plane contains a significant number of locations that require attention. For instance, on the map on the left, one can

even see places adjacent to SOI need to be adequately handled in order to get a better model. If now we concentrate on the data presented by the map on the right, we can see that the situation is better. Despite the fact that there are still regions near to the maximum and minimum values of significance in there, such regions now cover a smaller area than they did previously, which is a direct result of the successful fitting process that was carried out. Furthermore, in regions far from the the galactic plane, there are no particularly concentrated locations on the maps. This suggests that, the model created provides sufficient and adequate coverage for these locations.

In addition, despite the fact that the regions of the residual map on the right hinted at locations whose fit may be improved, attempts were made to do so. Nevertheless, these attempts were fruitless because there were no major improvements seen in valid fits as a result of them. This information, in conjunction with the results and data obtained from the diagnostic plots, gave the impression that it was indeed time to finish the model after fit 446.

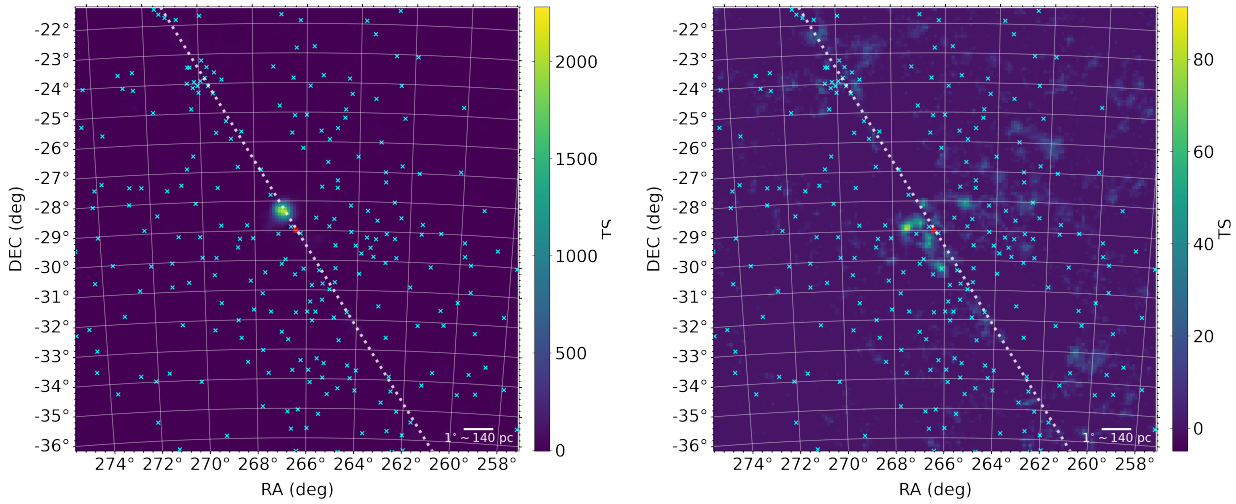

Figure 3.15: TS maps for the first and last fit of the model used to make the SED that uses the older galdiff. On the left, it is possible to see a single highlighted region next to SOI, indicating that the model needs improvement. On the right, a more homogeneous distribution of regions with detected TS is seen, with lower absolute values, indicating a general improvement.

The scenario that is shown by the TS maps for the two highlighted fittings that are shown in Figure 3.15 reveals a scenario that is quite comparable to the situation that was shown in Figure 3.9.

Once more, the TS map that was obtained after the initial fit displays a region that is particularly emphasized, suggesting the pressing requirement for enhancements to be made to the model. In the end, the TS map on the right was found, which essentially demonstrates that as the fittings were being made, the model was being improved and arriving at a more heterogeneous situation. In addition, when looking specifically at the final TS map, we discovered that it did not contain any TS foci that represented areas of the map that require enhancement as is the case when looking at regions that were further away from the plane of the galaxy. Close to the SOI, there is the presence of some of them, however, this region was exhaustively treated, and the result seen is the best that was possible to obtain.This result once again suggests that we got a great model improvement and that we examined all possibilities for substantial improvements that we could have made.

3.2.2.2 The SED built

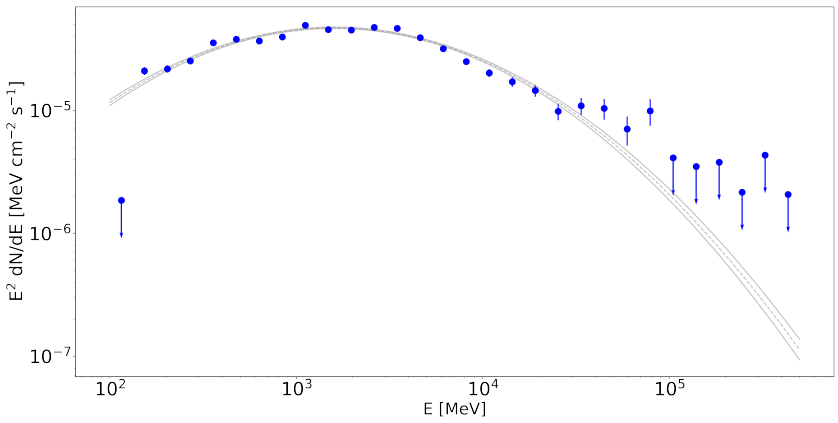

Figure 3.16: The SED build with the oldest version of the galdiff. Built with photons of energy between 100MeV and 500GeV, and from observations between August 2008 and July 2022 and with the selection of parameters described in table 3.3. The data is described by a log-parabola with parameters $\alpha = 2.49 \pm 0.02$, $\beta = 0.185 \pm 0.007$, $N_0 = (9.1 \pm 0.2) \times 10^{-13}$ cm^{-2} s^{-1} MeV^{-1}, and $E_0 = 6113$ MeV. In grey, there is the best fitting curve from the model data accompanied by 1σ errors.

The SED that was constructed here can be found on Figure 3.16. Figure 3.17, in turn, is a plot that shows all of the SEDs that have been constructed up to this point, making it feasible to evaluate each one against the others. In both cases, the gray line represents the log-parabola spectral model for the SOI that was provided by the model. This log-parabola

is constrained on either end by two curves that indicate the corresponding 1σ errors.

In particular with regard to the present on Figure 3.16, the parameters that provide the most accurate description of the spectral model of the log-parabola that was produced from the SED built are as follows $\alpha = 2.49 \pm 0.02$, $\beta = 0.185 \pm 0.007$, $N_0 = (9.1 \pm 0.2) \times 10^{-13}$ cm^{-2} s^{-1} MeV^{-1}, and $E_0 = 6113$ MeV. Once more, the E_0 parameter was kept fixed throughout the process and has no error because of it.

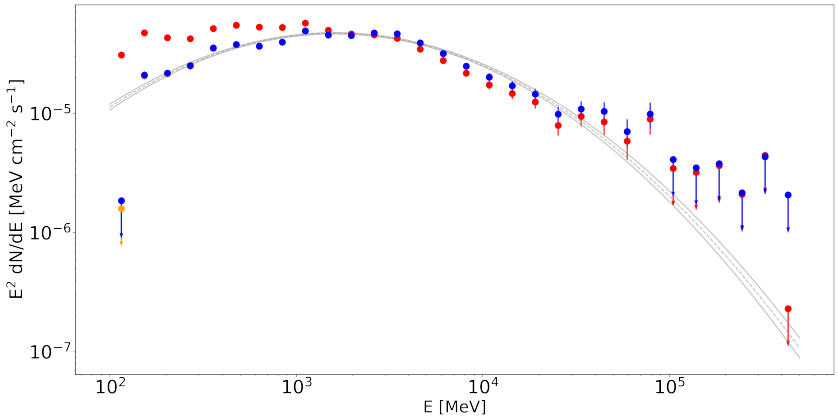

Figure 3.17: The SED build with the oldest version of the galdiff in blue, the SED built with an older version of the galdiff in orange and the fiducial SED, in red. Comparing them, is possible to see that there is a difference and a little scattering among them. In grey, there is the best fitting curve using parameters from model that used the oldest version of galdiff, accompanied by 1σ errors

There are three SEDs located on Figure 3.17. In blue we have the one that was built here, in red we have the fiducial SED, and in orange we have the SED that was created in the subsection that came before this one. When we look at them side by side, we can see that the SED that was built more recently is different from the fiducial one, but that it is relatively comparable to the one that was described in the subsection above. This demonstrates that selecting this galdiff actually takes us to a different SED. However, because the version that is being used here is quite comparable to the galdiff used before, as was mentioned at the beginning of this subsection, it is in fact to be expected that, after constructing a model based on the same algorithm, they will be quite comparable to one another, as is the case. This correspondence also demonstrates that the two models worked on in this part, which are independent from one another, both had a well done fit, reaching at the end in a very near panorama, and having as a maximum consequence the significant similarity between the SEDs.

3.3 Systematic error analysis

When we peered at the SEDs previously found, we noticed that depending on which version of galdiff we used, we would get different results. Straightforwardly, this means that the galdiff model introduces a source of systematic errors in our analysis and this needs to be taken into account for any modeling we want to do. From this point of view, we had already investigated all that was available to investigate, and at this point, we may attempt to carry out a process of merging the SEDs. However, before moving on to the aforementioned combination, it is necessary to investigate and address other potential sources of systematic error that may exist. Throughout the course of this procedure, came to the realization that a significant contributor to this kind of inaccuracy is the influence of sources whose parameters were freed during the stage of building the SED.

When constructing the SED, one has the option of either releasing the parameters associated with a single source or the parameters associated with a certain collection of sources. Until this point, the SEDs have been constructed by just making SOI parameters available for fitting. In this case, the maximum likelihood procedure will be carried out, and it will examine all of the pertinent data in order to compute the flux in each of the energy bins that are being taken into consideration. Because of this operation, once the SED has been constructed, we may find that the values of the spectral parameters that we have are different from those that were initially provided by the model, something that is natural from this perspective, and that allows us to obtain a better description of the source's emission than if we used the information coming from the model directly.

Going a step further, there is a scenario in which the procedure described above can take place in such a way that the final SED no longer depends only on the influence of a single source, but that now the flux computed in each energy bin, as well as SOI's global SED, also depend on adjustments that take place in the parameters of each of the freed sources individually. In a nutshell, what this basically means is the fact that the process of creating the SOI SED using different sources with released parameters, implies that the SOI we get can be different depending on this set of released sources, given that the maximum likelihood process will look at a larger set of information for adjustment. If we know these sources well, the results may not differ so much from those already found. However, in a region like the GC, this can be problematic precisely because of the location

	Closest sources				
1	4FGL J1744.9-2905	4FGL J1746.4-2852	4FGL J1748.3-2906	4FGL J1742.5-2833	4FGL J1747.2-2957
2	4FGL J1744.9-2905	4FGL J1746.4-2852	4FGL J1748.3-2906	4FGL J1742.5-2833	4FGL J1740.4-2850
3	4FGL J1744.9-2905	4FGL J1746.4-2852	4FGL J1748.3-2906	4FGL J1747.2-2957	4FGL J1740.4-2850
4	4FGL J1744.9-2905	4FGL J1746.4-2852	4FGL J1742.5-2833	4FGL J1747.2-2957	4FGL J1740.4-2850
5	4FGL J1744.9-2905	4FGL J1748.3-2906	4FGL J1742.5-2833	4FGL J1747.2-2957	4FGL J1740.4-2850
6	4FGL J1746.4-2852	4FGL J1748.3-2906	4FGL J1742.5-2833	4FGL J1747.2-2957	4FGL J1740.4-2850

Table 3.4 - Set of sources closest to SOI that had parameters released for the investigation of systematic errors.

	Brightest sources				
7	4FGL J1747.2-2957	4FGL J1801.3-2326e	4FGL J1801.6-2326	4FGL J1809.8-2332	isodiff
8	4FGL J1747.2-2957	4FGL J1801.3-2326e	4FGL J1801.6-2326	4FGL J1809.8-2332	galdiff
9	4FGL J1747.2-2957	4FGL J1801.3-2326e	4FGL J1801.6-2326	isodiff	galdiff
10	4FGL J1747.2-2957	4FGL J1801.3-2326e	4FGL J1809.8-2332	isodiff	galdiff
11	4FGL J1747.2-2957	4FGL J1801.6-2326	4FGL J1809.8-2332	isodiff	galdiff
12	4FGL J1801.3-2326e	4FGL J1801.6-2326	4FGL J1809.8-2332	isodiff	galdiff

Table 3.5 - Set of brightest sources of the ROI that had parameters released for the investigation of systematic errors.

and number of sources present there.

Nevertheless, in a region such as ours, where the number of gamma sources is rather high, it is recommended that an investigation similar to the one that was described above be carried out. This is further supported by the fact that even having access to the most advanced modeling techniques, we are unable to accurately identify all of the sources in the region.Because of this, we anticipate that the final total error σ^2_{tot} of this study will be given by the following formula:

$$\sigma^2_{tot} = \sigma^2_{stat} + \sigma^2_{sis} \tag{3.1}$$

where σ^2_{stat} is for the statistical errors that were given by the analysis itself, and σ^2_{sis} stands for the systematic error that is caused by the dispersion of the points in the different SEDs.

	Biggest TS sources				
13	4FGL J1747.2-2957	4FGL J1732.5-3131	4FGL J1748.0-2446	4FGL J1801.3-2326e	4FGL J1809.8-2332
14	4FGL J1747.2-2957	4FGL J1732.5-3131	4FGL J1748.0-2446	4FGL J1801.3-2326e	galdiff
15	4FGL J1747.2-2957	4FGL J1732.5-3131	4FGL J1748.0-2446	4FGL J1809.8-2332	galdiff
16	4FGL J1747.2-2957	4FGL J1732.5-3131	4FGL J1801.3-2326e	4FGL J1809.8-2332	galdiff
17	4FGL J1747.2-2957	4FGL J1748.0-2446	4FGL J1801.3-2326e	4FGL J1809.8-2332	galdiff
18	4FGL J1732.5-3131	4FGL J1748.0-2446	4FGL J1801.3-2326e	4FGL J1809.8-2332	galdiff

Table 3.6 - Set of sources with highest TS from the ROI that had parameters releases for the investigation of systematic errors.

3.3.1 Exploring even more SEDs

When seen from the perspective presented earlier, the next step is to construct many SEDs, freeing a variety of sources and parameters. From this, we can evaluate the impact those new freed sources have on the SED format, and after that, merge those new SEDs with the SEDs that were built above to get another one - the final SED. In order to accomplish this, we decided to make use of the same model that was responsible for the production of the fiducial SED. This is due to the fact that this model provides us with the optimal scenario for the ROI. Among other things, it was developed using the most recent versions of the isodiff and galdiff models that were developed. As a natural outcome of this, the discussion regarding its quality and the fitting that was conducted has already been made and reviewed.

After that, the following step would be to select the manner in which we would release the sources for analysis, as well as the specific source sets that we would make available. This is a relatively complex operation because, in an ideal scenario, this would need to be accomplished by releasing an additional source in addition to the SOI, changing that additional source, and creating the SEDs. Then, we would release two additional sources, change them in some way, and compute the SED for each iteration, and so on. It is impossible for such a method to be appropriate since it would lead to an excessive amount of systematic error, it would demand time and computer resources that we do not have available, and it would consequently result in a prohibitive analysis.

Because of this, the solution that we decided to adopt was to restrict ourselves to the six sources that had the highest TS, the six sources that had the highest brightness, and the six sources that were located closest to the SOI. This allowed us to release the parameters of the SOI and five other sources at a time in each SED that we built. This decision resulted in a scenario in which there were a total of 18 additional SEDs created. The various combinations of sources that were employed in the production of each new SED in this scenario are listed in tables 3.4, 3.5, and 3.6, respectively. Table 3.7 contains, on the other hand, information regarding the parameters of the spectral model that most accurately describes each of them.

SED	α	β	N_0 (cm^{-2} s^{-1} MeV^{-1})
1	(2.57 ± 0.02)	(0.133 ± 0.006)	(8.0 ± 0.2)×10^{13}
2	(2.57 ± 0.02)	(0.133 ± 0.006)	(8.0 ± 0.2)×10^{13}
3	(2.57 ± 0.02)	(0.133 ± 0.006)	(8.0 ± 0.2)×10^{13}
4	(2.57 ± 0.02)	(0.133 ± 0.006)	(8.0 ± 0.2)×10^{13}
5	(2.57 ± 0.02)	(0.133 ± 0.005)	(8.0 ± 0.2)×10^{13}
6	(2.57 ± 0.02)	(0.133 ± 0.005)	(8.0 ± 0.2)×10^{13}
7	(2.57 ± 0.02)	(0.134 ± 0.005)	(8.0 ± 0.1)×10^{13}
8	(2.57 ± 0.02)	(0.134 ± 0.005)	(8.0 ± 0.1)×10^{13}
9	(2.57 ± 0.02)	(0.134 ± 0.005)	(8.0 ± 0.1)×10^{13}
10	(2.57 ± 0.02)	(0.134 ± 0.005)	(8.0 ± 0.1)×10^{13}
11	(2.57 ± 0.02)	(0.134 ± 0.005)	(8.0 ± 0.1)×10^{13}
12	(2.57 ± 0.02)	(0.133 ± 0.005)	(8.0 ± 0.1)×10^{13}
13	(2.57 ± 0.02)	(0.133 ± 0.005)	(8.0 ± 0.1)×10^{13}
14	(2.57 ± 0.02)	(0.134 ± 0.005)	(8.0 ± 0.1)×10^{13}
15	(2.57 ± 0.06)	(0.13 ± 0.01)	(8.0 ± 0.5)×10^{13}
16	(2.57 ± 0.02)	(0.134 ± 0.005)	(8.0 ± 0.1)×10^{13}
17	(2.57 ± 0.02)	(0.134 ± 0.005)	(8.0 ± 0.1)×10^{13}
18	(2.57 ± 0.02)	(0.133 ± 0.005)	(8.0 ± 0.1)×10^{13}

Table 3.7 - Set of parameters of the log-parabolas that best describe the SEDs present in Figure 3.18, created from the release of the SOI and the sources present in the tables 3.4-3.6. In all cases, E_0 = 6113 MeV.

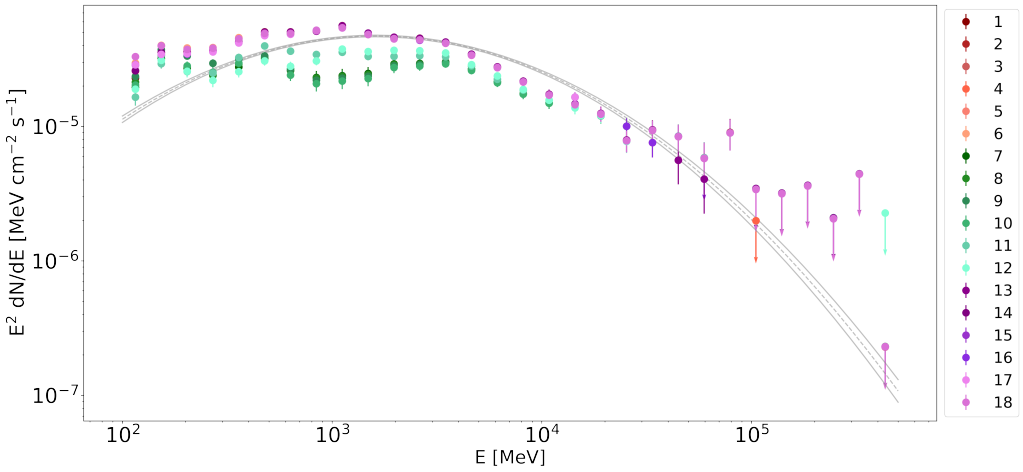

Figure 3.18: Set of SEDs generated with more than one source with free parameter, following the information in the tables 3.4-3.6. It is clearly seen that there is considerable dispersion in this scenario, which corroborates the hypothesis that this contributes to a systematic error. In grey, there is the best fitting curve from the Fiducial model accompanied by 1σ errors.

In turn, in Figure 3.18, these SEDs are all plotted together, so that it is possible to see them in relation to each other. In this context, it is essential to take into account the fact that the SEDs in this plot can be broken down into three major categories, each of which is represented by a distinct color and associated with the nearest, brightest, and highest

TS sources. The numbers that are displayed in the image provide a direct reference to the various combinations of sources from which they were derived, as can be found in the tables 3.4-3.6. The plot reveals that there is, in fact, considerable dispersion at several points, indicating that the analysis actually needed to be done. The spectral description and the 1σ error from the model that was employed are represented in this image by the dotted gray line, and the two gray curves, respectively.

3.3.2 *The final SED*

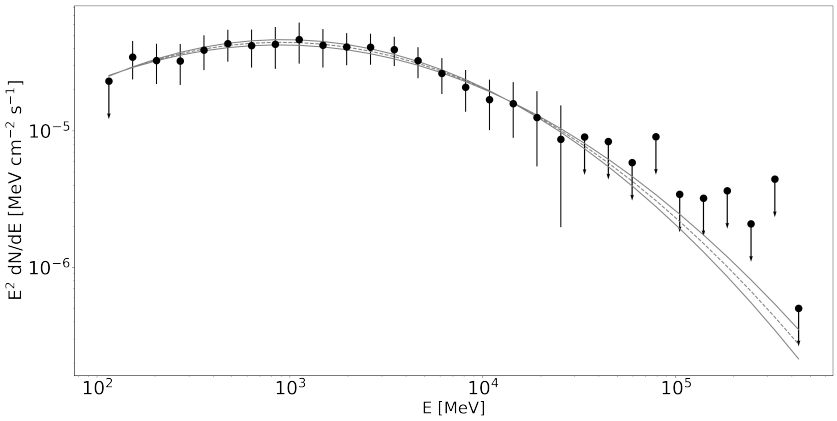

Figure 3.19: The final SED, built from the combination of all the other. It also uses photons of energy between 100MeV and 500GeV, and from observations between August 2008 and July 2022. The data is described by a log-parabola with parameters $\alpha = 2.51 \pm 0.03$, $\beta = 0.134 \pm 0.009$, $N_0 = (7.3 \pm 0.2) \times 10^{-13}$ cm^{-2} s^{-1} MeV^{-1}, and $E_0 = 6113$ MeV. The grey curve is the function given by the above parameter, while the dotted curve is related to the 1σ errors of it.

After all of that, the final objective is to combine the data that comes from the many SEDs that we constructed, including both: the ones shown directly above as well as those covered in the two sections that came before this one. This is of the utmost significance because the SED constructed in this manner will be able to contain all of the information about systematic errors that we construct and will be in a position to present a reliable image of the SOI emission. The SED that will be shown below is, without a doubt, the one considered the culmination of this investigation and will be utilized going forward.

However and, before presenting the SED itself, it is necessary to have a solid understanding of the process that was used to create it. The errors that are displayed in it are the total errors, σ_{tot}, and are consequently the ones that are given by the expression 3.1.

The formula was used as to guide through the process of locating them, making sure to give special attention to the fact that the values for the systematic error are derived from the dispersion that is presented in each of the SED points. In turn, the value of each of the flow points of this final SED is given by the arithmetic mean of the values of the respective points in the original SEDs. In this one result, available in Figure 3.19, we have information provided from a total of 21 different SEDs.

In particular, this SED is naturally described by a log-parabola spectral model, whose parameters, found via the application of a least squares algorithm, are given by: $\alpha = 2.51 \pm 0.03$, $\beta = 0.134 \pm 0.009$, $N_0 = (7.3 \pm 0.2) \times 10^{-13}$ cm^{-2} s^{-1} MeV^{-1}. As in the previous cases, the value of $E_0 = 6113$ MeV was kept fixed. An essential distinction between this version of the SED and the others is that, in this case, the gray dotted line relates to a log-parabola spectral model detailed by the parameters listed above, and not by one from a initial model. The dotted curve is related to the 1σ errors, which are referred to by the other two curves.

Chapter 4

Model

4.1 *Preliminary comparison to known models*

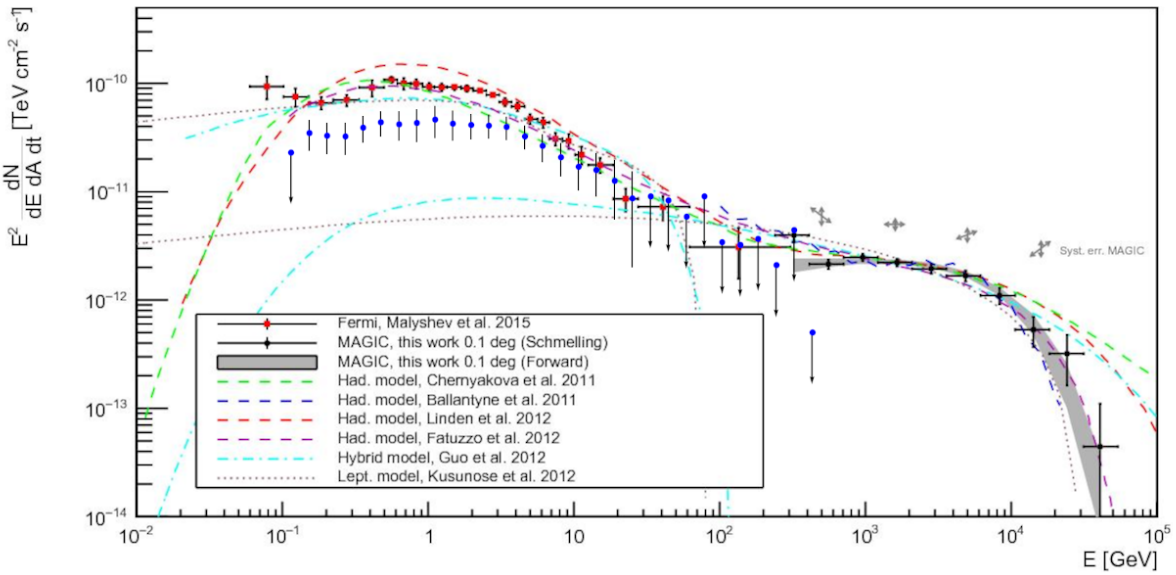

Figure 4.1: The 4FGL J1745.62859 SED built, from 100MeV to 500GeV and its comparison to a number of different models for Sgr A* high energy emission. Adapted from Ahnen et al. (2017).

The literature has looked into a variety of studies and models about Sagittarius A* gamma emissions starting from MeVs and arriving at TeVs. Figure 4.3 displays the primary examples that fall under this category and uses *Fermi*-LAT data. In an effort to understand our result, we have also incorporated the findings from our investigation into this figure so that it can serve as an initial point of comparison to models that were previously used to describe our SOI.

The models that are compatible with the energy band observed by *Fermi* make up the majority of the models on the list, with the exception of Ballantyne et al. (2011). This

model, in particular, is focused on TeV emissions, but shares an overlap with our data in the lowest energy range. In the next part, we will discuss some of the primary models that are displayed in this picture (and some others that are important).

The models that describe Sgr A* emissions in our energy band can be basically classified into two distinct varieties: those that are said to be leptonic and those that are considered to be hadronic. In a sentence, the primary distinction between them lies in the nature of the particle that is responsible for the generation of gamma radiation. It stands to reason that leptons are responsible for their generation in leptonic models, whereas hadrons are responsible for their generation in hadronic models. In a different way, there are also hybrid models, as we will see.

Let's begin by having a quick explanation about the model of Kusunose and Takahara (2012), a model that will be investigated in greater depth in the following part. Their investigation was based on 25 months' worth of GC emissions that were collected by the *Fermi*-LAT; these are the very same emissions that were utilized initially by Chernyakova et al. (2010). The essence of this approach can be summed up in two things: i) electrons that flee and travel away from the region that is regarded to be in the neighborhood of Sgr A*, but that is accumulate in a region whose size is of the order of 10^{18} cm, and ii) in the soft photons that are emitted by stars and dust that are in the region around the GC. This is the case due to the fact that the primary concept behind the model is that the gamma emissions result from the IC scattering of electrons that have escaped from the vicinity of Sgr A* with the soft photons that were discussed before. When we basically consider emissions between 10GeV and 100GeV, our findings are consistent with this model, as shown in Figure 4.3. This is the case when we consider this range of energies and none other.

The discrepancy for this, as we imagine to be the case for the discrepancy in relation to the other models that will be discussed, must be associated with the amount of data we had available for our analysis, an improvement in the models of diffuse emission from the galaxy, since, with better models we can, for example, expect less contamination, and particularly from our extensive systematic error handling, something that hasn't been particularly explored before in the way that we've done here.

The Malyshev et al. (2015) model is yet another elementary leptonic model for GC emissions. It makes use of data spanning around 6.2 years. In it, the authors explore the

idea of a combination of emissions from electrons that would be injected into the vicinity of Sgr A* during a powerful flare from it, which would have occurred somewhere between 100 and 400 years ago, and with much weaker activity today. They take into consideration ionization processes, bremsstrahlung, IC, and synchrotron emissions as potential pathways for the loss of energy. The flux value between 1 and 10 GeV is expected to diminish by approximately 10% according to one of the predictions made by this model at time scales that are longer than those analyzed by them. When compared to what they said, our data would only be a decrease in the flux seen in their original model in this range if the prediction had pointed out a decreace higher than 10%; this demonstrates yet another incompatibility with their model, given that we can see that in the region smaller than 1GeV, there is no compatibility between them.

Chernyakova et al. (2010) work, on the other hand, investigates a hadronic model. It makes use of observations collected by *Fermi*-LAT and H.E.S.S. over the course of 25 months. The most important point being made here is that relativistic protons that have been accelerated by Sgr A* would interact with gas in the most central region of the galaxy at only a few parsecs, and would generate, as a result of this interaction, products that would originate gamma emissions. Only in the maximum energy scenario, particularly still in the 10-100 GeV region, do our data support this model along with the other hadronics, as is shown in Figure 4.3. The presence of a bump in the region with the lowest energy is something that is typical of this type of model. This bump is caused by the decay of pions as discussed in the Introduction, but is something that is not clearly observed in our data, although it may be present to a lesser degree there, as we will discuss in detail latter.

Because Linden et al. (2012) constructed a hadronic model that is very comparable to the one that was described above, we won't go into further detail about it right now. Fatuzzo and Melia (2012), on the other hand, uses an alternative model. Within it, the environment around Sgr A* is composed of two phases. The first one would be an environment that is more interior and has a higher density, with a morphology closer to a torus there. The second component would be the exterior surrounding environment, which is referred to as the wind-zone. In this part of the discussed area, we would find the interstellar environment loaded with shocked stellar winds. In this scenario, gamma rays with energies comparable to those detected by *Fermi* would originate from the torus, whereas gamma rays with energies higher than those detected by *Fermi* would originate from the

other environment. However, as discussed earlier, our data do not seem to fit any of these models adequately and other than in one region or another when considering the error bars present.

Closing, the work of Guo et al. (2013) is responsible for the introduction of the differentiated model into our discussion. This model is a hybrid and it uses emissions from both hadronic and leptonic particles. In this proposal, protons and electrons would be accelerated in the GC, most likely in locations that are nearby to Sgr A* . The protons' interactions with the interstellar medium would result in gamma emissions on the scale of TeV, while the electrons' IC scattering of soft photons would be the source of the other emissions. It is clear from looking at Figure 4.3 that the results reported by this model do not match up with our data, which results in the curve that characterizes the model having flow rates that are higher than those that we measured.

But, in general, it is important to note that the fact that our data are not totally in accordance with any of the models that have been provided in the past does not necessarily signify a negative outcome. This is due to the fact that our SED was constructed using more data than those that were available and analyzed in any of the presented models, that it had models of diffuse galactic and isotropic extragalactic emissions available that were more up to date than those that were used in any previous analysis, and that it implemented systematic error handling distinct from what has been accomplished until now. In light of this, below we will discuss two models that have been appropriately applied to our data: one of leptonic origin and the other of hadronic origin, so that we can in fact have a better understanding of this EDS and extract, from it, new information about the environment of the center of the galactic.

4.2 A basic overwiew

Leptons are particles that do not interact through the mechanism of strong interaction.When we examine this category only via the lens of charged particles, the electron serves as the most prominent example of this class. Emissions connected with these particles typically take place when they are in a setting that is characterized by the presence of magnetic fields. The acceleration of these particles, which results in the production of photons through a process known as synchrotron emission, is carried by the interaction

with such fields.

It is possible to demonstrate, from the perspective of energy emission, that the emission of these particles is governed by an expression of the kind given below (De Angelis and Mallamaci (2018)):

$$\frac{dE_{CR}}{dt} \propto (m_e/M)^4 \tag{4.1}$$

where m_e stands for the mass of the electron and M is meant to represent the mass of the particle that is emitting it. This clearly indicates that the significance of this process increases proportionately with the decreasing mass of the particle being considered. Although hadrons, which will be covered in the following section, are capable of emitting in this manner, this phenomenon is of considerably greater importance for leptonic particles, which have lower masses.

In general, synchrotron emissions of leptonic origin have far lower energies than those associated with gamma photons. This mechanism is in fact very relevant for radio emissions. Its relevance to the higher-energy scenario is because leptons can up scatter low-energy photons causing the photons to leave this encounter with considerably higher energies than they entered with, possibly in the gamma region.

The scenario of a process known as Synchrotron Self-Compton (SSC) is an example of a situation that is of particular interest in the astrophysical scenario and can take place in AGNs. In this case, certain leptons emit radiation with an energy that is lower than that of the gamma band, with this radiation typically reaching X-ray energy in the higher cases, and the photons themselves then interact with the leptons from which they originated, via IC, elevating the photons' energy to the gamma band.

It can be seen in this way that emissions that originate from leptonic scenarios are of great interest for the case of gamma emissions: not because leptons are capable of directly generating gamma photons, but because they can generate photons that, when interacting with other leptonic particles, can increase in energy at the expense of the kinetic energy of the massive particles, and thus transform themselves into gamma photons.

In order to analyze our data from the leptonic perspective, we collaborated with Masaaki Kusunose to apply the previously developed model (Kusunose and Takahara (2012)) to our data and, from that, have an updated model of the central galactic scenario based on the idea that gamma emissions come from of electrons that interact with the medium of this

region. As a consequence of this, we will now proceed with an explanation of the model that was utilized, the results that were found, as well as a brief discussion.

4.3 A preliminary leptonic emission model

The emission of gamma photons in this model happens in a certain region, called the high energy region (HER). For simplicity, it is assumed that this region has a spherical shape with a radius r_γ and that all of it is permeated by a magnetic field B. The existence of high energy electrons is important to the functioning of this gamma emissions paradigm. In this situation, the majority of these electrons are supplied by flares that take place nearby the SMBH.

In order to obtain the self-consistent spectra of the gamma ray photons and the electrons, we must simultaneously solve the kinetic equations for electrons and photons. The following kinetic equation describes the electron state that is being taken into consideration:

$$q_{inj}(\gamma) = \frac{n_e(\gamma)}{t_{esc}} + \frac{\partial}{\partial\gamma}\dot{\gamma}_{rad} n_e(\gamma) \tag{4.2}$$

Here, in the specific scenario of non-thermal electrons, we have for a steady-state that the electrons are injected at a rate $q_{inj\gamma}$ per unit volume and per unit interval of electron Lorentz factor, γ. In addition to this, they are able to leave the so called zone of high-energy emission on a timescale that is indicated by t_{esc}. Moreover, $n_e(\gamma)$ stands for the number density of electrons per unit of γ, and $\dot{\gamma}_{rad}$ denotes the rate of radiative cooling that is associated to these electrons.

Two emission mechanisms are most relevant here: synchrotron emission and IC scattering. This happens because the synchrotron emission from the non-thermal electron population may provide part of the soft photons that, via IC scattering, receive more energy transforming themselves into photons of higher energy. Furthermore, photons from stars and dust may also function as soft photons if, as in the other case, they also undergo IC scattering.

It is expected, in accordance with the model that explains the emissions and behavior of the flares, that the injection of electrons takes place in such a way that the expression below is satisfied (Kusunose and Takahara (2010)):

$$q^f_{inj}(\gamma) = K^f_e \gamma^p \, H(\gamma - \gamma^f_{min}) \, e^{-\gamma/\gamma^f_{max}} \tag{4.3}$$

The Heaviside function is denoted by H in this expression, and K_e, p, γ^f_{max} and γ^f_{min} are parameters that are used to describe this injection.

Furthermore, taking into consideration the fact that, in the flare regions, electrons rapidly lose their temperature, and their description begins to obey a broken power law, at least approximately, this is the law that we employ to describe the electrons that are being injected in the high energies region (Kusunose and Takahara (2010)). In this sense, the following equation is applicable:

$$q_{\rm inj}(\gamma) = \begin{cases} K_1 \gamma^{-p_1} & (\gamma_{\rm min} \leq \gamma \leq \gamma_{\rm br}) \\ K_2 \gamma^{-p_2} & (\gamma_{\rm br} \leq \gamma \leq \gamma_{\rm max}) \end{cases} \tag{4.4}$$

Here, K_1, K_2, p_1, p_2, $\gamma_{\rm min}$, $\gamma_{\rm br}$ and $\gamma_{\rm max}$ are parameters. In particular with regard to the case of parameters K_1 and K_1, their determination is done by means of the injection rate per unit volume, the quantity that follows below:

$$q_{inj,0} = \int_{\gamma_{min}}^{\gamma_{max}} q_{inj}(\gamma) d\gamma \tag{4.5}$$

It is essential to have an understanding that the region of the GC is filled with soft photons. The origins of these photons are primarily associated with stars, dust, and local plasma, with these sources being interpreted by the model as the primary suppliers of soft photons. When looking at a region of the GC that is on the order of 1.2 pc in size, it is known that various kinds of emissions are responsable for different parts of the soft photon spectrum present in this environment (Mezger et al. (1996)). In particular regarding $\nu < 2 \times 10^{11}$ Hz, the domain occurs as a result of emission processes that are free-free. After that, the contribution of dust will dominate the emissions up to $\nu < 3 \times 10^{13}$ Hz, but stellar emissions will take over after that and continue to dominate all the way to $\nu < 2 \times 10^{16}$ Hz. Because of the Klein-Nishina effect, which occurs when photons of higher energy are subjected to IC scattering, the contribution of plasma emissions in the range given by $\nu > 2 \times 10^{16}$ Hz is not taken into account. Furthermore, due to uncertainties in the optical-UV spectrum, this part of the radiation is assumed to follow a blackbody spectrum, characterized by having a temperature $T_{\rm UV}$ and an energy density $u_{\rm UV}$.

	q_{inj} ($cm^{-3}\ s^{-1}$)	T_{UV} (eV)	u_{UV} (eV cm^{-3})	p_1	p_2	γ_{br}	γ_{max}
Model 1:	3×10^{-12}	1	8×10^4	1.3	2.54	6×10^2	1.6×10^5
Model 2:	1.2×10^{-11}	1	6×10^4	1.3	2.54	2×10^2	2×10^5
Model 3:	1.2×10^{-11}	2	10^5	1.3	2.54	2×10^2	2×10^5

Table 4.1 - Parameters used in the creation of different models of leptonic emission analysis.

4.4 Results and discussion

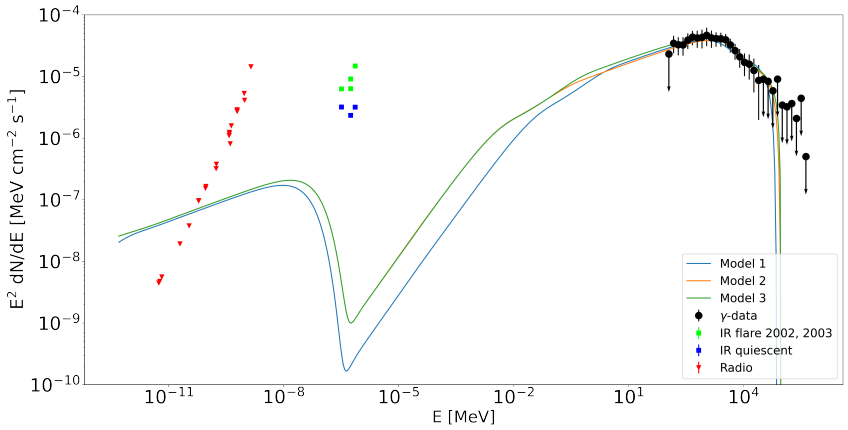

Figure 4.2: The SEDs explored in the analysis of the leptonic model compared with different observational data. Each of the parameters used in the construction of the curves for models 1-3 are available in table 4.1. The radio-submm emissions refer to a quiescent state and come from Markoff et al. (2001) and Zhao et al. (2003). The data for quiescent IR emissions and flares come, respectively, from Genzel et al. (2003) and Dodds-Eden et al. (2009).

The numerical calculations made uses a series of parameters, namely: q_{inj}, T_{UV}, u_{UV}, p_1, p_2, $\gamma_b r$ and γ_{max}. In addition to these, some other parameters are considered but are kept fixed in all analyses. Are they: $r_\gamma = 10^{18}$ cm, $B = 10^{-4}$ G and $\gamma_{min} = 2$. For convenience, the different parameters explored in three different models are available, in detail, in Table 4.1. It is important to point out that the values for these parameters were initially determined based on what was ultimately discovered for an analysis that was developed in a manner that was analogous to the one that was done in Kusunose and Takahara (2012).

Figure 4.2 displays, in turn, the results of the models and their comparison with observational data. In this particular instance, the model curves display emissions that are caused by the occurrence of IC scattering as well as accelerated electrons in flares. In par-

ticular, it is possible, according to any model, to establish that synchrotron emissions are the direct cause of emissions with energies lower than 1 eV. From this vantage point, one of the questions we could look into is whether or not there is a presence of self-Compton synchrotron emissions, also known as SSC. However, because the magnitude of the magnetic field that we are working with is currently at a level that allows us to disregard this possibility, we should do so.

In general, it is possible to deduce from the data presented in Figure 4.2 that the three models exhibit behavior that is comparable to one another. In addition, the curves that pertain to models 2 and 3 are quite similar to one another, only diverging in the region of high energies. This similarity between them is due to our choice of parameters, given that they have large parts of them the same, the difference being associated only with the parameters that describe the soft photons, as can be seen in Table 4.1. In addition, when we examine the curves that are associated with the models, there are two places that deserve to be highlighted. These are the break that occurs at energy 1×10^{-1} MeV, as well as the break that occurs at energy 204 MeV for model 1 and at energy 4×10^{-2} MeV and 413 MeV for models 2 and 3. The first break in each of these occurs as a result of the interaction of electrons with $\gamma \sim \gamma_{br}$ with IR-band energy photons. The second phenomenon takes place as a result of the interaction of these very same electrons with photons belonging to the optical-UV band. The occurrence of this can be traced back to IC scattering as the underlying physical mechanism in both of these instances.

It is also important to note that the radio emissions predicted by the model are higher at energies lower than 4×10^{-10} MeV. However, this is a result of the fact that we consider an emission around Sgr A* that encompasses a broader area than just the environment that is immediately surrounding it, specifically, we consider a 1pc region around the SMBH.

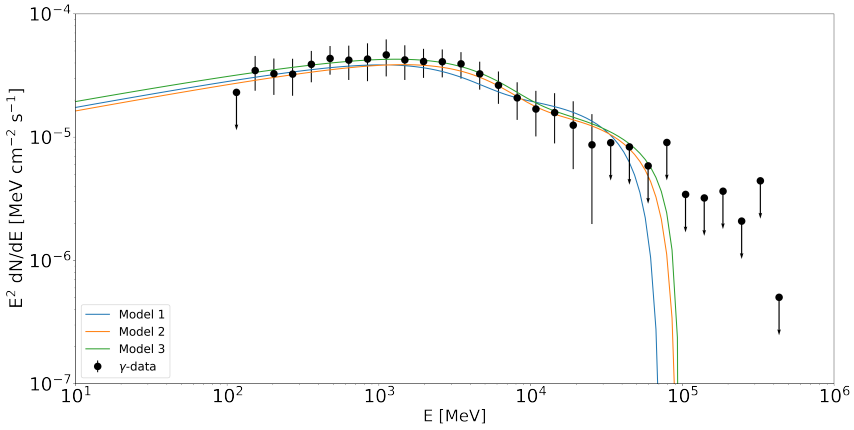

Figure 4.3: Details of the high energy regions of the SED explored from the leptonic model compared with the observational data from Figure 3.19. Each of the parameters used in the construction of the curves for models 1-3 are available in table 4.1.

Figure 4.3 provides a more in-depth look at the findings of the three models that were investigated, specifically with regard to the gamma emissions of the region that is of particular interest to us. In it, essentially, we can see the result of a preliminary comparison of these models with the observed data.

When taking into account the significance of one sigma up to the maximum energy of approximately 100 GeV, it has been determined that the three models that were investigated are all capable of adequately describing the data that was collected. Furthermore, it is noteworthy that in this qualitative analysis, it is not possible to make a distinction between which of the three models would best describe the observed data. This suggests that for the time being, there is no way in which we can use them to extract accurate values from the environment around Sgr A*, since models that use different parameters lead to equally valid fits. However, this does not indicate any problems because these models make it possible to: i) show that it is indeed possible to explore a leptonic model to describe the gamma emissions of the SMBH in question; and ii) impose limits on the values of the parameters that are used in the description of this model.

On the basis of this, a new stage of these analyses ought to be carried out. In essence, in light of the fact that this model is able to satisfactorily describe the observations that have been observed, we will need to investigate a different method of fitting in which we obtain from the measured data the curve of a model whose parameters best describe the observed data, making it possible to extract direct information from the SED that has

been discovered. Additionally, greater care will need to be taken with the other aspects of the process going forward. Specifically, the issue of the forecast radio emission and the radio data should be investigated, attempting, for example, to adjust the injection rate of electrons and the value of the magnetic field that is being utilized. It is important to keep in mind that this final component can, in fact, be investigated without having a significant impact on the model's predictions at high energies. This is because the most significant change will take place in the synchrotron emission processes, which are in charge of the component that is responsible for the lowest energy emission part.

Since the highest energy region of the observed data was not looked at as thoroughly as it should have been in the current methodology, this is yet another aspect that needs to be better investigated. Because these photons are the ones scattered by the electrons with the highest energies, the choice of γ_{max} values used in the models may have a great influence in the result and in order to investigate and justify these emissions, models that have the higher max Lorentz factor should be used. In any case, this is an analysis that will need to be done in order to gain an understanding of whether or not these electrons exists and are in fact accelerated in this region, obtaining such high energies from flares or not. The case of these kind of emissions may be the result of other types of sources participating in the process, such as pulsar wind nebulae, a kind of scenario explored by Hinton and Aharonian (2007).

Chapter 5

Conclusion

We conducted a very thorough investigation of the emissions emanating from the galactic core by making use of basically 14 years' worth of data collected by the *Fermi*-LAT satellite telescope: especially from source 4FGL J1745.6-2859, which is probably the gamma-ray equivalent of Sagittarius A*. From this perspective, two main things stand out, namely:

1. **We built the most robust SED for 4FGL J1745.6-2859 yet**:

   The SED that we created is the most reliable one that has ever been developed for this source in the energy range from 100MeV to 500GeV. This is because, at the time of our research, we used practically all of the data that was available from *Fermi*-LAT, did a detailed analysis of the qualities of the models we built and also carried out with an exhaustive treatment of the systematic errors that are inherent in this analysis.

   To be more specific, we made use of a variety of indicators in order to attest to the improvement in the model that we were developing. These indications included the likelihood value, the residual histograms, the residual maps, and the TS maps. In every instance, we are in a position to claim that the final product is a model that is vastly superior to the one we began with, and the only reason we ceased working on it is because there was no longer any valid possibilities to make any further advancements that would change the overall scenario.

   In the context of systematic errors, we studied if the selection of different galactic diffuse emission models - the model that describes the gamma radiation that permeates the galaxy, mainly the galactic center - altered the form of the SED that was acquired, and we came to the conclusion that it indeed led to a variation in the SED,

attesting that it is a source of systematic error that cannot be disregarded.

Subsequently, we investigated if the shape of the SED is also influenced by the sources that are present in the galactic center, and concluded that it does, meaning actually that our lack of knowledge about the sources that make up the galactic center also changes the SED we observe and this introduces another source os systematic errors.

From this, we merged all the information into a single, final and robust SED.

2. **We did a preliminary analysis of SED's gamma emissions of 4FGL J1745.6-2859 from a leptonic perspective**:

   We constructed an analysis of the gamma emissions of Sgr A* from a leptonic perspective through a collaboration with Dr. Masaaki Kusunose.

   In this study, we investigated the possibility of using three distinct models to provide an explanation for the data that was collected. Each of these models was produced using a unique set of initial parameters, and as a result, reflected a unique set of circumstances regarding the environment that was being considered.

   We came to the conclusion that in the energy band with the highest range of values, specifically between 100 MeV and 100GeV, all three models are equally capable of describing the data that was collected. This indicates that these values should serve, for the time being, as indicative of those that we actually have in the environment around the SMBH, reflecting that the set of initial parameters used in each model are all real possibilities for describing the environment that is being considered.

5.1 Future perspectives

In the context of future prospects, other points are worth highlighting:

1. **Finish the leptonic model:**

   Even though we have made progress in the analysis of gamma emissions from the lepton point of view, there is still potential for improvement in the general scenario, and this is something that we will explore.

   In particular, we hope to investigate it by inverting the strategy that has been used up until now with this model. This will allow us to extract from it the parameters

that best describe the observed data, as well as possible upper and lower limits for them. In this manner, we will be able to obtain a description that is more reliable and appropriate for the scenario that has been investigated.

Moreover, there are additional facets that need to be addressed and investigated further. In particular, we can continue to investigate a variety of electron injection rates and values for the magnetic field in order to gain a better understanding of the influence that these parameters have on the portion of the model that has the lowest energy. Exploring higher energy values for the electrons that are accelerated by flares while simultaneously evaluating the physical reality of the existence of these particles.

2. **Hadronic model for the 4FGL J1745.6-2859 SED**:

   When we talk about gamma emissions, two main scenarios arise: those originating from leptonic particles and those originating from hadronic particles. The first scenario was covered in this dissertation, however, the second one is not.

   It is relevant to do so as it will provide another perspective on these emissions. In an ideal scenario, we will try to identify whether these emissions are of this type or the other, meaning that we will Perform a confrontation between the results of the leptonic and hadronic models, in order to identify whether it is possible to differentiate the origin of the emissions from the GC. If possible, adequately justify the reason for this and clearly point out the finding and the consequences for the galactic center.

   Moreover, in the scenario that this distinction is not possible, this process is still valid, and for sure will provide a better perspective of the environment of the galactic center, making us have a better understanding of what kind of observations we will need to make to be able to differentiate them in the future.

   To do this treatment, we will collaborate with Timothy Linden and refine his model (Linden et al. (2012)) for use in our data.

Also, there is no doubt that the next generation of gamma-ray telescopes will make a significant contribution to our overall comprehension of the GC. This is due to the fact that we anticipate that, with their help, we will be able to achieve superior imaging and superior analysis possibilities compared to those that are currently done.

To be more specific, it is hoped that with the introduction of the Cherenkov Telescope Array (CTA), we will be able to obtain a significantly better exposure of the GC. Specifically, observations at angular resolutions better than those that can be made with the *Fermi*-LAT will be made with the CTA, given that it is anticipated to reach resolutions on the order of arcminutes. In addition to this, it is going to investigate an energy band that spans from 20 GeV to 300 TeV, which will make it possible, for instance, to refine and delve deeper into the results found in this dissertation. It is also anticipated that with it, it will be possible to carry out analyses on the gaseous distribution of the GC, thereby definitively linking the gamma emissions associated with Sgr A* to either leptonic or hadronic processes.

Bibliography

Acceleration of petaelectronvolt protons in the Galactic Centre, Nature, 2016, vol. 531, p. 476

Abdalla H., Abramowski A., Aharonian F., Benkhali F. A., Akhperjanian A., Andersson T., Angüner E., Arakawa M., Arrieta M., Aubert P., et al., Characterising the VHE diffuse emission in the central 200 parsecs of our Galaxy with HESS, Astronomy & Astrophysics, 2018, vol. 612, p. A9

Abdollahi S., Acero F., Ackermann M., Ajello M., Atwood W., Axelsson M., Baldini L., Ballet J., Barbiellini G., Bastieri D., et al., Fermi large area telescope fourth source catalog, The Astrophysical Journal Supplement Series, 2020, vol. 247, p. 33

Abdollahi S., Acero F., Baldini L., Ballet J., Bastieri D., Bellazzini R., Berenji B., Berretta A., Bissaldi E., Blandford R. D., et al., Incremental Fermi Large Area Telescope Fourth Source Catalog, arXiv preprint arXiv:2201.11184, 2022

Abuter R., Amorim A., Anugu N., Bauböck M., Benisty M., Berger J.-P., Blind N., Bonnet H., Brandner W., Buron A., et al., Detection of the gravitational redshift in the orbit of the star S2 near the Galactic centre massive black hole, Astronomy & Astrophysics, 2018, vol. 615, p. L15

Abuter R., Amorim A., Bauböck M., Berger J., Bonnet H., Brandner W., Cardoso V., Clénet Y., De Zeeuw P., Dexter J., et al., Detection of the Schwarzschild precession in the orbit of the star S2 near the Galactic centre massive black hole, Astronomy & Astrophysics, 2020, vol. 636, p. L5

Abuter R., Amorim A., Bauböck M., Berger J., Bonnet H., Brandner W., Clénet Y., Du Foresto V. C., de Zeeuw P., Deen C., et al., Detection of orbital motions near the last stable circular orbit of the massive black hole SgrA, Astronomy & Astrophysics, 2018, vol. 618, p. L10

Abuter R., Amorim A., Bauböck M., Berger J., Bonnet H., Brandner W., Clénet Y., Du Foresto V. C., De Zeeuw P., Dexter J., et al., A geometric distance measurement to the Galactic center black hole with 0.3% uncertainty, Astronomy & Astrophysics, 2019, vol. 625, p. L10

Acciari V. A., Ansoldi S., Antonelli L., Engels A. A., Baack D., Babić A., Banerjee B., de Almeida U. B., Barrio J., González J. B., et al., MAGIC observations of the diffuse γ-ray emission in the vicinity of the Galactic center, Astronomy & Astrophysics, 2020, vol. 642, p. A190

Ackermann M., Ajello M., Albert A., Atwood W., Baldini L., Ballet J., Barbiellini G., Bastieri D., Bellazzini R., Bissaldi E., et al., The Fermi galactic center GeV excess and implications for dark matter, The Astrophysical Journal, 2017, vol. 840, p. 43

Ackermann M., Ajello M., Atwood W., Baldini L., Ballet J., Barbiellini G., Bastieri D., Bechtol K., Bellazzini R., Berenji B., et al., Fermi-LAT observations of the diffuse γ-ray emission: implications for cosmic rays and the interstellar medium, The Astrophysical Journal, 2012, vol. 750, p. 3

Ackermann M., Albert A., Atwood W., Baldini L., Ballet J., Barbiellini G., Bastieri D., Bellazzini R., Bissaldi E., Blandford R., et al., The spectrum and morphology of the Fermi bubbles, The Astrophysical Journal, 2014, vol. 793, p. 64

Aharonian F., Akhperjanian A., Aye K.-M., Bazer-Bachi A., Beilicke M., Benbow W., Berge D., Berghaus P., Bernlöhr K., Bolz O., et al., Very high energy gamma rays from the direction of Sagittarius A, Astronomy & astrophysics, 2004, vol. 425, p. L13

Ahnen M., Ansoldi S., Antonelli L., Antoranz P., Arcaro C., Babic A., Banerjee B., Bangale P., De Almeida U. B., Barrio J., et al., Observations of Sagittarius A* during the pericenter passage of the G2 object with MAGIC, Astronomy & Astrophysics, 2017, vol. 601, p. A33

Ajello M., Albert A., Atwood W., Barbiellini G., Bastieri D., Bechtol K., Bellazzini R., Bissaldi E., Blandford R., Bloom E., et al., Fermi-LAT observations of high-energy γ-ray emission toward the galactic center, The Astrophysical Journal, 2016, vol. 819, p. 44

Akiyama K., Alberdi A., Alef W., Algaba J. C., Anantua R., Asada K., Azulay R., Bach U., Baczko A.-K., Ball D., et al., First Sagittarius A* Event Horizon Telescope Results. I. The Shadow of the Supermassive Black Hole in the Center of the Milky Way, The Astrophysical Journal Letters, 2022, vol. 930, p. L12

Albert J., Aliu E., Anderhub H., Antoranz P., Armada A., Asensio M., Baixeras C., Barrio J., Bartelt M., Bartko H., et al., Observation of gamma rays from the galactic center with the MAGIC telescope, The Astrophysical Journal, 2006, vol. 638, p. L101

Alexander T., Stellar processes near the massive black hole in the Galactic center, Physics Reports, 2005, vol. 419, p. 65

Armillotta L., Krumholz M. R., Di Teodoro E. M., McClure-Griffiths N., The life cycle of the Central Molecular Zone–I. Inflow, star formation, and winds, Monthly Notices of the Royal Astronomical Society, 2019, vol. 490, p. 4401

Atwood W., Abdo A. A., Ackermann M., Althouse W., Anderson B., Axelsson M., Baldini L., Ballet J., Band D., Barbiellini G., et al., The large area telescope on the Fermi gamma-ray space telescope mission, The Astrophysical Journal, 2009, vol. 697, p. 1071

Baganoff F., Bautz M., Brandt W. N., Chartas G., Feigelson E., Garmire G., Maeda Y., Morris M., Ricker G., Townsley L., et al., Rapid X-ray flaring from the direction of the supermassive black hole at the Galactic Centre, Nature, 2001, vol. 413, p. 45

Baganoff F. K., Maeda Y., Morris M., Bautz M., Brandt W., Cui W., Doty J., Feigelson E., Garmire G., Pravdo S., et al., Chandra X-ray spectroscopic imaging of Sagittarius A* and the central parsec of the galaxy, The Astrophysical Journal, 2003, vol. 591, p. 891

Ball D., Özel F., Psaltis D., Chan C.-k., Particle Acceleration and the Origin of X-Ray Flares in GRMHD Simulations of SGR A, The Astrophysical Journal, 2016, vol. 826, p. 77

Ballantyne D., Schumann M., Ford B., Modelling the time-dependence of the TeV γ-ray source at the Galactic Centre, Monthly Notices of the Royal Astronomical Society, 2011, vol. 410, p. 1521

Boehle A., Ghez A., Schödel R., Meyer L., Yelda S., Albers S., Martinez G., Becklin E., Do T., Lu J., et al., An improved distance and mass estimate for Sgr A* from a multistar orbit analysis, The Astrophysical Journal, 2016, vol. 830, p. 17

Boyce H., Haggard D., Witzel G., von Fellenberg S., Willner S., Becklin E., Do T., Eckart A., Fazio G., Gurwell M., et al., Multi-wavelength Variability of Sagittarius A* in July 2019, arXiv preprint arXiv:2203.13311, 2022

Boyce H., Haggard D., Witzel G., Willner S., Neilsen J., Hora J., Markoff S., Ponti G., Baganoff F., Becklin E., et al., Simultaneous X-Ray and Infrared Observations of Sagittarius A*'s Variability, The Astrophysical Journal, 2019, vol. 871, p. 161

Brinkerink C. D., Falcke H., Law C. J., Barkats D., Bower G. C., Brunthaler A., Gammie C., Impellizzeri C. V., Markoff S., Menten K. M., et al., ALMA and VLA measurements of frequency-dependent time lags in Sagittarius A*: evidence for a relativistic outflow, Astronomy & Astrophysics, 2015, vol. 576, p. A41

Brown R. L., Intense sub-arcsecond structure in the galactic center, Reprints-National Radio Astronomy Observatory, Green Bank, W. Va: Series A., 1973, vol. 194, p. 265

Brown R. L., Liszt H. S., Sagittarius A and its environment, Annual review of astronomy and astrophysics, 1984, vol. 22, p. 223

Cafardo F., Nemmen R., Collaboration F. L., et al., Fermi-LAT Observations of Sagittarius A*: Imaging Analysis, The Astrophysical Journal, 2021, vol. 918, p. 30

Calderón D., Cuadra J., Schartmann M., Burkert A., Russell C. M., Stellar winds pump the heart of the Milky Way, The Astrophysical Journal Letters, 2019, vol. 888, p. L2

Chen Z., Gallego-Cano E., Do T., Witzel G., Ghez A., Schödel R., Sitarski B., Becklin E., Lu J., Morris M., et al., Consistency of the Infrared Variability of SGR A* over 22 yr, The Astrophysical journal letters, 2019, vol. 882, p. L28

Cheng K.-S., Chernyshov D., Dogiel V., Ko C.-M., Ip W.-H., Origin of the Fermi bubble, The Astrophysical Journal Letters, 2011, vol. 731, p. L17

Chernyakova M., Malyshev D., Aharonian F., Crocker R., Jones D. I., The high-energy, Arcminute-scale galactic center gamma-ray source, The Astrophysical Journal, 2010, vol. 726, p. 60

Christopher M., Scoville N., Stolovy S., Yun M. S., HCN and HCO+ observations of the Galactic circumnuclear disk, The Astrophysical Journal, 2005, vol. 622, p. 346

De Angelis A., Mallamaci M., Gamma-ray astrophysics, The European Physical Journal Plus, 2018, vol. 133, p. 1

Do T., Lu J. R., Ghez A. M., Morris M. R., Yelda S., Martinez G. D., Wright S. A., Matthews K., Stellar populations in the central 0.5 pc of the Galaxy. I. A new method for constructing luminosity functions and surface-density profiles, The Astrophysical Journal, 2013, vol. 764, p. 154

Dodds-Eden K., Porquet D., Trap G., Quataert E., Haubois X., Gillessen S., Grosso N., Pantin E., Falcke H., Rouan D., et al., Evidence for x-ray synchrotron emission from simultaneous mid-infrared to x-ray observations of a strong Sgr A* flare, The Astrophysical Journal, 2009, vol. 698, p. 676

Eckart A., Hüttemann A., Kiefer C., Britzen S., Zajaček M., Lämmerzahl C., Stöckler M., Valencia-S M., Karas V., García-Marín M., The Milky Way's supermassive black hole: how good a case is it?, Foundations of Physics, 2017, vol. 47, p. 553

Eckart A., Schödel R., Meyer L., Trippe S., Ott T., Genzel R., Polarimetry of near-infrared flares from Sagittarius A, Astronomy & Astrophysics, 2006, vol. 455, p. 1

Eckart A., Straubmeier C. M., et al., The black hole at the center of the Milky Way. Imperial College Press, 2005

Eckart A., Zajacek M., Parsa M., Fazeli E. H. N., Busch G., Shahzamanian B., Subroweit M., Peissker F., Sabha N., Horrobin M., et al., The Multifrequency Behavior of Sagittarius A, arXiv preprint arXiv:1806.00284, 2018

Edgar R., A review of Bondi–Hoyle–Lyttleton accretion, New Astronomy Reviews, 2004, vol. 48, p. 843

Einstein A., Die feldgleichungen der gravitation, Sitzung der physikalische-mathematischen Klasse, 1915, vol. 25, p. 844

Eisenhauer F., Genzel R., Alexander T., Abuter R., Paumard T., Ott T., Gilbert A., Gillessen S., Horrobin M., Trippe S., et al., SINFONI in the galactic center: young stars and infrared flares in the central light-month, The Astrophysical Journal, 2005, vol. 628, p. 246

Fabian A. C., Observational evidence of active galactic nuclei feedback, Annual Review of Astronomy and Astrophysics, 2012, vol. 50, p. 455

Fatuzzo M., Melia F., A kinship between the EGRET supernova remnants and Sagittarius A East, The Astrophysical Journal, 2003, vol. 596, p. 1035

Fatuzzo M., Melia F., Diffusive cosmic-ray acceleration in Sagittarius A, The Astrophysical Journal Letters, 2012, vol. 757, p. L16

Fazio G., Hora J., Witzel G., Willner S., Ashby M., Baganoff F., Becklin E., Carey S., Haggard D., Gammie C., et al., Multiwavelength Light Curves of Two Remarkable Sagittarius A* Flares, The Astrophysical Journal, 2018, vol. 864, p. 58

Freitag M., Amaro-Seoane P., Kalogera V., Stellar remnants in galactic nuclei: mass segregation, The Astrophysical Journal, 2006, vol. 649, p. 91

Genzel R., Eisenhauer F., Gillessen S., The Galactic Center massive black hole and nuclear star cluster, Reviews of Modern Physics, 2010, vol. 82, p. 3121

Genzel R., Hollenbach D., Townes C. H., The nucleus of our Galaxy, Reports on Progress in Physics, 1994, vol. 57, p. 417

Genzel R., Karas V., The galactic center, Proceedings of the International Astronomical Union, 2006, vol. 2, p. 173

Genzel R., Schödel R., Ott T., Eckart A., Alexander T., Lacombe F., Rouan D., Aschenbach B., Near-infrared flares from accreting gas around the supermassive black hole at the Galactic Centre, Nature, 2003, vol. 425, p. 934

Ghez A., Duchêne G., Matthews K., Hornstein S., Tanner A., Larkin J., Morris M., Becklin E., Salim S., Kremenek T., et al., The first measurement of spectral lines in a short-period star bound to the Galaxy's central black hole: a paradox of youth, The Astrophysical Journal, 2003, vol. 586, p. L127

Ghez A., Wright S., Matthews K., Thompson D., Le Mignant D., Tanner A., Hornstein S. D., Morris M., Becklin E., Soifer B., Variable infrared emission from the supermassive black hole at the center of the Milky Way, The Astrophysical Journal, 2004, vol. 601, p. L159

Ghez A. M., Salim S., Weinberg N., Lu J., Do T., Dunn J., Matthews K., Morris M., Yelda S., Becklin E., et al., Measuring distance and properties of the Milky Way's central supermassive black hole with stellar orbits, The Astrophysical Journal, 2008, vol. 689, p. 1044

Gillessen S., Eisenhauer F., Fritz T., Bartko H., Dodds-Eden K., Pfuhl O., Ott T., Genzel R., The orbit of the star S2 around SGR A* from very large telescope and keck data, The Astrophysical Journal, 2009, vol. 707, p. L114

Gillessen S., Eisenhauer F., Trippe S., Alexander T., Genzel R., Martins F., Ott T., Monitoring stellar orbits around the Massive Black Hole in the Galactic Center, The Astrophysical Journal, 2009, vol. 692, p. 1075

Gillessen S., Genzel R., Fritz T. K., Eisenhauer F., Pfuhl O., Ott T., Schartmann M., Ballone A., Burkert A., Pericenter passage of the gas cloud G2 in the Galactic Center, The Astrophysical Journal, 2013, vol. 774, p. 44

Goodenough L., Hooper D., Possible evidence for dark matter annihilation in the inner Milky Way from the Fermi Gamma Ray Space Telescope, arXiv preprint arXiv:0910.2998, 2009

Goss W., Brown R. L., Lo K., The discovery of Sgr A, Astronomische Nachrichten: Astronomical Notes, 2003, vol. 324, p. 497

Grenier I. A., Casandjian J.-M., Terrier R., Unveiling extensive clouds of dark gas in the solar neighborhood, Science, 2005, vol. 307, p. 1292

Guo Y.-Q., Tian Z., Wang Z., Li H.-J., Chen T.-L., The galactic center: a petaelectronvolt cosmic-ray acceleration factory, The Astrophysical Journal, 2017, vol. 836, p. 233

Guo Y.-Q., Yuan Q., Liu C., Li A.-F., A hybrid model of GeV–TeV gamma ray emission from the Galactic center, Journal of Physics G: Nuclear and Particle Physics, 2013, vol. 40, p. 065201

Güsten R., Genzel R., Wright M., Jaffe D., Stutzki J., Harris A., Aperture synthesis observations of the circumnuclear ring in the Galactic center, The Astrophysical Journal, 1987, vol. 318, p. 124

Hartman R., Bertsch D., Bloom S., Chen A., Deines-Jones P., Esposito J., Fichtel C., Friedlander D., Hunter S., McDonald L., et al., The third EGRET catalog of high-energy gamma-ray sources, The Astrophysical Journal Supplement Series, 1999, vol. 123, p. 79

Heckman T. M., Best P. N., The coevolution of galaxies and supermassive black holes: insights from surveys of the contemporary universe, Annual Review of Astronomy and Astrophysics, 2014, vol. 52, p. 589

Herrnstein R. M., Zhao J.-H., Bower G. C., Goss W., The variability of Sagittarius A* at centimeter wavelengths, The Astronomical Journal, 2004, vol. 127, p. 3399

Hinton J., Aharonian F., Inverse compton scenarios for the TeV gamma-ray emission of the galactic center, The Astrophysical Journal, 2007, vol. 657, p. 302

Hooper D., Cholis I., Linden T., TeV gamma rays from Galactic Center pulsars, Physics of the dark universe, 2018, vol. 21, p. 40

Hooper D., Dingus B., Improving the angular resolution of EGRET and new limits on supersymmetric dark matter near the galactic center, Advances in Space Research, 2005, vol. 35, p. 130

Hooper D., Goodenough L., Dark matter annihilation in the Galactic Center as seen by the Fermi Gamma Ray Space Telescope, Physics Letters B, 2011, vol. 697, p. 412

Hooper D., Linden T., Origin of the gamma rays from the Galactic Center, Physical Review D, 2011, vol. 84, p. 123005

Hsieh P.-Y., Koch P. M., Ho P. T., Kim W.-T., Tang Y.-W., Wang H.-H., Yen H.-W., Hwang C.-Y., Molecular gas feeding the circumnuclear disk of the Galactic Center, The Astrophysical Journal, 2017, vol. 847, p. 3

Hughes S. A., Trust but verify: The case for astrophysical black holes, arXiv preprint hep-ph/0511217, 2005

Jackson J., Geis N., Genzel R., Harris A., Madden S., Poglitsch A., Stacey G., Townes C., Neutral gas in the central 2 parsecs of the Galaxy, The Astrophysical Journal, 1993, vol. 402, p. 173

Jansky K. G., Radio waves from outside the solar system, Nature, 1933, vol. 132, p. 66

Kanbach G., Bertsch D., Favale A., Fichtel C., Hartman R., Hofstadter R., Hughes E., Hunter S., Hughlock B., Kniffen D., et al., The project EGRET (energetic gamma-ray experiment telescope) on NASA's Gamma-Ray Observatory GRO, Space Science Reviews, 1989, vol. 49, p. 69

Kormendy J., Ho L. C., Coevolution (or not) of supermassive black holes and host galaxies, Annual Review of Astronomy and Astrophysics, 2013, vol. 51, p. 511

Kosack K., Badran H., Bond I., Boyle P., Bradbury S., Buckley J., Carter-Lewis D., Celik O., Connaughton V., Cui W., et al., TeV gamma-ray observations of the galactic center, The Astrophysical Journal, 2004, vol. 608, p. L97

Kusunose M., Takahara F., Synchrotron Blob Model of Infrared and X-ray Flares from Sagittarius A, The Astrophysical Journal, 2010, vol. 726, p. 54

Kusunose M., Takahara F., A leptonic model of steady high-energy gamma-ray emission from Sgr A, The Astrophysical Journal, 2012, vol. 748, p. 34

Lacy J. H., Townes C. H., Geballe T. R., Hollenbach D. J., Observations of the motion and distribution of the ionized gas in the central parsec of the Galaxy. II, Astrophysical Journal, Part 1, vol. 241, Oct. 1, 1980, p. 132-146. Research supported by the University of California and NASA, 1980, vol. 241, p. 132

Lacy J. H., Townes C. H., Hollenbach D. J., The nature of the central parsec of the Galaxy, The Astrophysical Journal, 1982, vol. 262, p. 120

Lense J., Thirring H., Über den Einfluss der Eigenrotation der Zentralkörper auf die Bewegung der Planeten und Monde nach der Einsteinschen Gravitationstheorie, Physikalische Zeitschrift, 1918, vol. 19, p. 156

Linden T., Lovegrove E., Profumo S., The morphology of hadronic emission models for the gamma-ray source at the galactic center, The Astrophysical Journal, 2012, vol. 753, p. 41

Longair M. S., High energy astrophysics. Cambridge university press, 2010

Lynden-Bell D., Galactic nuclei as collapsed old quasars, Nature, 1969, vol. 223, p. 690

Malyshev D., Chernyakova M., Neronov A., Walter R., Leptonic origin of the 100 MeV γ-ray emission from the Galactic centre, Astronomy & Astrophysics, 2015, vol. 582, p. A11

Markoff S., Falcke H., Yuan F., Biermann P. L., The Nature of the 10 kilosecond X-ray flare in Sgr A, Astronomy & Astrophysics, 2001, vol. 379, p. L13

Marrone D., Baganoff F., Morris M., Moran J. M., Ghez A., Hornstein S., Dowell C., Muñoz D. J., Bautz M., Ricker G., et al., An x-ray, infrared, and submillimeter flare of Sagittarius A, The Astrophysical Journal, 2008, vol. 682, p. 373

Marrone D. P., Moran J. M., Zhao J.-H., Rao R., Interferometric measurements of variable 340 GHz linear polarization in Sagittarius A, The Astrophysical Journal, 2006, vol. 640, p. 308

Mattox J. R., Bertsch D., Chiang J., Dingus B., Digel S., Esposito J., Fierro J., Hartman R., Hunter S., Kanbach G., et al., The likelihood analysis of EGRET data, The Astrophysical Journal, 1996, vol. 461, p. 396

Mauerhan J. C., Morris M., Walter F., Baganoff F. K., Intraday variability of Sagittarius A* at 3 millimeters, The Astrophysical Journal, 2005, vol. 623, p. L25

Mayer-Hasselwander H., Bertsch D., Dingus B., Eckart A., Esposito J., Genzel R., Hartman R., Hunter S., Kanbach G., Kniffen D., et al., High-energy gamma-ray emission from the Galactic Center, Astronomy and Astrophysics, v. 335, p. 161-172 (1998), 1998, vol. 335, p. 161

Merritt D., Single and binary black holes and their influence on nuclear structure, Carnegie Observatories Astrophysics Series Vol. 1: Coevolution of Black Holes and Galaxies, 2004, p. 263

Mertsch P., Petrosian V., Fermi bubbles from stochastic acceleration of electrons in a Galactic outflow, Astronomy & Astrophysics, 2019, vol. 622, p. A203

Mezger P. G., Duschl W. J., Zylka R., The Galactic Center: a laboratory for AGN?, The Astronomy and Astrophysics Review, 1996, vol. 7, p. 289

Miyazaki A., Tsutsumi T., Tsuboi M., Intraday variation of Sagittarius A* at short millimeter wavelengths, The Astrophysical Journal, 2004, vol. 611, p. L97

Montero-Castaño M., Herrnstein R. M., Ho P. T., Gas Infall Toward Sgr A* from the Clumpy Circumnuclear Disk, The Astrophysical Journal, 2009, vol. 695, p. 1477

Mouawad N., Eckart A., Pfalzner S., Schödel R., Moultaka J., Spurzem R., Weighing the cusp at the Galactic Centre, Astronomische Nachrichten: Astronomical Notes, 2005, vol. 326, p. 83

Murchikova E. M., Phinney E. S., Pancoast A., Blandford R. D., A cool accretion disk around the Galactic Centre black hole, Nature, 2019, vol. 570, p. 83

Murchikova L., Witzel G., Second-scale submillimeter variability of Sagittarius A* during flaring activity of 2019: on the origin of bright near-infrared flares, The Astrophysical Journal Letters, 2021, vol. 920, p. L7

Narayan R., Yi I., Mahadevan R., Explaining the spectrum of Sagittarius A* with a model of an accreting black hole, Nature, 1995, vol. 374, p. 623

Negro M., Fleischhack H., Zoglauer A., Digel S., Ajello M., Unveiling the origin of the fermi bubbles with MeV photon telescopes, The Astrophysical Journal, 2022, vol. 927, p. 225

Neilsen J., Nowak M., Gammie C., Dexter J., Markoff S., Haggard D., Nayakshin S., Wang Q., Grosso N., Porquet D., et al., A Chandra/HETGS census of X-ray variability from Sgr A* during 2012, The Astrophysical Journal, 2013, vol. 774, p. 42

Netzer H., The physics and evolution of active galactic nuclei. Cambridge university press, 2013

Netzer H., Revisiting the unified model of active galactic nuclei, arXiv preprint arXiv:1505.00811, 2015

Nowak M., Neilsen J., Markoff S., Baganoff F., Porquet D., Grosso N., Levin Y., Houck J., Eckart A., Falcke H., et al., Chandra/HETGS observations of the brightest flare seen from Sgr A, The Astrophysical Journal, 2012, vol. 759, p. 95

Oka T., Nagai M., Kamegai K., Tanaka K., A New Look at the Galactic Circumnuclear Disk, The Astrophysical Journal, 2011, vol. 732, p. 120

Paumard T., Genzel R., Martins F., Nayakshin S., Beloborodov A., Levin Y., Trippe S., Eisenhauer F., Ott T., Gillessen S., et al., The two young star disks in the central parsec of the galaxy: properties, dynamics, and formation, The Astrophysical Journal, 2006, vol. 643, p. 1011

Paumard T., Maillard J.-P., Stolovy S., New results on the Galactic Center Helium stars, Astronomische Nachrichten: Astronomical Notes, 2003, vol. 324, p. 303

Peebles P., Star distribution near a collapsed object, The Astrophysical Journal, 1972, vol. 178, p. 371

Peißker F., Eckart A., Zajaček M., Ali B., Parsa M., S62 and S4711: Indications of a Population of Faint Fast-moving Stars inside the S2 Orbit—S4711 on a 7.6 yr Orbit around Sgr A, The Astrophysical Journal, 2020, vol. 899, p. 50

Plewa P., Gillessen S., Pfuhl O., Eisenhauer F., Genzel R., Burkert A., Dexter J., Habibi M., George E., Ott T., et al., The Post-pericenter Evolution of the Galactic Center Source G2, The Astrophysical Journal, 2017, vol. 840, p. 50

Ponti G., George E., Scaringi S., Zhang S., Jin C., Dexter J., Terrier R., Clavel M., Degenaar N., Eisenhauer F., et al., A powerful flare from Sgr A* confirms the synchrotron nature of the X-ray emission, Monthly Notices of the Royal Astronomical Society, 2017, vol. 468, p. 2447

Porter T. A., Johannesson G., Moskalenko I. V., High-energy gamma rays from the Milky Way: three-dimensional spatial models for the cosmic-ray and radiation field densities in the interstellar medium, The Astrophysical Journal, 2017, vol. 846, p. 67

Psaltis D., Testing general relativity with the Event Horizon Telescope, General Relativity and Gravitation, 2019, vol. 51, p. 1

Quataert E., Dorland W., Hammett G. W., The magnetorotational instability in a collisionless plasma, The Astrophysical Journal, 2002, vol. 577, p. 524

Rubilar G., Eckart A., Periastron shifts of stellar orbits near the Galactic Center, Astronomy & Astrophysics, 2001, vol. 374, p. 95

Saitoh T. R., Makino J., Asaki Y., Baba J., Komugi S., Miyoshi M., Nagao T., Takahashi M., Takeda T., Tsuboi M., et al., Flaring up of the compact cloud G2 during the close encounter with Sgr A, Publications of the Astronomical Society of Japan, 2014, vol. 66

Schartmann M., Burkert A., Alig C., Gillessen S., Genzel R., Eisenhauer F., Fritz T., Simulations of the origin and fate of the Galactic Center cloud G2, The Astrophysical Journal, 2012, vol. 755, p. 155

Stone J. M., Marrone D. P., Dowell C., Schulz B., Heinke C., Yusef-Zadeh F., Far infrared variability of Sagittarius A*: 25.5 hr of monitoring with Herschel, The Astrophysical Journal, 2016, vol. 825, p. 32

Su M., Slatyer T. R., Finkbeiner D. P., Giant gamma-ray bubbles from Fermi-LAT: active galactic nucleus activity or bipolar galactic wind?, The Astrophysical Journal, 2010, vol. 724, p. 1044

Sundbäck D., Degree Project Analysis of the Hard Spectrum BL Lac Source 1H 1914-194 with Fermi-LAT Data and Multiwavelength Modelling, 2018, Ph.D. Thesis

Thirring H., Über die Wirkung rotierender ferner Massen in der Einsteinschen Gravitationstheorie., Physikalische Zeitschrift, 1918, vol. 19, p. 33

Thirring H., Berichtigung zu meiner Arbeit:"Über die Wirkung rotierender Massen in der Einsteinschen Gravitationstheorie", Physikalische Zeitschrift, 1921, vol. 22, p. 29

Thorne K. S., Misner C. W., Wheeler J. A., Gravitation. Freeman San Francisco, CA, 2000

Tsuboi M., Kitamura Y., Uehara K., Tsutsumi T., Miyawaki R., Miyoshi M., Miyazaki A., ALMA view of the circumnuclear disk of the Galactic Center: tidally disrupted molecular clouds falling to the Galactic Center, Publications of the Astronomical Society of Japan, 2018, vol. 70, p. 85

Vasiliev E., Zelnikov M., Dark matter dynamics in the galactic center, Physical Review D, 2008, vol. 78, p. 083506

Vollmer B., Duschl W. J., The Minispiral in the Galactic Center revisited, New Astronomy, 2000, vol. 4, p. 581

von Fellenberg S. D., Witzel G., Bauböck M., Chung H.-H., Aimar N., Bordoni M., Drescher A., Eisenhauer F., Genzel R., Gillessen S., et al., General relativistic effects and the near-infrared and X-ray variability of Sgr A* I, arXiv preprint arXiv:2301.02558, 2023

Witzel G., Martinez G., Hora J., Willner S., Morris M., Gammie C., Becklin E., Ashby M., Baganoff F., Carey S., et al., Variability timescale and spectral index of Sgr A* in the near infrared: approximate Bayesian computation analysis of the variability of the closest supermassive black hole, The Astrophysical Journal, 2018, vol. 863, p. 15

Witzel G., Martinez G., Willner S., Becklin E., Boyce H., Do T., Eckart A., Fazio G., Ghez A., Gurwell M., et al., Rapid variability of Sgr A* across the electromagnetic spectrum, The Astrophysical Journal, 2021, vol. 917, p. 73

Wollman E., Geballe T., Lacy J., Townes C., Rank D., NE II 12.8 micron emission from the galactic center. II, The Astrophysical Journal, 1977, vol. 218, p. L103

Wood M., Caputo R., Charles E., Di Mauro M., Magill J., Perkins J., Fermipy: An open-source Python package for analysis of Fermi-LAT Data, arXiv preprint arXiv:1707.09551, 2017

Xu Y.-D., Narayan R., Quataert E., Yuan F., Baganoff F. K., Thermal X-ray iron line emission from the galactic center black hole Sagittarius A, The Astrophysical Journal, 2006, vol. 640, p. 319

Yang H.-Y. K., Ruszkowski M., Zweibel E. G., Unveiling the origin of the Fermi bubbles, Galaxies, 2018, vol. 6, p. 29

Yuan F., Quataert E., Narayan R., Nonthermal electrons in radiatively inefficient accretion flow models of Sagittarius A, The Astrophysical Journal, 2003, vol. 598, p. 301

Yusef-Zadeh F., Bushouse H., Wardle M., Heinke C., Roberts D., Dowell C., Brunthaler A., Reid M., Martin C., Marrone D., et al., SIMULTANEOUS MULTI-WAVELENGTH OBSERVATIONS OF Sgr A* DURING 2007 APRIL 1–11, The Astrophysical Journal, 2009, vol. 706, p. 348

Yusef-Zadeh F., Wardle M., Dodds-Eden K., Heinke C., Gillessen S., Genzel R., Bushouse H., Grosso N., Porquet D., An inverse compton scattering origin of X-ray flares from Sgr A, The Astronomical Journal, 2012, vol. 144, p. 1

Zhao J.-H., Young K., Herrnstein R., Ho P., Tsutsumi T., Lo K., Goss W., Bower G., Variability of Sagittarius A*: Flares at 1 millimeter, The Astrophysical Journal, 2003, vol. 586, p. L29

Zylka R., Mezger P., Ward-Thompson D., Duschl W., Lesch H., Anatomy of the Sagittarius A complex: IV. Sgr A* and the Central Cavity revisi-ted, arXiv preprint astro-ph/9410086, 1994